

**Magnetic Resonance Imaging for Monitoring Irreversible Electroporation of
Hepatocellular Carcinoma**

BY

YUE ZHANG

B.S., Nanjing University of Aeronautics and Astronautics, 2007

M.S., University of Illinois at Chicago, Chicago, 2011

THESIS

Submitted as partial fulfillment of the requirements
for the degree of Doctor of Philosophy in Bioengineering
in the Graduate College of the
University of Illinois at Chicago, 2013

Chicago, Illinois

Defense Committee:

Richard L. Magin, Ph.D., Chair

Andrew C. Larson, Ph.D., Advisor

Thomas J. Royston, Ph.D.

Ron C. Gaba, M.D., Radiology

Robert J. Lewandowski, M.D., Northwestern University

ACKNOWLEDGMENTS

First and foremost, I would like to thank my advisor, Dr. Andrew Larson for suggesting this research project. It is my fortune that Dr. Larson offers me the opportunity to conduct my research project at Robert H. Lurie Comprehensive Cancer Center, providing exposure to theoretical and practical aspects of MRI research. He created a great research opportunity and a supportive environment for me. During the course of this study, he has provided remarkable insight and experience at critical points, and also granted me the freedom to pursue my own interests. His guidance and continued support provided the opportunity for me to complete this work, as well as in future endeavors, for which I am deeply grateful.

I would like to thank Dr. Omary for his help in the animal studies and invaluable advice from clinic aspects. I also would like to thank Dr. Richard Magin for his valuable suggestions and discussions during my study. Special thanks also go to Dr. Sarah White for her clinical opinions, assisting animal procedures and improving the quality of manuscripts. I also want to thank Dr. Xiaohong J. Zhou for his helpful discussion. Thank Drs. Robert Lewandowski, Thomas Royston, Ron Gaba, and David Vaillancourt for valuable suggestions and comments to this work.

I would also like to thank my laboratory members who assist me with many experiments: Dr. Yang Guo, Dr. Zhuoli Zhang, Dr. Weiguo Li, Dr. Daniel Procissi, Dr. Derek West, Dr. Dong-Hyun Kim, Dr. Elias Gounaris, Jodi Nicolai, Jeane Chen, Andrew Gordon, Kathy Harris, Katie Williams, Elizabeth Nealis. Formal lab members provided considerable assistance when I started: Dr. Jie Deng, Dr. Ning Jin, Dr.

Xiaoming Yin, Dr. Dingxin Wang, Rachel Klein, Alexander Sheu, and Dr. Xu Feng. I thank them for the support and friendship.

Thanks are extended to Drs. Xiaoming Bi, Sven Zuehlsdorff, Christopher Glielmi, Shivraman Giri and Bruce Spottiswoode from Siemens Medical Solutions for their helpful discussions about pulse sequence programming.

Appreciations also go to National Institute of Health and Society of Interventional Radiology (Allied Scientist Grant) for providing funding to this project, to University of Illinois at Chicago for providing support through fellowship (Chancellor's Graduate Research Fellowship).

Finally, I would also like to thank my parents, *Hong Wang* and *Hongan Zhang*, whose love and support enabled me to complete this work.

Yue Zhang

TABLE OF CONTENTS

<u>CHAPTER</u>	<u>PAGE</u>
1 INTRODUCTION	1
1.1 CURRENT CHALLENGES OF LIVER TUMOR THERAPIES	1
1.2 SIGNIFICANCE.....	2
1.3 AIMS	3
2 BACKGROUND	5
2.1 HEPATOCELLULAR CARCINOMA	5
2.2 IRREVERSIBLE ELECTROPORATION	6
2.2.1 Tumor Ablation Techniques.....	6
2.2.2 Irreversible Electroporation Ablation	7
2.2.3 Planning and Optimization of IRE Treatment Protocol	10
2.2.4 MRI Guidance of Tissue Ablation Procedures	11
2.3 BASIC MR PHYSICS	13
2.3.1 Spin	13
2.3.2 Magnetic Moment and Lamor Equation	14
2.3.3 Equilibrium Alignment of Spin.....	16
2.3.4 The Magnetization	18
2.3.5 Relaxation.....	18
2.3.6 Imaging Contrast Mechanism	20
3 MRI TO ASSESS IMMEDIATE RESPONSE TO IRREVERSIBLE ELECTROPORATION FOR TARGETED ABLATION OF LIVER TISSUES: PRE- CLINICAL FEASIBILITY STUDIES IN RODENT MODEL	21
3.1 INTRODUCTION.....	21
3.2 MATERIALS AND METHODS	22
3.2.1 Experimental Overview.....	22
3.2.2 Animal Model.....	23
3.2.3 MRI Measurements	25
3.2.4 IRE Procedures	25
3.2.5 FEM Simulations	28
3.2.6 Histological Evaluation	29
3.2.7 Data Analysis.....	29

TABLE OF CONTENTS (continued)

<u>CHAPTER</u>	<u>PAGE</u>
3.2.8 Statistical Analysis	30
3.3 RESULTS.....	31
3.3.1 MRI Measurements	31
3.3.2 Histology	36
3.3.3 Evaluation of Relationship between FEM-Predicted, MRI-Monitored, and Histology-Confirmed IRE Ablation Zones	40
3.4 DISCUSSION.....	46
4 MRI-BASED 3D FINITE ELEMENT MODELING FOR PREDICTION OF IRREVERSIBLE ELECTROPORATION ABLATION ZONES IN A RAT LIVER TUMOR MODEL	51
4.1 INTRODUCTION.....	51
4.2 MATERIALS AND METHODS	51
4.2.1 Tumor Cell Culture	51
4.2.2 Animal Model.....	52
4.2.3 MRI Measurements	53
4.2.4 IRE Procedures	54
4.2.5 Histology.....	54
4.2.6 FEM Simulation	55
4.2.7 Statistical Analysis.....	55
4.3 RESULTS.....	55
4.4 DISCUSSION.....	59
5 MULTI-MODALITY IMAGING TO ASSESS IMMEDIATE RESPONSE TO IRREVERSIBLE ELECTROPORATION IN A RAT LIVER TUMOR MODEL	61
5.1 INTRODUCTION.....	61
5.2 MATERIALS AND METHODS	63
5.2.1 Experimental Overview.....	63
5.2.2 Tumor Cell Line and Culture.....	63
5.2.3 Animal Model.....	64
5.2.4 IRE Procedures	64
5.2.5 Multi-Modality Imaging.....	65
5.2.6 Histological Evaluation	68

TABLE OF CONTENTS (continued)

<u>CHAPTER</u>	<u>PAGE</u>
5.2.7 Data Analysis.....	69
5.2.8 Statistical Analysis.....	69
5.3 RESULTS.....	70
5.3.1 Multi-Modality Imaging.....	70
5.3.2 Hepatic Ligation.....	76
5.3.3 Histology.....	78
5.3.4 Statistics	84
5.4 DISCUSSION.....	84
6 DIFFUSION-WEIGHTED MRI FOR MONITORING IRREVERSIBLE ELECTROPORATION ABLATION OF HEPATOCELLULAR CARCINOMA IN A RODENT MODEL	87
6.1. INTRODUCTION.....	87
6.2. MATERIALS AND METHODS	89
6.2.1. Tumor Cell Line and Culture.....	89
6.2.2. Animal Model.....	89
6.2.3. MR Imaging	90
6.2.4. IRE Procedures	92
6.2.5. Histological Evaluation	92
6.2.6. Data Analysis.....	93
6.2.7. Statistical Analysis.....	94
6.3. RESULTS.....	94
6.3.1. MRI Measurements	94
6.3.2. Histology.....	101
6.3.3. Comparison of SNR, T2 and ADC between pre- and post-IRE	105
6.4. DISCUSSION.....	105
7. SUMMARY AND FUTURE DIRECTIONS	109
REFERENCES.....	112
VITA	122

LIST OF TABLES

<u>TABLE</u>	<u>PAGE</u>
Table 3.1: MRI and Histological Measurements of IRE Ablation Zone.....	42
Table 4.1: MRI Parameters of T2W TSE	53
Table 5.1: MRI Parameters of T1W GRE and T2W TSE	67
Table 6.1: MRI Parameters.....	91

LIST OF FIGURES

<u>FIGURE</u>	<u>PAGE</u>
Figure 2.1: Two categories of electroporation	8
Figure 2.2: Magnetic moment in an external field	15
Figure 2.3: Spins alignments without (A) and with (B) an external magnetic field. A shows that the total magnetization is 0 with no external field; B shows spin vectors align parallel or anti-parallel with the external magnetic field.	17
Figure 2.4: The magnetization relaxation process after it is tipped to x-y plane by an rf pulse.....	19
Figure 3.1: IRE electrodes and its holder	24
Figure 3.2: Animal remained fixed in supine position	26
Figure 3.3: Electroporator ECM830	27
Figure 3.4: Representative T1W GRE images (A, B) and T1W (C, D), T2W (E, F), and PDW (G, H) TSE images acquired before (Pre-IRE) and immediately after (Post-IRE) the application of 2500V IRE pulses. These images were acquired along an orientation perpendicular to the IRE electrodes; bipolar electrode positions were depicted as signal voids. MRI-monitored IRE ablation zones were hypo-intense within T1W images and hyper-intense within both T2W and PDW images.	32
Figure 3.5: Representative T1W GRE images (A, B) and T1W (C, D), T2W (E, F), and PDW (G, H) TSE images acquired before (Pre-IRE) and immediately after (Post-IRE) the application of 2500V IRE pulses. These images were acquired along an orientation parallel to the IRE electrodes; bipolar electrode positions were depicted as signal voids.	

MRI-monitored IRE ablation zones were hypo-intense within T1W images and hyper-intense within both T2W and PDW images. 34

Figure 3.6: Representative hematoxylin-eosin (H&E) histology slide images for one rat that was sacrificed immediately after 2500V IRE procedures. A low magnification image (x2.5) with large FOV (A) and x25 magnification image (B) from inset (dashed box within A) each show no clear morphological changes but eosinophilic cytoplasmic changes within IRE ablation zones. 37

Figure 3.7: A representative x25 magnification image from H&E slide for rat sacrificed 24 hours post-IRE shows a well-delineated boundary between untreated and ablated tissues with cellular necrosis within ablation zone..... 39

Figure 3.8: FEM-anticipated IRE ablation zones (A-C), post-IRE T1W GRE images (D-F) and corresponding H&E pathology slides from livers harvested 24hrs post-IRE (G-I) following IRE procedures with electrode voltages of 1000V, 1500V and 2500V (top, middle, and lower rows, respectively)..... 41

Figure 3.9: Scatterplots showing the relationship between intra-procedural MRI-based IRE ablation zone measurements and FEM-anticipated ablation measurements. Intra-procedural MRI-based IRE ablation zone measurements were highly consistent with FEM-anticipated ablation zones with intra-class correlation coefficients > 0.90 , $p < 0.001$ for both T1W (A) and T2W (B) measurements..... 44

Figure 3.10: Scatterplots showing the relationship between intra-procedural MRI-based IRE ablation zone measurements and histology-confirmed IRE ablation zone measurements. Intra-procedural MRI-based IRE ablation zone measurements were highly correlated with with histology-confirmed measurements of the IRE ablation zone

24hrs post-therapy with Spearman correlation coefficient $\rho = 0.90$ for T1W (A) and $\rho = 0.91$ for T2W (B) measurements (both, $p < 0.001$)..... 45

Figure 4.1: Representative images for Group A (left). T2W images (A and B, blue dashed circle for liver, white arrows for electrodes and yellow arrow for tumor), reconstructed 3D liver and tumor(C), axial view of 3D model (D), FEM simulated ablation zone (E, blue region) and histology-confirmed ablation zone (F, white circle).56

Figure 4.2: Representative images for Group B. (above) T2W images (A and B, blue dashed circle for liver, white arrows for electrodes and yellow arrow for tumor), reconstructed 3D liver and tumor (C), axial view of 3D FEM model (D), simulated ablation zone (E, blue region) and histology-confirmed ablation zone (F, white circle). Yellow circle indicated untreated tumor growing into surrounding normal liver. 57

Figure 4.3: Scatterplots show the relationship between FEM-simulated IRE ablation zone and histology-confirmed IRE ablation zones. 58

Figure 5.1: Representative multi-modality images for pre-IRE and post-IRE in normal hepatic parenchyma. On 30 min Post-IRE US(B), a hypoechoic region foci was noted in the liver parenchyma (white cross); Red arrow indicated the probe position (hyperechogenicity related to introduction of air into the liver with probe placement). On post-IRE CT(D), a hypoattenuate region appeared as the ablation zone. The ablation zone was visualized as hypointensity within T1W (F) and hyperintensity within T2W MRI(H)..... 72

Figure 5.2: Representative multi-modality images for pre-IRE and post-IRE in tumors. Within Pre-IRE US (A), the tumor (yellow plus) appeared as hyperechoic peripherally and isoechoic centrally (when compared to normal hepatic parenchyma); Within Post-

IRE US (B), both normal and tumor tissues adjacent to the IRE probe became more hypo-echoic. Red arrow indicated the probe position. The ablation zone appeared as hypoattenuating within post-IRE CT (D) where the tumor boundary could no longer be noted. A hypointense ablation zone appeared within post-IRE T1W (F). A hyperintense region of ablated normal tissues appeared surrounding the central hyperintense tumor within T2W (H). 74

Figure 5.3: T1W GRE images (A,B) and T2W (C,D) TSE images acquired before (Pre-IRE) and immediately after (Post-IRE) the application of 2500V IRE pulses in rat with ligated port vein and hepatic artery. Notice the conspicuous lack of post-IRE T1W and T2W signal alterations compared to the post-IRE signal changes clearly apparent within those images presented in **Fig.5.1**. 77

Figure 5.4: Representative H-E–stained histology slides for normal liver ablation in rats sacrificed 30minutes (A) and 24 hours after IRE procedures (B). The 24-hour staining (B) showed a more clear ablation zone than immediate one (A). The morphology of the cell nuclear immediately after IRE (D) showed no clear change compared to unablated tissues (C), but small amount of red blood cells appeared in some extracellular spaces. After 24 hours (E), red blood cells were filled in most extracellular spaces and sinusoidal space and nuclear lost their normal morphology by becoming shrinked, indicating cell necrosis. 79

Figure 5.5: Representative H-E–stained histology slides for tumor ablation in rats those were control (A,B), sacrificed 30minutes (C,D) and 24 hours after IRE procedures (E,F). The tumor cells arranged loosely within both 30 minutes (D) and 24 hours(F) compared

to control tumor cells (B). Some nucleus agglutinations can be seen at 30 minutes; nuclear cytoplasm ratio increases 24 hours after IRE. 80

Figure 5.6: TEM images for normal liver ablation. Normal complete cell membrane, nucleus membrane and cell organelles are clear seen in untreated liver tissue (A, B). 30 minutes after IRE (C, D), pores on nuclear membrane are observed while cell membrane disappeared, but most organelles remain their structure. 24 hours after IRE (E, F), cell and nucleus boundaries are not observed; most organelles lose their structure. 82

Figure 5.7: TEM images for tumor ablation. Untreated tumor cells have a larger nucleus and complete cell membrane and nucleus membrane can be noted (A, B). 30 minutes after IRE (C, D), pores on nuclear membrane are observed while cell membrane disappeared, but most organelles remain their structure. 24 hours after IRE (E, F), cell boundary can no longer be noted; most organelles lose their structure, nucleolus decrease and vacuolar degeneration is seen in cytoplasm. 83

Figure 6.1: Representative T1W MRI before and after IRE within normal liver parenchyma (A and B) and tumor liver (C and D). Ablated normal tissue appeared as hypo-intensity within post-IRE T1W (B). A large hypo-intensity zone appeared to cover the tumor for tumor ablation (D). 95

Figure 6.2: Representative multiple-echo TSE T2W MRI and the corresponding T2 maps before (A, B and C) and after IRE (D, E and F) within normal liver parenchyma. Ablated normal tissue appeared as slightly hyper-intensity within post-IRE T2W at TE = 12.6 ms (D) and hyper-intensity at TE = 44.1 ms (E). T2 maps indicated increased T2

within ablated normal tissues. In this case, average T2pre = 20.93 ms, and T2post = 32.77 ms. 97

Figure 6.3: Representative multiple-echo TSE T2W MRI and the corresponding T2 maps before (A, B and C) and after IRE (D, E and F) for a tumor liver ablation. A large ablation zone appeared as hyper-intensity to cover the tumor within both post-IRE T2W at TE = 12.6 ms (D) and at TE = 44.1 ms (E). Small colored T2 maps overlaid with gray-scale T2maps (C and F) indicating decreased T2 within tumor after IRE. In this case, average tumor T2pre = 51.59ms, and T2post = 35.76ms. 98

Figure 6.4: Representative DW MRI and the corresponding tumor ADC maps before (A, B and C) and after IRE (D, E and F) for a tumor liver ablation. The DW signal intensity within the tumor decayed less than that within the normal liver within both DW images at b = 500 s/mm². The tumor region ADC maps overlaid with DW image at b = 0, indicating decreased ADC within tumor after IRE. In this case, average tumor ADCpre (1.788±0.662)×10⁻³mm²/s = , and ADCpost = (1.386±0.505)×10⁻³mm²/s..... 100

Figure 6.5: Representative H&E staining for a normal liver sacrifice 1 day after IRE. The region overview showed a well-delineated boundary between untreated and ablated tissues with cellular necrosis within ablation zone (A: original magnification ×2.5). A detailed view within the ablation zone showed nuclear degeneration and remarkable hemorrhage was observed (B: original magnification ×100). 102

Figure 6.6: Representative H&E staining for a tumor sacrifice immediately after IRE. Tissue necrosis was not clearly observed within the ablation zone (A: original magnification ×20). A detailed view within the tumor indicated cellular swelling (white arrows), no hemorrhage was observed (B: original magnification ×100)..... 103

Figure 6.7: Representative H&E staining for a tumor sacrifice 1 day after IRE. The region overview showed a well-delineated boundary between untreated and ablated tissues with cellular necrosis within ablation zone (A: original magnification $\times 20$). A detailed view within the tumor showed tumor cells became loosely arranged. More extracellular space appeared and no hemorrhage was observed. (B: original magnification $\times 100$)..... 104

LIST OF ABBREVIATION

DWI	Diffusion Weighted Imaging
FEM	Finite Element Modeling
FISP	Fast Imaging with Steady State Precession
RFA	Radiofrequency Ablation
GRE	Gradient Recall Echo
IRE	Irreversible Electroporation
HIFU	High Intensity Focused-Ultrasound
H&E	Hematoxylin and Eosin
LITT	Laser-Induced Thermotherapy
MRI	Magnetic Resonance Imaging
PEI	Percutaneous Ethanol Injection
RE	Reversible Electroporation
TE	Echo Time
TR	Repetition Time
TSE	Turbo Spin Echo
STIR	Short Inversion Time Inversion Recovery

SUMMARY

Targeted tissue ablation methods have been widely applied to the treatment of metastatic and original tumor. Irreversible electroporation (IRE) is a novel targeted tissue ablation approach by applying external electrical field to increase cell membrane permeability which leads to cell death. IRE has multiple advantages comparing to thermal ablation methods, for example, no heat-sink effect and less damage to large blood vessels. For conventional IRE, pre-procedural planning can be performed with finite element modeling to predict ablated region based on applied voltage and the assumption of homogeneous tissue properties, which might decrease the accuracy for heterogeneous tissue with cirrhotic or tumoral tissue.

In this dissertation, MRI was perform to assess the immediate response to IRE in a rat liver model. IRE-induced MRI signal alterations were observed. MRI-measured IRE ablation zone was highly correlated with histology-confirmed ablation zone. Second, an MRI-based pre-procedural finite element method was developed and applied in a rat liver tumor model. The simulated ablation zone showed a high correlation with histology-confirmed ablation zone. This approach could potentially provide individualized pre-procedural planning for IRE. Third, Multi-modality imaging was perform in a rat liver model to assess the normal tisssue response and tumor response. The echogenecity changes for Ultrasound, the hounsfield units for CT and signal-to noise ratios for MRI were measured. At last, diffusion-weighted and multiple echoes T2-weighted turbo spin echo MRI were performed before and immediate after IRE in a rat liver tumor model.

Quantitative apparent diffusion coefficient and T2 maps were used to investigate cell membrane permeability change after IRE.

1 INTRODUCTION

1.1 CURRENT CHALLENGES OF LIVER TUMOR THERAPIES

Hepatocellular carcinoma (HCC) is the sixth most common neoplasm worldwide and the fourth leading cause of cancer death in United States. The current curative therapies for HCC are surgical resection and transplantation, which is only suitable for 10-15% patients. Various interventional treatments are developed for unresectable HCC, including transarterial therapy (bland embolization with particles, transarterial chemoembolization, radioembolization) and percutaneous ablative therapy (chemical ablation, thermal ablation). However, these thermal ablation approaches have significant potential limitations, for example, uncontrollable diffusion of chemical agent for chemical ablation, incomplete intra-procedural imaging of the targeted tumor for thermal ablation, and 'heat sink' effects particularly for tumors located near large hepatic blood vessels.

Irreversible electroporation (IRE) is a recently developed tissue ablation technology. IRE utilizes targeted delivery of electrical pulses to induce cell death through cell membrane permeabilization. This non-thermal ablation modality may overcome some of the primary limitations of conventional ablation approaches.

Magnetic resonance imaging guidance methods have already been widely advocated for intra-procedural monitoring of both transarterial therapies and

percutaneous thermal ablation procedures. For percutaneous approaches, MRI-guidance can be used for both real-time, targeted placement of ablation probes as well as functional monitoring of tissue response. While MRI monitoring approach has been applied in IRE ablation, it is critical important to conduct an imaging-pathology correlation study. A 2D finite element method has been used to simulate IRE ablation zone in normal liver; but this conventional approach would be inaccurate for tumor ablation. An individualized pre-procedural planning method will benefit heterogeneous tissues. While recent studies have investigated in large animal model *in vivo*, there is not enough data to demonstrate IRE ablation in tumor model.

1.2 SIGNIFICANCE

IRE has demonstrated notable potential as a tumor ablation modality with several benefits over current thermal ablation approaches. However, further pre-clinical studies in liver tumor animal models are necessary to validate intra-procedural imaging methods, which will be critical to permit 'patient-specific' optimization of IRE procedures. The long-term clinical impact of these studies should be significant:

First, Pre-procedural MRI and 3D FEM studies will permit advanced patient-specific pre-procedural planning of IRE treatment protocols to select optimized voltage and electrode positions;

Second, our studies should potentially provide further understanding of IRE-induced signal alternations and novel imaging techniques for depicting membrane permeabilization during IRE;

Third, Intra-procedural image-guided IRE monitoring techniques should permit patient-specific protocol optimization to both reduce liver toxicity and improve therapy response.

1.3 AIMS

The broad, long-term objective of this doctoral work is to improve the prognosis of patients with unresectable HCC. The immediate objective was to develop a serial of MRI techniques to assess liver tumor response after IRE ablation in a rodent model. Specifically, this dissertation addressed the following four aims.

Aim One

To investigate the feasibility of assessing immediate response to IRE of liver tissues by MRI

T1-weighted turbo spin echo (TSE), T1-weighted gradient-recalled echo, T2-weighted and proton-weighted TSE imaging were performed before and immediately after IRE in a rat liver model. MRI-based ablation zones were measured and to correlate with histology-based ablation zones.

Aim Two

To develop a MRI-based 3D finite element method for prediction of IRE ablation zones

T2-weighted TSE sequence was performed in a rat liver tumor model before IRE. These MR images were used to create a finite element method model to predict IRE ablation zone.

Aim Three

To evaluate the immediate tumor response to IRE by multi-modality imaging

Ultrasound, CT and MRI were performed in a rat liver tumor model before and after IRE. Ultrasound scoring were performed, Hounsfield unite was measured for CT and signal-to-noise ratio was measured for MRI

Aim Four

To monitor IRE ablation of HCC by diffusion-weighed MRI

Diffusion-weighed MRI sequence was performed before and immediately after IRE ablation in a rat liver tumor model. The apparent diffusion coefficient of tumor was measured to investigate cell membrane permeability change due to elctroporation.

2 BACKGROUND

2.1 HEPATOCELLULAR CARCINOMA

Hepatocellular carcinoma (HCC), a primary malignant cancer of the liver, is the sixth most common neoplasm in the world (1) and is fourth leading cause of cancer death in United States(2, 3). It is estimated that there will be 30,640 new cases diagnosed and 21,670 deaths due to this disease in the United States in 2013(4). The main risk factors for HCC are hepatitis B, hepatitis C viruses, alcoholism. liver cirrhosis is the strongest predicting factor of HCC(5). Alpha-fetoprotein (AFP) level was used as serum marker of HCC. But recent study indicated AFP was not a sensitive marker to detect HCC since AFP is not elevated in all patients with HCC(6). Enrolling patients who are at high risk for development in a regular surveillance program (usually using ultrasound imaging every six months) with patients who are at high risk for tumor development (hepatitis B carriers) is the only way to early diagnose HCC (7). Over 60% of HCC in clinical practice are diagnosed at the late stage.(8) HCC at its late stage is featured by aggressive growth, metastases, low survival rates(9). Surgical resection offers the best prognosis for long-term survival, but only 10-15% of patients are suitable for surgical resection(10). Resection in cirrhotic patients carries high morbidity and mortality (11, 12). Liver transplantation can be a curative approach for patients with advanced HCC without extrahepatic metastasis (13). Patient selection is a major key for successful transplantation (14).

Therefore most regional therapies (nonsurgical) are developed to provide palliative treatment rather than a cure(15).

2.2 IRREVERSIBLE ELECTROPORATION

2.2.1 Tumor Ablation Techniques

The targeted tissue ablation is considered as minimally invasive technique for local treatment of HCC. These approaches include percutaneous ethanol injection (PEI), radiofrequency ablation (RFA), laser interstitial thermal ablation and cryo-ablation. PEI was introduced as the seminal tissue ablation technique in the 1980s. Radiofrequency ablation (RFA) was first introduced in fresh liver from a bovine cadaver and now has become the most widely used tissue ablation method due to improved regional control compared to alternatives approaches such as PEI. However, the thermal ablation methods have several significant potential limitations: asymptomatic pleural effusion(16), pneumonia(17), tumor seeding(18), incomplete imaging of the targeted tissue due to boiling bubbles and vapor, 'heat sink' effects particularly for tumors located near large hepatic blood, indistinct margins between treated and untreated tissues. While thermal ablation approaches, like RFA and cryo-ablation, have gained wide acceptance for the tissue ablation, these critical drawbacks still keep limiting overall efficacy. Irreversible electroporation (IRE) is a powerful new tissue ablation technology that may overcome some of the primary limitations of thermal ablation approaches.

2.2.2 Irreversible Electroporation Ablation

2.2.2.1 Electroporation

Electroporation, is a significant increase in the permeability of the cell membrane caused by an externally applied electrical field. The increase in membrane permeability is associated with the formation of nano-scale pores in the cell membrane, which led to the naming of “electroporation”. The pores created by external pulses facilitate the exchange between intracellular and extracellular components. The electroporation depends on the transmembrane electrical field at each point of the cell membrane. The local electrical field is generally determined by the pulse voltage, duration and shape. The subsequent behavior of pores is determined by the magnitude of electrical field, which divides electroporation into two categories. When the electrical field is not strong enough, these pores close shortly after application of the electrical field. It is known as Reversible Electroporation (RE). The phenomenon of RE has already widely applied in introducing macromolecules into the cell whose membrane is normally impermeable (19), which is known as gene transfer. People applied RE to introduce exterior gene into murine melanoma cell (20), which was termed as electrogenetherapy. RE was also used to increase the delivery of chemotherapeutic drugs like cisplatin and bleomycin into cancer cells to enhance the efficacy of treatment (21, 22), which was named as electrochemotherapy. In these applications of RE, the cells have a good chance to survive because the pores are able to reseal after the removal of electric field (23).

However, when the electrical field across the cell membrane is sufficiently strong, the pores do not reseal leading to a loss of homeostasis and eventual cell death, a process recently described as irreversible electroporation (IRE). Figure 1 illustrated these two categories of electroporation.

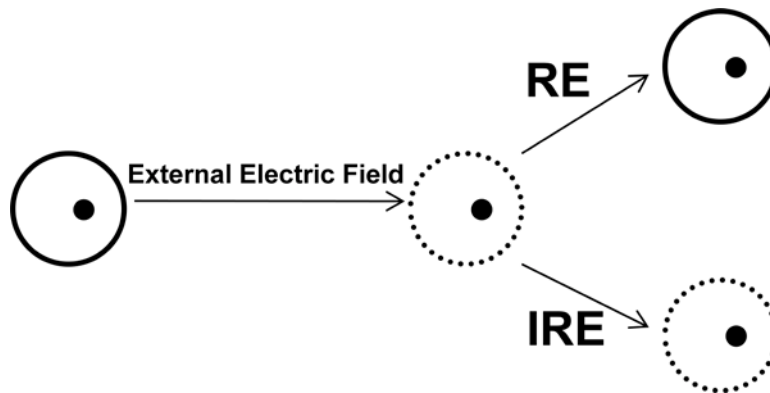


Figure 2.1: Two categories of electroporation

2.2.2.2 IRE as a Novel Ablation Approach

IRE was first introduced as a potential tissue ablation technique in 2005(24). In this approach, electrical pulses were targeted delivered to induce cell death through cell membrane permeabilization. Previous studies have demonstrated that IRE can ablate large volumes of tissue without inducing thermal effects; IRE can therefore serve as a novel ablation modality independent of prior thermal ablation approaches.

IRE has gained more attentions recently as a tissue ablation approach. In 2005, IRE was performed in vitro to ablate human hepatocarcinoma cells (HepG2), where multiple electrical pulses produced complete cancer cells ablation(25). It was reported IRE was applied to ablate normal liver parenchyma in a rat model in vivo in 2006, in which treated tissues exhibited microvascular occlusion and endothelial cell necrosis while intact large blood vessels(26). In 2007, people performed IRE methodology in normal swine liver and found that the structure of bile ducts, blood vessels and connective tissues remains intact with IRE(27).

Previous studies have demonstrated that IRE has significant advantages over existing ablation methods. The IRE procedures only need less than 1s for the application of a short series of microsecond electrical pulses for tissue ablation(26). IRE induces a distinctive boundary between ablated and viable tissues at the position where the magnitude of the electrical field (E-field) falls under the lethal dose threshold (26, 28). Importantly, IRE does not suffer from the 'heat-sink' effect that is generally problematical for thermal ablation methods resulting in detriment of surrounding

undesired tissues and blood vessels (29, 30). IRE fields can be modeled numerically to anticipate the affected region (24, 31). Other potential advantages include tumor specific immunological reaction (32) and little impact upon the collagen network within tissues(30). Particularly IRE can potentially abate tumor tissues close to large vessels, which would make this novel ablation therapy an attractive approach for the treatment of primary and metastatic liver cancer.

2.2.3 Planning and Optimization of IRE Treatment Protocol

2.2.3.1 Current Pre-Procedural Planning of IRE Treatment Protocol

For current IRE procedure, finite element modeling (FEM) can be used to calculate the E-field distribution for pre-procedural planning of the optimization of applied voltage and electrode spacing. The FEM approaches of electroporation are generally based on the assumption of homogenous tissue conductivity (24). The IRE ablation zones are based on these numerical models and lethal E-field which leads to permanent cell membrane permeabilization (30). However, for liver containing fibrotic, cirrhotic or tumor tissues, this assumption could lead to erroneous approximation of anticipated ablation zone. An imaging approach, electrical impedance tomography (EIT) (33, 34), can measure the electrical impedance distribution within the tissue, which might provide a more accurate representation of tissue conductivity and lead to a better prediction of ablation zones. However, EIT method is limited by complex data acquisition algorithm, image reconstruction algorithm (34) and relative poor spatial resolution. These limitations may decrease the prediction accuracy for IRE in heterogeneous tissues.

2.2.3.2 Current Intra-Procedural Optimization of IRE Treatment

Ultrasound imaging approaches have initially been used to visualize IRE ablation volumes (27). The IRE regions are visualized as hypoechoic appearance in normal liver with gray-scale ultrasound. Although it is feasible to monitor IRE procedures, ultrasound imaging has several limitations in clinic: clinical studies of conventional gray-scale ultrasound show widely conflicting results, with sensitivity ranging from 20-84% (35-38); ultrasound is insensitive for HCC detection in advanced cirrhosis from A prospective study of 200 sonograms (35).

MRI is generally considered a more accurate imaging technique to detect HCC, particularly for smaller lesions (36, 37), due to excellent soft tissue contrast and the ability of non-invasive monitoring temperature changes during RFA and cryo-therapy. Therefore, I propose the use of MRI for intra-procedural monitoring the tissue response after IRE procedural, which allows rapid adjustments of treatment strategy to achieve optimized outcome.

2.2.4 MRI Guidance of Tissue Ablation Procedures

MRI guidance methods have already been widely advocated for intra-procedural monitoring of both percutaneous and high-intensity focused-ultrasound (HIFU) tissue ablation procedures (39, 40). MRI-guidance can be used for both real-time, targeted placement of ablation probes and functional monitoring of tissue response in percutaneous procedures. For thermal ablation procedures, electrodes insertion can be performed during acquisition of images with fast imaging with steady state precession

(FISP) or true FISP. The thermal lesion formation during the ablation session can be monitored with rapid turbo spin echo (TSE) T2-weighted and turbo short inversion time inversion recovery (STIR) sequences obtained intermittently during the ablation (41, 42). These lesions are typically depicted as low signal on T2-weighted or STIR images and non-enhancing on T1-weighted contrast-enhanced images (42-44). Quantitative measurements can be also served to monitor the treatment response in thermal ablation procedures; these measurements are generally based on quantitative T1, and diffusion (44-46).

For cryo-ablation, MRI can be used to in vivo depict the formation of the entire iceball (47-51) by offering an entire circumference of the cryo-effect and without creating a shadow artifact (49, 50, 52). MRI measurements of cryo-ablated lesions can be used to accurately predict the proximal outer boundary of tissue necrosis within 1–5 mm (51). Intra-procedural MR images typically visualize ice-balls as sharply marginated regions of signal loss on fast spin-echo, spin-echo, and gradient-echo MR images. Intra-procedural MRI measurements of ice-ball locations are well correlated with post-procedural histological measurements of cryo-necrosis (53).

For laser-induced thermotherapy (LITT), MR thermometry methods can permit real time online monitoring temperature alteration during treatment. The laser-induced lesion can be visualized as hypo-intense T2-weighted MR images. MR images of post-LITT prostate has shown that coagulated tissues delineate well from viable surrounding tissues not only on contrast enhanced T1-weighted images (54-56), but also on T2-

weighted images, where low signal intensity indicates areas of coagulation(55, 57).

Dynamic and static contrast-enhanced MR imaging can be also used to estimate the degree of resultant necrosis (58).

Diffusion-weighted MRI (DWI) has been used to assess tissue damage in many applications, including prostate cryo-ablation (59), HIFU-treated uterine fibroid(60), osteogenic sarcoma(61), and liver tumor undergoing chemoembolization(62). The apparent diffusion coefficient (ADC) decrease occurred early during the course of the treatment, but the ADC increased as the tissue recovered and regenerated over time in a canine prostates model (63). DWI has been shown to be very sensitive to cell death and tissue damage (59-62), particularly during targeted ablation therapies.

Therefore, we anticipate that MRI methods should also permit intra-procedural monitoring of tissue response during IRE ablation. In this thesis, I performed an in vivo study to test if MRI approaches can be used to visualize tissue response after IRE, which will allow rapid adjustments of treatment strategy to achieve optimized outcome.

2.3 BASIC MR PHYSICS

2.3.1 Spin

Spin is a fundamental intrinsic property of elementary particles and atomic nuclei (64). Electrons, protons, and neutrons possess spin, which is counted in multiples of $1/2$ and can be positive or negative. For individual unpaired electrons, protons and neutrons, each possesses a spin of $1/2$. Human body is largely composed of water molecules.

Each water molecule has two hydrogen nuclei (protons). MRI is based on the interaction of a proton spin with an external magnetic field, \vec{B}_0 .

2.3.2 Magnetic Moment and Larmor Equation

To easily understand the basic motion of the proton spin, we can image that an electrically charged particle is rotating around its axis like a spinning gyroscope. So it looks like an effective loop of electrical current around the same axis about which it is spinning. The strength with which the loop interacts with an external field is named as 'magnetic dipole moment' vector $\vec{\mu}$ (**Figure 2**). The direction of this vector is along the spin axis. The magnetic moment vector will tend to align itself along any external static magnetic field (65). The precession angular frequency for the proton magnetic moment vector is given by

$$\omega_0 = \gamma \cdot B_0 \quad (\text{Eqn. 2.1})$$

where γ is a constant called the gyromagnetic ratio ($\gamma = 2.68 \times 10^8$ rad/s/Tesla for the hydrogen proton in water). This precession frequency ω_0 at a specific external magnetic field is referred to as the Larmor frequency and Equation (3.1) is referred to as the Larmor equation (65).

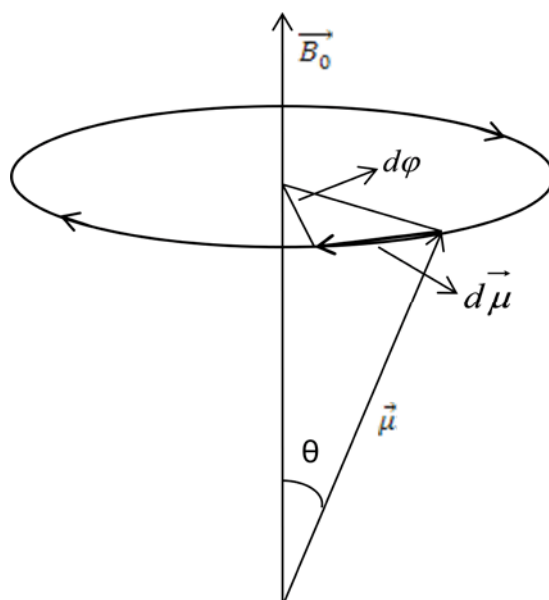


Figure 2.2: Magnetic moment in an external field

2.3.3 Equilibrium Alignment of Spin

For a single proton, its magnetic moment vector will tend to align itself along any external static magnetic field (65). The alignment level (the same orientation, anti-orientation or partial alignment with \vec{B}_0) is associated with the absolute temperature T . At human body temperatures, the thermal energy is millions of times larger than the quantum energy difference for parallel alignment (lower energy) versus anti-parallel alignment (higher energy). When a large number of spins are placed in an external magnetic field, the spin vector will align in one of two possible orientations, parallel or anti-parallel to the outer field, corresponding to a low energy state and a high energy state (**Figure 2.3**). According to Boltzmann distribution in thermal dynamics, the number of spins in the lower energy level slightly exceeds the number of spins in the higher energy level:

$$\frac{N_h}{N_l} = e^{-\frac{\gamma h B_0}{kT}} \quad \text{(Eqn. 2.2)}$$

where N_h is the number of spins in the higher energy level, N_l is the number of spins in the lower energy level, k is Boltzmann's constant and h is Planck's quantum constant. Due to Avogadro numbers of protons in a few grams of tissue, the average magnetic moment vector along the external field (Known as longitudinal equilibrium magnetization) is measurable to detect signals.

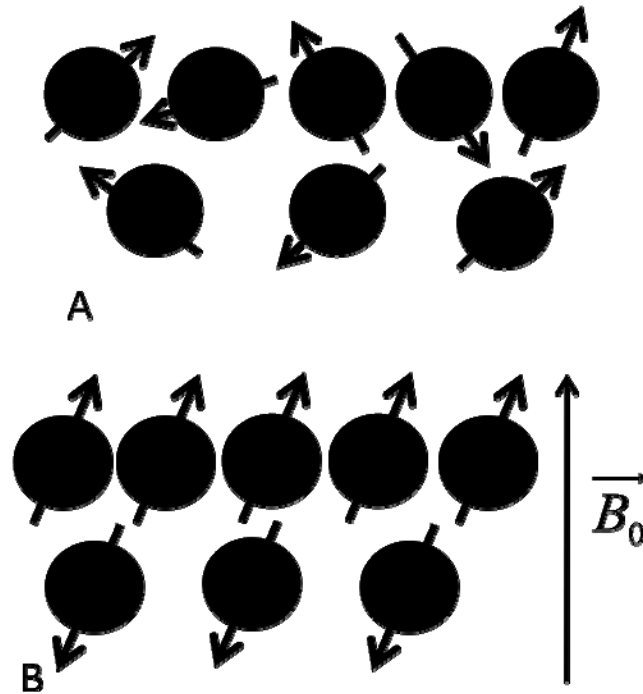


Figure 2.3: Spins alignments without (A) and with (B) an external magnetic field. A shows that the total magnetization is 0 with no external field; B shows spin vectors align parallel or anti-parallel with the external magnetic field.

2.3.4 The Magnetization

A single magnetization vector (\vec{M}_0) represents the vector sum of all spin magnetic moments in the same external magnetic field. The magnetization can be rotated away from its alignment along B_0 axis by applying a radiofrequency (rf) magnetic field within a short time. An rf pulse applied in the plane orthogonal to \vec{B}_0 (referred as “transverse plane”) will rotate the original longitudinal magnetization by a certain flip angle which is dependent on the strength and duration of the rf pulse. After the rf pulse is removed, the resulting tipped magnetization will tend to align back to \vec{B}_0 , where signal can be detected in this process and which can be described as longitudinal relaxation and transverse relaxation(66).

2.3.5 Relaxation

The tipped magnetization (\vec{M}) can be decomposed into two components: longitudinal and transverse components. The longitudinal components (M_z) will grow back along the direction of B_0 and the time of this regrowth is used to characterize this process as “T1”, “longitudinal relaxation time” or “spin-lattice relaxation time” due to the interaction between spins and their atomic neighborhood. The transverse components (M_{xy}) will decay away and the time of this dephase is used to characterize this process as “T2”, “transverse relaxation time” or “spin-spin relaxation time”. The relaxation process can be mathematically described by *Bloch Equation* (65):

$$\frac{d\vec{M}}{dt} = \gamma \vec{M} \times \vec{B}_0 + \frac{1}{T_1} (\vec{M}_0 - \vec{M}_z) + \frac{1}{T_2} \vec{M}_{xy} \quad \text{(Eqn. 2.3)}$$

Solve this equation in z direction in xy plane, respectively, we can have

$$M_z(t) = M_0 + (M_z(0) - M_0) \cdot e^{-\frac{t}{T_1}} \quad (\text{Eqn. 2.4})$$

$$M_{xy}(t) = M_{xy}(0) \cdot e^{-\frac{t}{T_2}} \quad (\text{Eqn. 2.5})$$

The spiral course in **Figure 2.4** is the pictorial solution for Bloch equation (3.3).

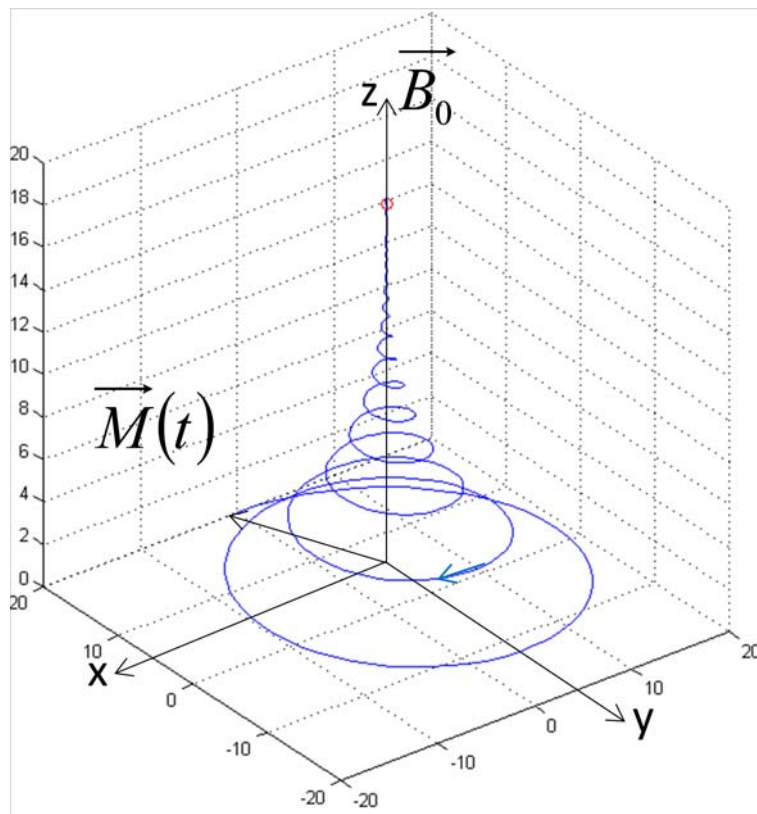


Figure 2.4: The magnetization relaxation process after it is tipped to x-y plane by an rf pulse

2.3.6 Imaging Contrast Mechanism

The most fundamental contrast generating mechanisms are based on proton density, T_1 and T_2 differences between tissues. We can achieve different imaging contrasts by changing the repetition time (TR) and echo time (TE): The signal is main dependent on T_1 by using relatively short TR and very short TE ($\ll T_2$), which is T_1 -weighted imaging; the signal is main dependent on T_2 by using very long TR ($\gg T_1$) and relatively long T_2 , which is T_2 -weighted imaging; the signal is main determined by proton density by using very long TR and very long TE, which is proton-density-weighted imaging.

3 MRI TO ASSESS IMMEDIATE RESPONSE TO IRREVERSIBLE ELECTROPORATION FOR TARGETED ABLATION OF LIVER TISSUES: PRE- CLINICAL FEASIBILITY STUDIES IN RODENT MODEL

3.1 INTRODUCTION

Electroporation involves the application of a short-lived electrical field across the cell membrane to create nano-scale pores thereby increasing membrane permeability (67). Typically these pores close shortly after application of the electrical field; this reversible electroporation phenomenon has been widely used to facilitate gene transfer (68-70) and drug delivery (71, 72). However, when the electrical field across the cell membrane is sufficiently strong, the pores do not reseal leading to a loss of homeostasis and eventual cell death, a process recently described as irreversible electroporation (IRE) (27). Recently, IRE has been applied as a tissue ablation modality (26, 27, 29, 73). IRE may offer multiple potential advantages compared to commonly used radio-frequency thermal ablation (RFA) approaches for the treatment of hepatic lesions. Unlike RFA approaches, IRE methods do not suffer from heat-sink effects that can lead to indistinct margins between treated and untreated tissues (27, 73), under-treatment of targeted tissues, and potential damage to adjacent blood vessels (29).

Finite element modeling (FEM) can be used to anticipate IRE ablation volumes based upon electrode positions and the applied electrode voltage (31). However, these modeling procedures typically assume homogenous tissue conductivity; unknown anisotropic and/or heterogeneous tissue conductivities within fibrotic, cirrhotic, and/or

tumor containing liver tissues could conceivably lead to erroneous pre-procedural approximation of the anticipated ablation volume. Imaging guidance may be important to enable immediate visualization of IRE ablation zones thereby permitting patient-specific intra-procedural adjustments to the treatment protocol.

MRI guidance methods have already been advocated for intra-procedural monitoring of tumor ablation procedures due to excellent soft tissue contrast and the ability to non-invasively monitor temperature changes during RFA and cryotherapy (43, 45, 74). Previously, MRI has been used to visualize electrical shock trauma within muscle tissues; during these studies muscle tissues subjected to high voltage electrical shocks demonstrated significantly increased signal intensity within T2-weighted MRI images (75-77). Hence, we anticipated that MRI methods may also prove effective for immediate intra-procedural monitoring of tissue response during IRE procedures.

Our purpose was to test the hypothesis that MRI measurements can be used to immediately detect treated tissue regions after irreversible electroporation (IRE) ablation procedures in rodent liver tissues.

3.2 MATERIALS AND METHODS

3.2.1 Experimental Overview

For these studies we performed *in vivo* intra-hepatic IRE procedures in a rat model using multiple electrode voltage levels to achieve a range of different ablation zone sizes. Intra-procedural MRI measurements were performed immediately before and

after application of the IRE pulses. MRI-based measurements of IRE ablation zone sizes were compared to histology-based ablation zone measurements at necropsy. We also simulated the anticipated ablation zone size (for each applied voltage level) with FEM methods. For outcome measures we examined the correlation between MRI and histology-based ablation zone measurements and the correlation between MRI-based and FEM-anticipated ablation zone measurements.

3.2.2 Animal Model

All experiments were approved by the institutional animal care and use committees of University of Illinois at Chicago and Northwestern University. Twenty-two male Sprague-Dawley rats (Charles River, Wilmington, MA) weighing 300-350g were used for these experiments. Four rats were initially used to qualitatively determine the feasibility of using intra-procedural MRI to depict the IRE ablation zones with 2500V pulses applied to the electrodes; these rats were immediately sacrificed after the MRI-monitored IRE procedure. Another eighteen rats were divided into 3 groups and (6 rats/group) each underwent IRE procedures with different electrode voltages applied for each group (1000, 1500, and 2500 V); these rats were survived for 24hrs post-procedure to permit definitive formation of IRE-induced necrotic tissue regions (27, 73). Prior to IRE and MRI procedures, rats were anesthetized with a high limb injection of Ketamine (75-100 mg/kg, Ketaset; Fort Dodge Animal Health, Fort Dodge, IA) and Xylazine (2-6 mg/kg, Isothesia; Abbott Laboratories, North Chicago, IL). Rats were restrained in supine position and the left lateral lobe of the liver exposed with midline incision. Two parallel electrodes with 1cm spacing were inserted into the center of the

left lateral lobe to a depth of approximately 12mm (each electrode was a 35mm length, 0.4mm diameter (1 French) platinum-iridium needle (**Figure 3.1**); 10mm electrode separation was maintained by insertion of the needles through holes drilled within a 15mm thick plastic spacing block).



Figure 3.1: IRE electrodes and its holder

3.2.3 MRI Measurements

All studies were performed using a 3 Tesla clinical scanner (Magnetom Trio, Siemens Medical Solutions, Erlangen, Germany) with 4-element carotid array coils used for signal reception. Electrodes remained positioned within the liver throughout the procedure but were disconnected from the function generator during the MRI scan. Prior to application of the IRE pulses, localization scans were performed to identify separate imaging planes perpendicular and parallel to the electrodes. Next, we acquired pre-IRE T1-weighted (T1W) gradient recalled echo (GRE) images with repetition time/echo time (TR/TE) = 200/2.5ms, flip angle = 90°, slice thickness (TH) = 2mm, field of view (FOV) = 65×150 mm², matrix = 84×192, bandwidth = 500 Hz/pixel and T2-weighted (T2W), proton-density weighted (PDW), and T1W turbo spin-echo (TSE) images with TH= 2mm, FOV = 65×150 mm², matrix = 84×192, bandwidth = 500 Hz/pixel, T2W TR/TE = 3500/60ms, PDW TR/TE = 3500/8ms, and T1W TR/TE = 200/8ms. Images were acquired along orientations both parallel and perpendicular to the electrodes. Immediately following application of the IRE pulses, MRI measurements were repeated.

3.2.4 IRE Procedures

After pre-IRE scan, rats were removed from the scanner bore but remained fixed in supine position within restrain apparatus (rats strapped to form-fitting back board, as in **Figure 3.2**). Electrodes were connected to IRE function generator (Electroporator ECM830; BTX Division of Harvard Apparatus, Holliston, MA) (**Figure 3.3**). For IRE procedures, 1000V to 2500V square wave pulses were applied to the 2 parallel electrodes with following protocol: total number of pulses = 8, duration of each pulse =

100 μ s, and interval between two pulses = 100 ms. Immediately after application of the IRE pulses, electrodes were disconnected and animals returned to the scanner bore for follow-up imaging measurements. For the rats electroporated with 1000V pulses, following initial localization scans, the electrodes were removed prior to follow-up T1W and T2W measurements to permit visualization of IRE ablation zones that were of smaller sizes than the induced magnetic susceptibility-based electrode artifacts.



Figure 3.2: Animal remained fixed in supine position



Figure 3.3: Electroporator ECM830

3.2.5 FEM Simulations

For FEM simulations we used COMSOL Multi-Physics software package (COMSOL, Inc. Burlington, MA), which implements the finite element method to solve partial differential equations. The anticipated electrical field (*E*-field) potentials resulting from application of the IRE pulses was determined by solving the Laplace equation $\nabla(\sigma \nabla \phi) = 0$ where ϕ is the electrical potential and σ the electrical conductivity of surrounding tissues. Our simulations closely followed those described in previous IRE studies (24, 26, 27). Briefly, the liver was approximated as a cylindrically symmetric disk with a 30mm diameter and isotropic and homogeneous tissue conductivity of 0.125 S/m (78). For simplicity, this approximation did not include spatially heterogeneous conductivity properties that could be expected in clinical patients due to the presence of fibrotic and tumor tissues. The parallel two-needle electrode array was positioned at the center of this simulated liver volume. The specified IRE electrode voltage was applied to one of the electrodes while the other electrode was treated as ground. Liver surfaces were assumed electrically insulating. Previous rabbit model studies demonstrated that IRE *E*-field potentials $> 63.7 \pm 4.3$ V/mm are lethal within hepatic parenchyma (28). Therefore, for our IRE FEM simulations we assumed that *E*-field potentials > 68.0 V/mm would be sufficient for tissue ablation; for applied electrode voltages of 1000V, 1500V, and 2500V we measured the area (mm²) within a plane perpendicular to the electrodes that was anticipated to achieve this lethal *E*-field threshold (i.e. ablation zone based upon these FEM simulations).

3.2.6 Histological Evaluation

The initial 4 animals were euthanized immediately after post-IRE MRI scans. An additional 18 animals were euthanized 24 hours after electroporation. These rats were euthanized and livers harvested for subsequent necropsy. Livers were fixed in 10% buffered formaldehyde solution, sliced at 3mm intervals, and embedded in paraffin for histological examination. Liver sections were sliced in 4 μ m thick sections and stained using hematoxylin and eosin (H&E). Histological slides were digitized with an optical magnification image acquisition system (TissueGnostics, Vienna, Austria). These specimens were evaluated by an attending surgical pathologist (G.Y.Y., >10yrs experience) with specialization in gastrointestinal oncology. ImageJ software (NIH) was used to manually draw a region-of-interest circumscribing areas of cellular necrosis within each image to measure the resulting IRE ablation zone for each animal. The areas of these region-of-interest (mm²) were measured for comparison.

3.2.7 Data Analysis

For rats euthanized 24 hours after electroporation, regions of interest were drawn to measure the MRI-monitored ablation zones separately within T2W TSE and T1W GRE images oriented perpendicular to the IRE electrodes. These regions of interest were drawn with the reviewer blinded to the applied IRE electrode voltage for a given set of images. The reviewer, a Certificate of Added Qualification-certified attending interventional radiologist (R.J.L.) with >10yrs experience in liver-directed interventional

oncology procedures, qualitatively selected hypo-intense regions within the T1W images and hyper-intense regions within the T2W images with visual reference to the corresponding pre-IRE images. The areas of these regions-of-interest were measured for comparisons. MRI-based ablation zone measurements were evaluated with respect to both ablation zones anticipated based upon FEM simulations and ablation zones measured within corresponding histology slides.

We also measured the diameter of the electrode artifacts within GRE T1W images and within TSE T2W images (using images aligned perpendicular to the electrodes).

3.2.8 Statistical Analysis

Analysis of variance methods were used to evaluate between group differences in MRI ablation zone measurements (T1W, T2W) for the different IRE voltage groups. Independent *t*-tests were used to compare T1W to T2W MRI-measured IRE ablation zones at each different voltage level. Intra-class correlation was used to evaluate the consistency between intra-procedural MRI measurements and FEM-anticipated ablation zones for the three different voltage levels. Spearman correlation coefficients were used to determine the relationship between MRI measurements and histology-confirmed ablation zone measurements (both continuous variables). These analyses were implemented with the SPSS Version 17 software package (Chicago, IL) with *p*-values less than 0.05 considered statistically significant.

3.3 RESULTS

3.3.1 MRI Measurements

Figures 1 and 2 show representative T1W GRE images and T1W, T2W, and PDW TSE images before and immediately after application 2500V IRE, obtained perpendicular (Fig 3.4) and parallel (Fig 3.5) to the electrodes. IRE impacted tissues were clearly demarcated from surrounding normal hepatic parenchyma; electroporated tissues were hypo-intense within T1W GRE and TSE images but consistently hyper-intense within both PDW and T2W TSE images. The diameter of the electrode artifacts was 3.5 ± 0.3 mm within GRE T1W images and 1.5 ± 0.2 mm within TSE T2W images.

Figure 3.4: Representative T1W GRE images (A, B) and T1W (C, D), T2W (E, F), and PDW (G, H) TSE images acquired before (Pre-IRE) and immediately after (Post-IRE) the application of 2500V IRE pulses. These images were acquired along an orientation perpendicular to the IRE electrodes; bipolar electrode positions were depicted as signal voids. MRI-monitored IRE ablation zones were hypo-intense within T1W images and hyper-intense within both T2W and PDW images.

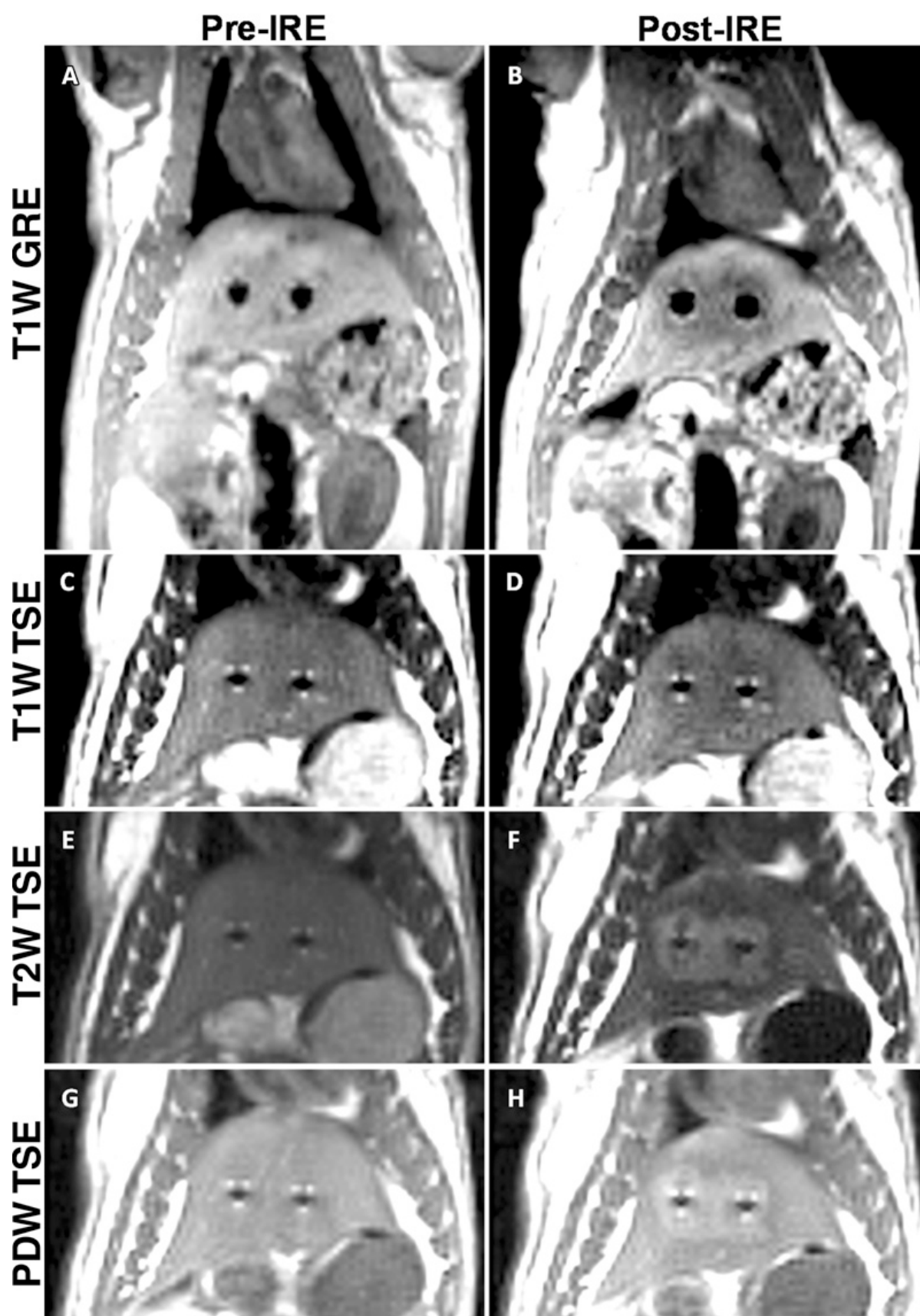
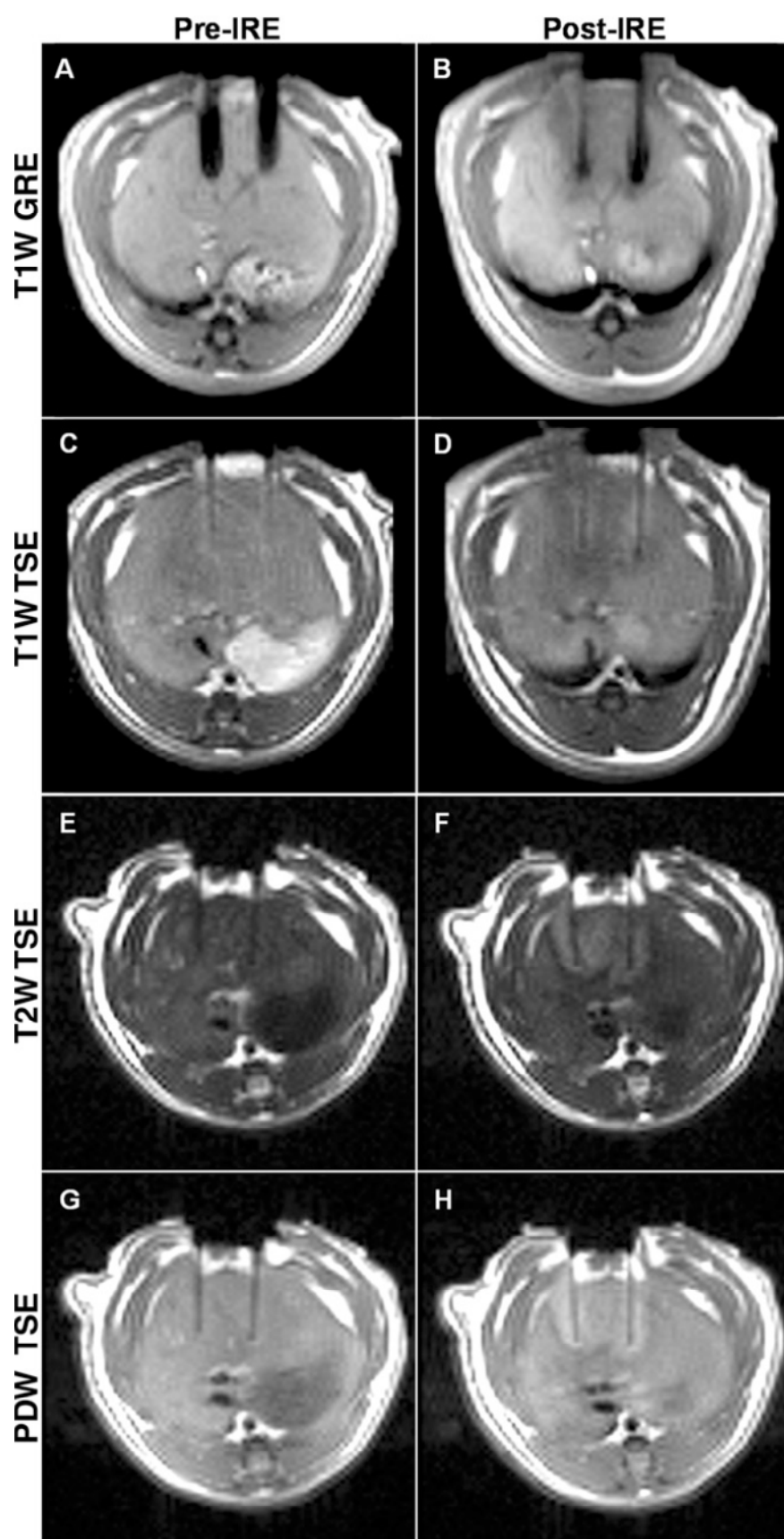


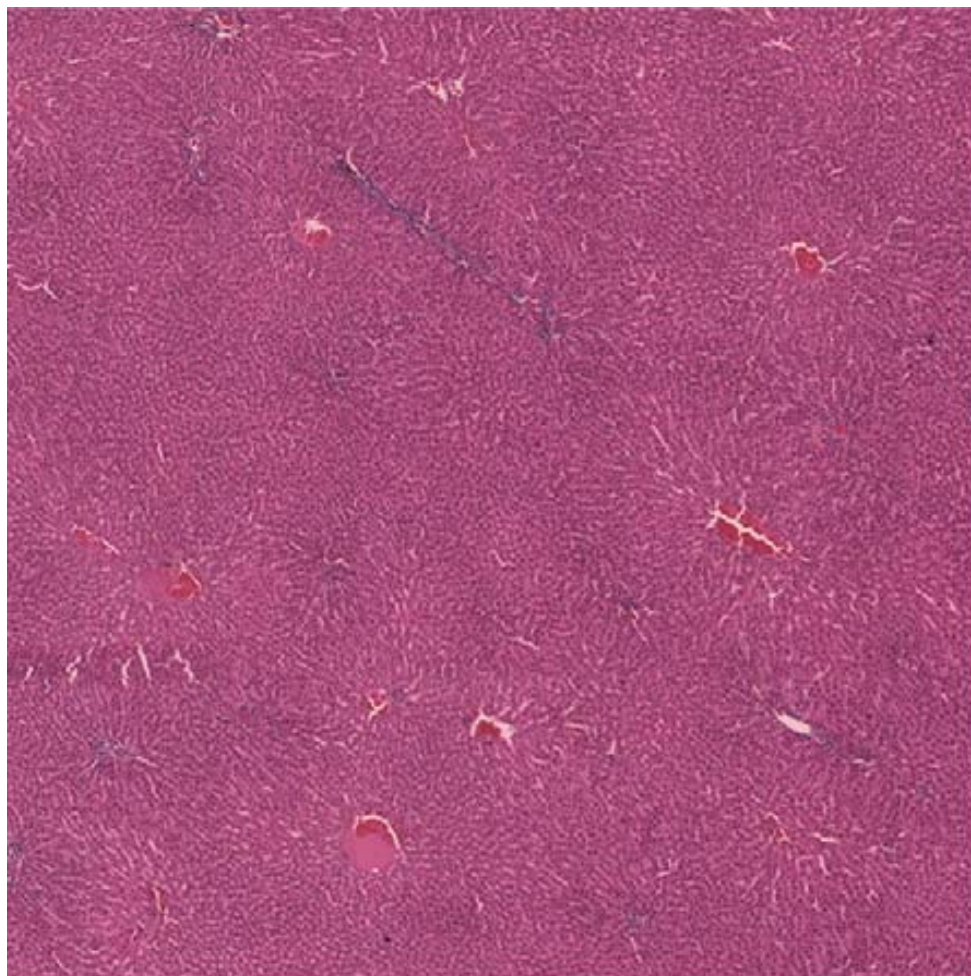
Figure 3.5: Representative T1W GRE images (A, B) and T1W (C, D), T2W (E, F), and PDW (G, H) TSE images acquired before (Pre-IRE) and immediately after (Post-IRE) the application of 2500V IRE pulses. These images were acquired along an orientation parallel to the IRE electrodes; bipolar electrode positions were depicted as signal voids. MRI-monitored IRE ablation zones were hypo-intense within T1W images and hyper-intense within both T2W and PDW images.



3.3.2 Histology

For rats euthanized immediately after IRE, H&E slides prepared from corresponding liver specimens showed eosinophilic cytoplasmic changes within the electroporated regions adjacent to the electrode positions; however, no other substantial histological alterations were observed at this early post-IRE time interval(Fig 3.6). For rats euthanized 24 hours after IRE procedures, histological slides demonstrated eosinophilic cytoplasm and central necrosis within IRE ablation zones with congestion in interstitial spaces and a well delineated boundary between untreated and ablated tissues (Fig 3.7).

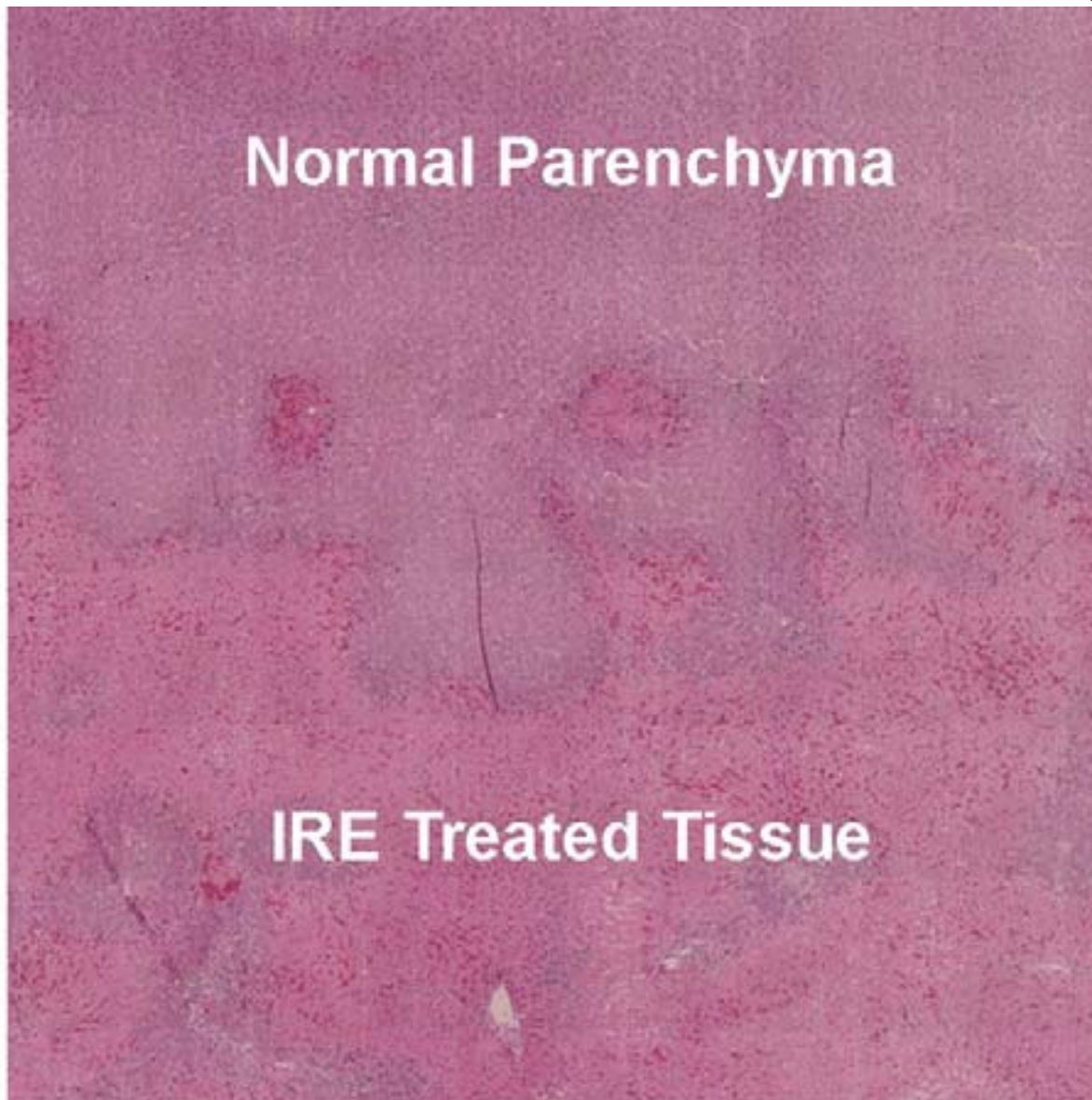
Figure 3.6: Representative hematoxylin-eosin (H&E) histology slide images for one rat that was sacrificed immediately after 2500V IRE procedures. A low magnification image (x2.5) with large FOV (A) and x25 magnification image (B) from inset (dashed box within A) each show no clear morphological changes but eosinophilic cytoplasmic changes within IRE ablation zones.



b.



a.



C.

Figure 3.7: A representative x25 magnification image from H&E slide for rat sacrificed 24 hours post-IRE shows a well-delineated boundary between untreated and ablated tissues with cellular necrosis within ablation zone.

3.3.3 Evaluation of Relationship between FEM-Predicted, MRI-Monitored, and Histology-Confirmed IRE Ablation Zones

FEM-predicted ablation zones (with anticipated 68.0V/mm lethal E -field potential) for electrode voltages of 1000V, 1500V, and 2500V, along with corresponding post-IRE T1W GRE images with 24hrs post-procedural H&E histology images for 3 different animals are shown in **Fig. 3.8**. As illustrated in **Fig. 3.8**, the MRI measurements and corresponding histological slides similarly depicted an increased ablation zone with increasing voltage and well-delineated boundaries between untreated and ablated tissues zones.

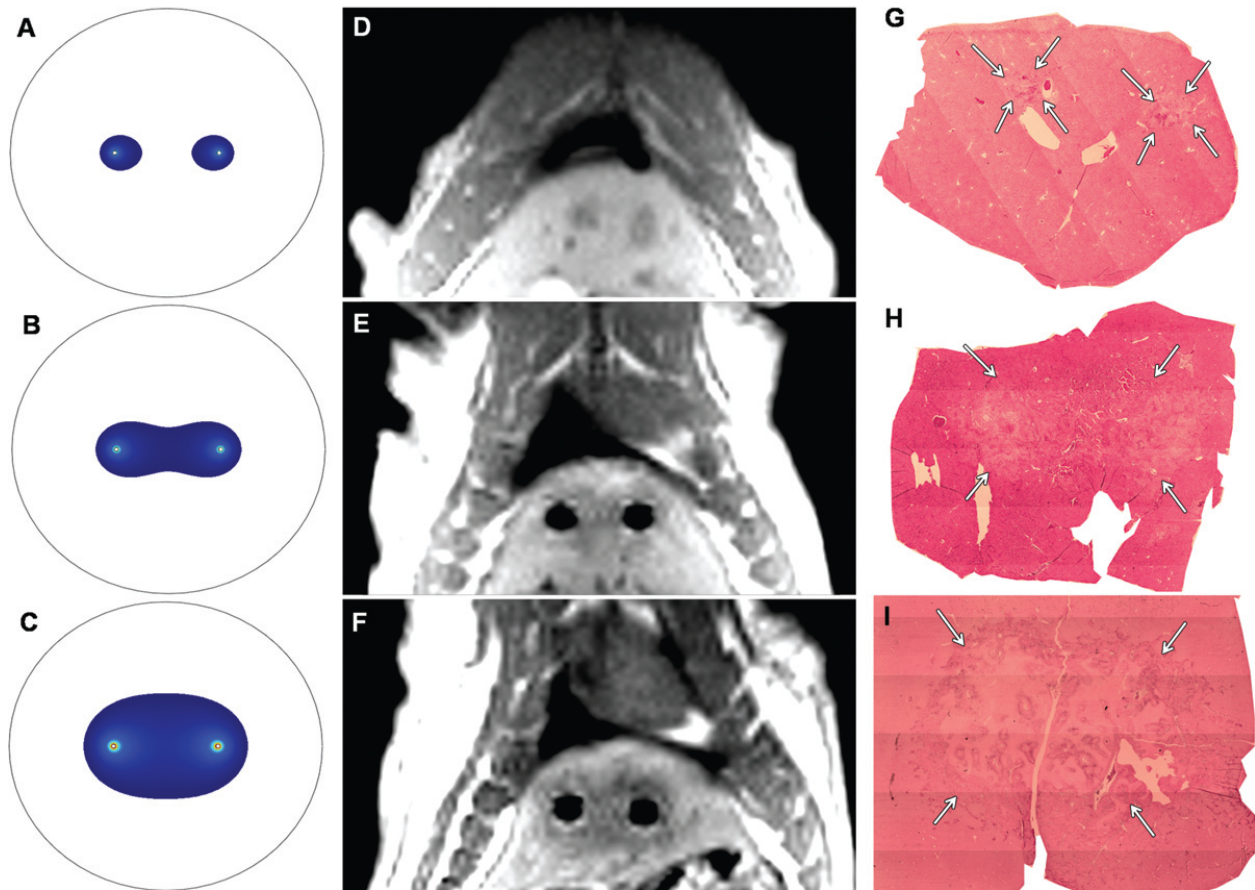


Figure 3.8: FEM-anticipated IRE ablation zones (A-C), post-IRE T1W GRE images (D-F) and corresponding H&E pathology slides from livers harvested 24hrs post-IRE (G-I) following IRE procedures with electrode voltages of 1000V, 1500V and 2500V (top, middle, and lower rows, respectively).

Analysis of variance indicated significant differences in MRI-based ablation zone measurements for the three different IRE electrode voltages groups ($p \leq 0.001$ for both T1W and T2W measurements). For T1W and T2W images, mean areas significantly increased with IRE voltage level as indicated by significant linear trends ($p < 0.001$). For both T1W and T2W measurements, mean IRE-impacted areas were progressively and significantly higher when compared in 1000V vs. 1500V groups, 1500V vs. 2500V groups, and 1000V vs. 2500V groups ($p < 0.001$ for each comparison, Table 3.1).

Table 3.1: MRI and Histological Measurements of IRE Ablation Zone

	FEM-	T1W MRI-	T2W MRI-	H&E Histology
IRE	Anticipated	Measured IRE	Measured IRE	Measured IRE
Voltage	IRE Ablation	Ablation Zone [†]	Ablation Zone [†]	Ablation Zone [†]
	Zone (mm ²)	(mm ²) Mean \pm SD	(mm ²) Mean \pm SD	(mm ²) Mean \pm SD
1000	26.51	30.46 \pm 7.56	29.46 \pm 7.95	22.54 \pm 8.25
1500	94.48	125.75 \pm 16.90	90.16 \pm 13.06	105.24 \pm 20.78
2500	183.54	186.61 \pm 17.91	183.26 \pm 18.50	226.94 \pm 62.85

[†]For T1W MRI, T2W MRI and H&E histology, $p < 0.001$ when comparing 1000V to 1500V, 1000V to 2500V, and 1500V to 2500V ablation zone measurements. SD: standard deviation

*Significance levels when comparing T1W and T2W MRI-measured IRE ablation zone at the same voltage level. $p = 0.272$ at 1000V, $p = 0.061$ at 1500V and $p = 0.120$ at 2500V.

FEM simulations predicted IRE ablation zones of 26.51mm², 94.48mm² and 183.54mm², respectively, for electrode voltages of 1000V, 1500V, and 2500V. Examination of the consistency between ablation zone measurements determined *in vivo* with MRI and the FEM-anticipated ablation zones indicated intra-class correlation coefficients of 0.96 ($p < 0.001$) for T1W measurements and 0.98 ($p < 0.001$) for T2W measurements (**Fig.3.9**). As shown in **Fig.3.10**, MRI measurements of the IRE ablation zones were also highly correlated with histology-confirmed ablation zone measurements, as indicated by Spearman correlation coefficients of $\rho = 0.90$, $p < 0.001$ for T1W and $\rho = 0.91$, $p < 0.001$ for T2W measurements. Within H&E slides, coagulative necrosis was clearly visualized in the ablation regions. The ablated zones were well demarcated from surrounding hepatic parenchyma. In the regions of IRE ablation, hepatocytes had markedly eosinophilic cytoplasm and sinusoids were congested.

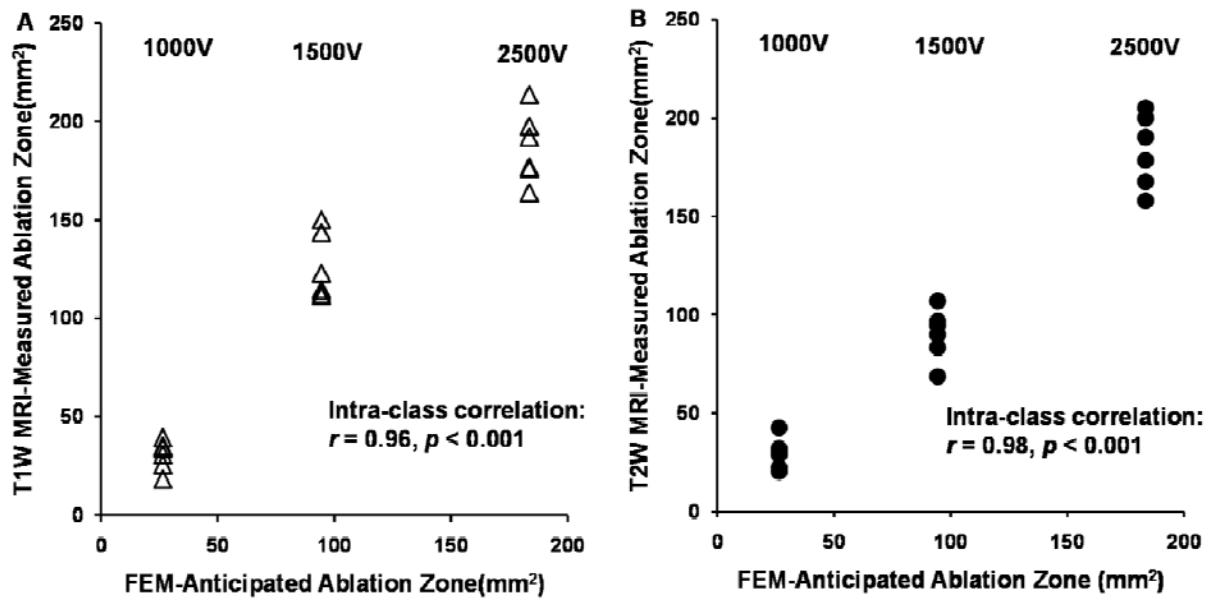


Figure 3.9: Scatterplots showing the relationship between intra-procedural MRI-based IRE ablation zone measurements and FEM-anticipated ablation measurements. Intra-procedural MRI-based IRE ablation zone measurements were highly consistent with FEM-anticipated ablation zones with intra-class correlation coefficients > 0.90 , $p < 0.001$ for both T1W (A) and T2W (B) measurements.

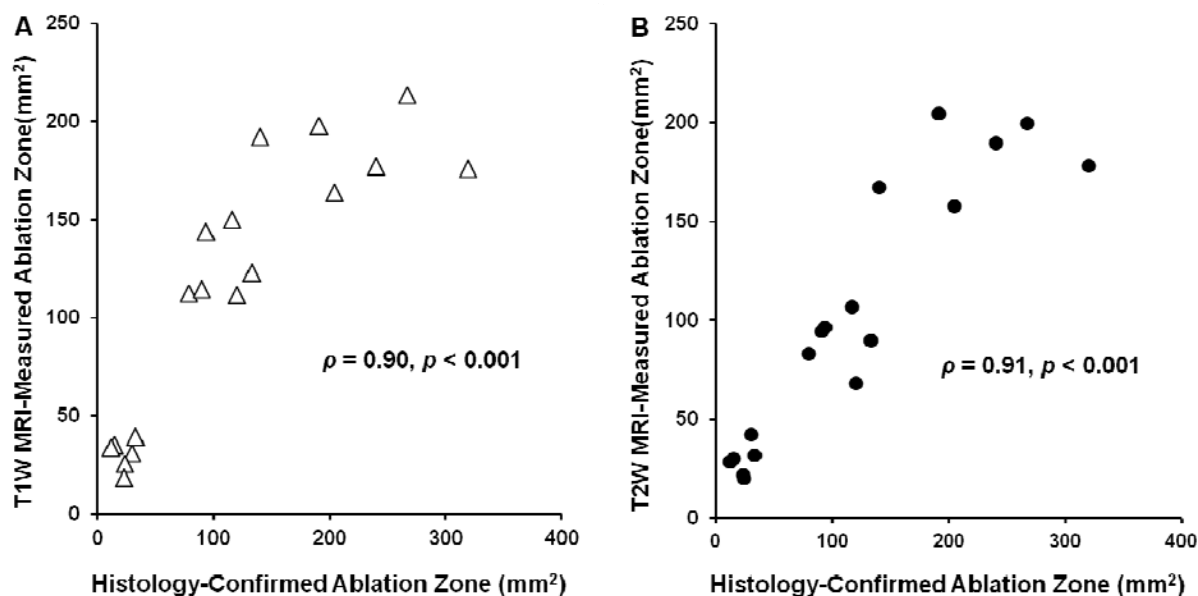


Figure 3.10: Scatterplots showing the relationship between intra-procedural MRI-based IRE ablation zone measurements and histology-confirmed IRE ablation zone measurements. Intra-procedural MRI-based IRE ablation zone measurements were highly correlated with with histology-confirmed measurements of the IRE ablation zone 24hrs post-therapy with Spearman correlation coefficient $\rho = 0.90$ for T1W (A) and $\rho = 0.91$ for T2W (B) measurements (both, $p < 0.001$).

3.4 DISCUSSION

IRE is a potentially highly effective tissue ablation technique. However, intra-procedural imaging guidance may be critical to optimize IRE approaches, particularly for visceral ablation procedures targeting liver tumors of primary or metastatic origin. Our initial feasibility studies successfully demonstrated the potential to use MRI measurements to monitor IRE zones in rat liver tissues. MRI-monitored ablation zones were immediately visible as hypo-intense regions within T1W images and hyper-intense regions within T2W and PDW images. MRI-monitored IRE ablation zones increased in size with increasing electrode voltage. MRI-based ablation zone measurements showed good consistency with FEM-anticipated ablation zones and were highly correlated with follow-up histology-based ablation zone measurements (Spearman $\rho > 0.90$ with $p < 0.001$ for both T1W and T2W measurements).

IRE electrodes were visualized as signal voids within each image with GRE sequences resulting in larger signal voids than those depicted using TSE sequences. The diameters of these signal voids were much larger than the diameter of the electrodes themselves. Due to the presence of these signal voids, the impact of the IRE ablation pulses could not be readily visualized immediately adjacent to the electrodes. However, in practice, we do not anticipate this limitation to be problematic for intra-procedural monitoring given that tissues immediately adjacent to the electrode should experience very high E -field potentials orders of magnitude greater than those produced in tissues located at increasing distances from the electrodes (31); we would anticipate that relatively independent of the applied electrode voltage used for a given IRE

procedure, tissues immediately adjacent to the electrode should be sufficiently treated.

However, the size of each electrode-induced signal void is dependent upon the material used to construct the electrodes (essentially the prime determinant is the magnetic susceptibility of the electrode relative to the adjacent tissues), main magnetic field strength, electrode orientation relative to the main field, pulse sequence used for visualization and associated sequence parameters. As would be expected, for this initial feasibility study and associated imaging parameters, the diameter of the electrode-induced signal voids were much larger within GRE images than within TSE images (roughly 3.5mm and 1.5mm in diameter, respectively). For translation to clinical practice, larger diameter electrodes will likely be required thus increasing the size of anticipated signal voids. Additional studies are clearly warranted to further investigate the size of the induced signal voids relative to ablation zone sizes, particularly for larger, clinically relevant IRE electrodes and electrodes constructed using different materials. Ultra-short echo-time sequences (21), gradient-echo slice excitation profile imaging techniques (22), and view-angle tilting methods (23) have previously been used to reduce the size of signal voids produced during the placement of percutaneous needles and/or ablation probes during MRI-guided biopsy and ablation procedures; these methods should each be similarly applicable in the setting of MRI-guided IRE.

While further studies are clearly necessary to fully investigate the contrast mechanisms that produce immediate IRE-induced PDW, T2W, and T1W signal changes, we speculate that these may be the result of local fluid accumulation due to transient permeabilization of blood vessels with subsequent fluid build-up after rapid extravasation

into the treated tissue zones. These IRE-induced signal alterations (hyper-intense zones within PDW and T2W images, hypo-intense zones within T1W images) were highly consistent with classic proton-density, T2 relaxation, and T1 relaxation increases typically observed during acute episodes of tissue edema (79-82). In a prior *in vivo* electro-permeabilized skeletal muscle study, the formation of edema was qualitatively confirmed by phase contrast photomicrographs of H&E (73). Our findings are consistent with previous gene-therapy electro-transfer studies (similar procedures to IRE involving the application of high voltage electrical pulses to permeabilize cell membranes) during which muscle tissue edema was visualized as hyper-intense regions within T2W images (70, 83).

MRI measurements of ablation zone sizes at 1500V were somewhat larger in T1W images compared to corresponding T2W images. The reason for this discrepancy is currently unclear. One possible source of error may have simply been mis-registration of slice positions between the separate T1W and T2W measurements during these free-breathing *in vivo* studies. Another possibility is that the T1W signal changes, at this particular applied voltage level, occurred both within the irreversibly electroporated central ablation zone as well as an outer surrounding region of reversibly electroporated tissue. Further studies are necessary to rigorously investigate the mechanism(s) that may have lead to these aforementioned differences.

Our study had several limitations. While histology measurements were highly correlated with intra-procedural MRI measurements of the IRE ablation zones, a

variable level of discrepancy between these measurements was clearly evident. However, these discrepancies were not entirely unexpected given the difficulties associated with correlating *in vivo* imaging results to histology measurements at delayed intervals post-therapy. Co-registration of these measurements was quite difficult given that the IRE electrodes (serving as our fiducial markers during the MRI studies) were removed and the surgical incision closed to survive each animal for 24hrs prior to necropsy. These delays between imaging and histology measurements were critically necessary given that IRE-induced tissue necrosis does not occur until roughly 12-24hrs post-therapy. Future pre-clinical correlation studies in the setting of IRE therapy may benefit from the use of either surgically-implanted, permanent fiducial markers to avoid such complications.

An additional limitation of this study was that IRE procedures were performed in normal liver parenchyma as opposed to hepatic tumor tissues. Future studies will be critical to confirm similar findings in hepatic tumor tissues and compare long-term IRE treatment outcomes to intra-procedural MRI measurements. Alternative functional imaging methods such as diffusion-weighted MRI (63) or dynamic contrast-enhanced MRI (84, 85) may also prove effective for *in vivo* quantification of the IRE ablation zones. However, due to the strong magnetic susceptibility differences between electrodes and surrounding tissues, conventional single-shot diffusion-weighted sequences may be ineffective and contrast-enhanced methods (due to requisite limits upon contrast dose) may be more effective for follow-up studies than for intra-procedural monitoring requiring repeated measurements. Additional functional and quantitative MRI studies

are clearly warranted to further investigate the potential for more accurate discrimination between treated and untreated IRE ablation zones.

4 MRI-BASED 3D FINITE ELEMENT MODELING FOR PREDICTION OF IRREVERSIBLE ELECTROPORATION ABLATION ZONES IN A RAT LIVER TUMOR MODEL

4.1 INTRODUCTION

Irreversible electroporation (IRE) (27) has recently been applied as a novel tissue ablation modality; IRE involves application of short-lived electrical fields across the cell membrane to permanently increase membrane permeability leading to cell death. 2D finite element methods (FEM) are used to model anticipated electrical field distributions but these typically assume homogeneous tissue conductivity (24); heterogeneity could lead to poor approximations of subsequent ablation volume. In this work, we developed a 3D FEM approach using pre-procedural MRI measurements to produce a patients-specific 3D surrogate-conductivity map for simulation of IRE ablation zones in a rat model of hepatocellular carcinoma (HCC). The purpose of this study was to prospectively test the hypothesis that pre-procedural MRI and 3D finite element methods (FEM) can be used to accurately predict IRE ablation zones.

4.2 MATERIALS AND METHODS

4.2.1 Tumor Cell Culture

The N1-S1 rat hepatoma cell line (CRL-1603, American Type Culture Collection, Manassas, Virginia) was propagated in Dulbecco's Modified Eagle's Medium (DMEM, ATCC, Manassas, Virginia) supplemented with 10% fetal bovine serum (Sigma-Aldrich)

90 µg/mL gentamicin. N1S1 cells were initially developed from carcinogenicity studies in Sprague–Dawley rats whose diet included 4-dimethylaaminoasobenzene (20). The Cells grew in suspension culture flasks at 37°C in a 95% air/5% CO₂ incubator. 5×10⁶ cells were injected into liver for each implantation in order to establish tumor liver. Before each implantation procedure, >90% cell viability was confirmed by trypan blue staining.

4.2.2 Animal Model

All experiments and animal procedures were approved by the institutional animal care and use committees of University of Illinois at Chicago and Northwestern University. 16 male Sprague-Dawley rats (Charles River, Wilmington, MA) weighing 300-350g were used for these experiments. After anesthesia, the left lateral lobe of rat liver was exposed and 5×10⁶ N1-S1 cells were injected visually beneath the hepatic capsule into this lobe. Following the implantation, tumor growth to desired pre-treatment size generally required about 7 to 10 days. The N1-S1 HCC cell line was used to grow one tumor in each rat; rats were divided into small (<8.50 mm, Group A) and large (> 8.50 mm, Group B) tumor size groups (8 rats/group). Prior to IRE and MRI procedures, rats were anesthetized with a high limb injection of Ketamine (75-100 mg/kg, Ketaset; Fort Dodge Animal Health, Fort Dodge, IA) and Xylazine (2-6 mg/kg, Isothesia; Abbott Laboratories, North Chicago, IL). Rats were restrained in supine position and the left lateral lobe of the liver exposed with midline incision. After anesthesia, rats were restrained in supine position and the liver exposed with midline incision. Two parallel platinum-iridium needle electrodes were inserted into the liver to straddle tumor centroid.

4.2.3 MRI Measurements

All experiments were performed using a 1.5T clinical MR scanner (Magnetom Espree, Siemens Medical Solutions) with a head coil. Electrodes remained positioned within the liver throughout the procedure but were disconnected from the function generator during the MRI scan. Prior to application of the IRE pulses, localization scans were performed to identify separate imaging planes perpendicular and parallel to the electrodes. Next, we acquired pre-IRE T2-weighted (T2W) turbo spin-echo (TSE) images with repetition time/echo time (TR/TE) = 3640/61ms, flip angle = 150° , slice thickness (TH) = 2mm, field of view (FOV) = $75 \times 150 \text{ mm}^2$, matrix = 96×192 , bandwidth = 205 Hz/pixel Images were acquired along orientations both parallel and perpendicular to the electrodes.

Table 4.1: MRI Parameters of T2W TSE

TR	3640 ms
TE	61ms
FA	150°
TH	2 mm
FOV	$75 \times 150 \text{ mm}^2$
Matrix	96×192
BW	205 Hz/pixel

4.2.4 IRE Procedures

After pre-IRE scan, rats were removed from the scanner bore but remained fixed in supine position within restrain apparatus (rats strapped to form-fitting back board). Electrodes were connected to IRE function generator (Electroporator ECM830; BTX Division of Harvard Apparatus, Holliston, MA). 2000V square wave pulses were applied to the 2 parallel electrodes with following protocol: total number of pulses = 8, duration of each pulse = 100 μ s, and interval between two pulses = 100 ms (same protocol for 2 groups).

4.2.5 Histology

After IRE procedure, rats were survived for 24 hours and then euthanized to harvest liver. Liver specimens were fixed in formalin and stained using hematoxylin and eosin (H&E). Livers were fixed in 10% buffered formaldehyde solution, sliced at 3mm intervals, and embedded in paraffin for histological examination. Liver sections were sliced in 4 μ m thick sections and stained using hematoxylin and eosin (H&E). Histological slides were digitized with an optical magnification image acquisition system (TissueGnostics, Vienna, Austria). ImageJ (NIH) was used to manually draw a region-of-interest (ROI) circumscribing areas of cellular necrosis within each image to measure the resulting total ablation zone and non-ablated tumor zone for each animal. The areas of these region-of-interest (mm²) were measured for comparison.

4.2.6 FEM Simulation

T2W images along the orientation parallel to the electrodes were manually segmented into normal liver and tumor region ROI, for each slice these ROI were a 2D structured matrix with MATLAB software (MathWorks, Natick, MA). Each 2D structured matrix was imported into COMSOL software (Comsol, Burlington, MA) with the slice stack combined to generate a 3D data volume via linear interpolation. Normal liver regions were assigned a conductivity value of 0.125 S/m whereas tumor tissues were assigned a value of 0.275 S/m (78). The electrical field distribution map was generated based on this model, electrode position (identified within the MRI image stack), and applied IRE pulse parameters. The threshold for IRE in liver was assumed to be 60.0 V/mm. We measured the total area of IRE ablation and non-ablated tumor zones within these FEM simulations at central axial slice through the tumor.

4.2.7 Statistical Analysis

Pearson correlation coefficients were calculated to examine the relationship between FEM-simulated and histology-confirmed ablation zone measurements and a t-test was performed to compare the difference between untreated remnant tumor zone between large and small tumor treatment groups ($p < 0.05$ considered statistically significant).

4.3 RESULTS

FEM-simulated (Fig.4.1E) and histology-confirmed (Fig.4.1F) total ablation zones tended to cover the entire tumor region for Group A. However, ablation zones (Fig.4.2E

and Fig.4.2F) tended to cover only a portion of the tumor for Group B rats. FEM-simulated total ablation zones were well correlated to histology-confirmed total ablation zones ($r=0.817$, $p<0.001$); the size of FEM-simulated untreated tumor zones was also well correlated with histology-confirmed viable remnant tumor zones ($r=0.781$, $p<0.001$). Untreated remnant tumor zones for Group A were significantly smaller than those in Group B ($p=0.007$) (Fig.4.3).

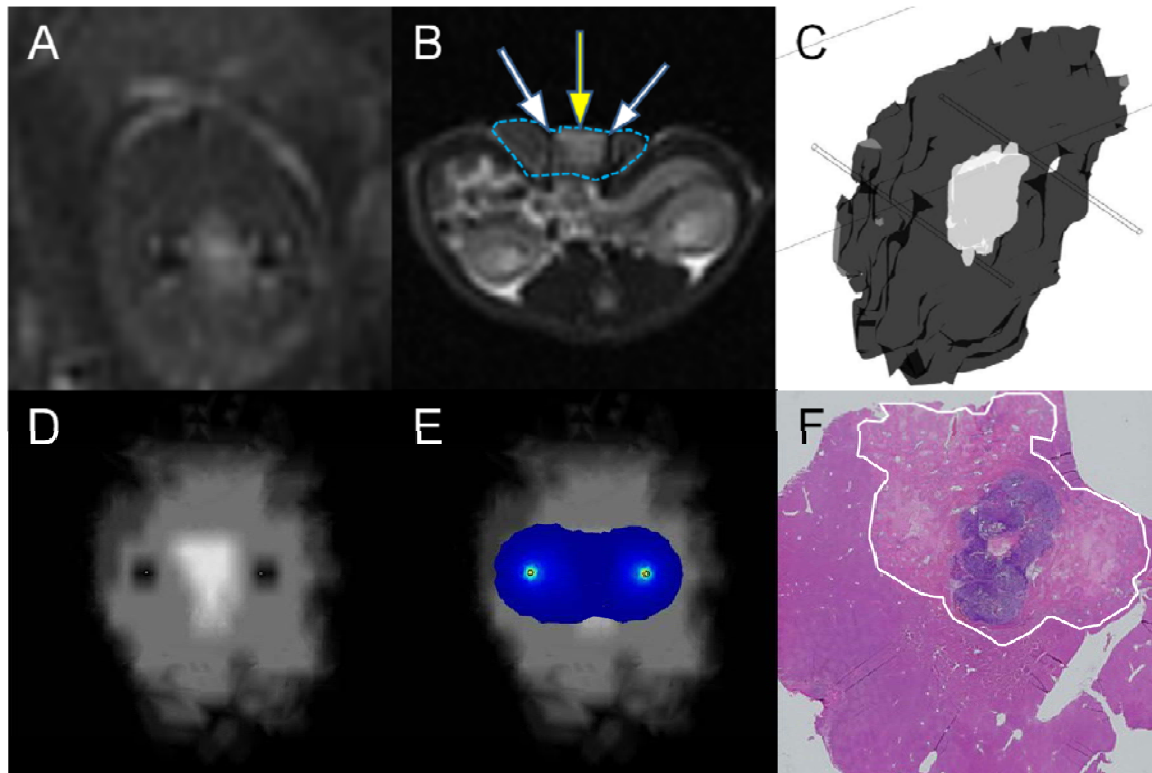


Figure 4.1: Representative images for Group A (left). T2W images (A and B, blue dashed circle for liver, white arrows for electrodes and yellow arrow for tumor), reconstructed 3D liver and tumor(C), axial view of 3D model (D), FEM simulated ablation zone (E, blue region) and histology-confirmed ablation zone (F, white circle).

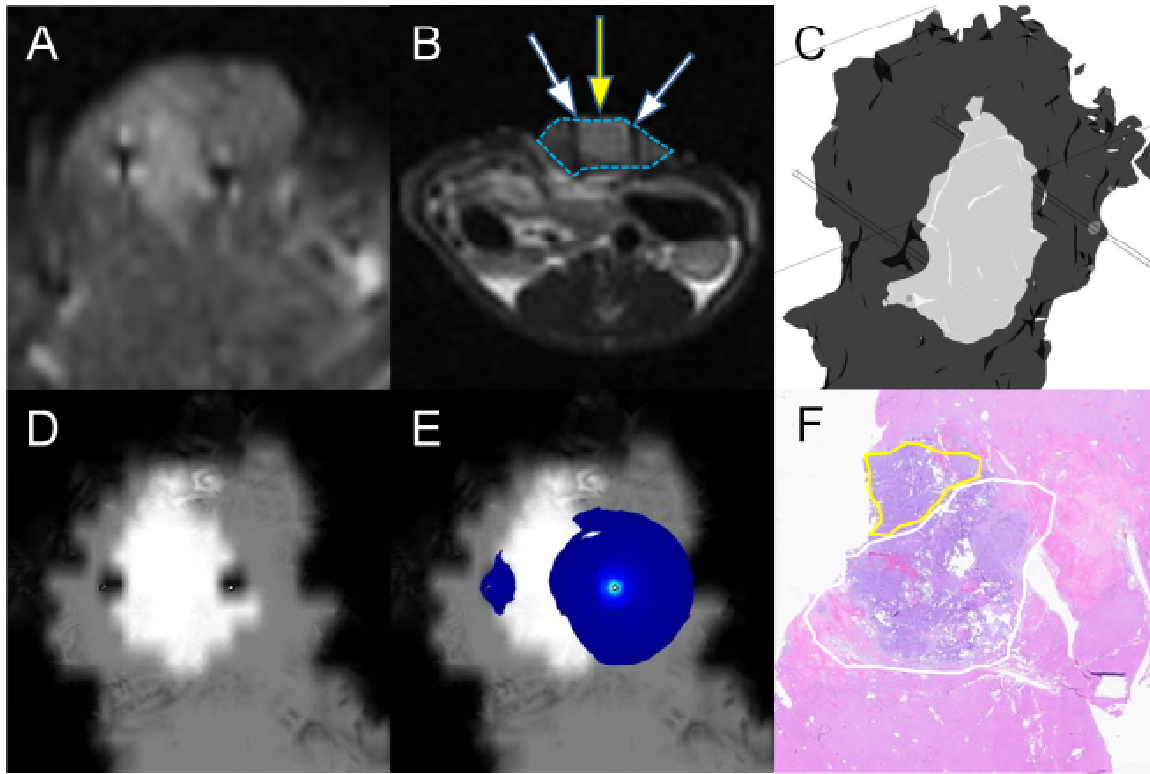


Figure 4.2: Representative images for Group B. (above) T2W images (A and B, blue dashed circle for liver, white arrows for electrodes and yellow arrow for tumor), reconstructed 3D liver and tumor (C), axial view of 3D FEM model (D), simulated ablation zone (E, blue region) and histology-confirmed ablation zone (F, white circle). Yellow circle indicated untreated tumor growing into surrounding normal liver.

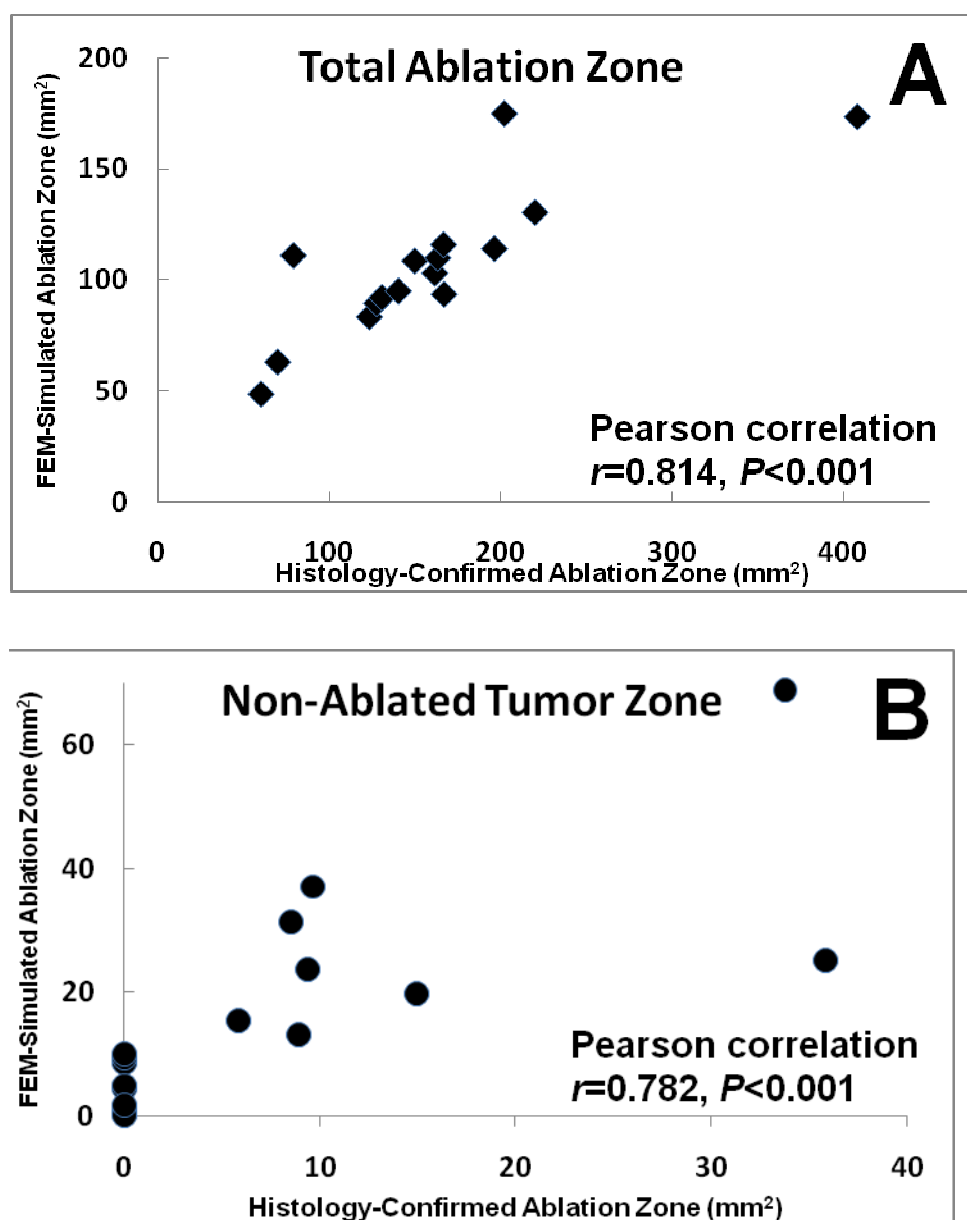


Figure 4.3: Scatterplots show the relationship between FEM-simulated IRE ablation zone and histology-confirmed IRE ablation zones.

4.4 DISCUSSION

IRE is an effective tumor ablation modality. Pre-procedural planning may be important to optimize IRE procedures. This study developed a MRI-based pre-procedural 3D FEM simulation method to predict IRE ablation zone. Pre-IRE T2-weighted MRI was used to create a 3D virtual liver model which is based on the actual tumor size and shape. FEM-simulated ablation zones were highly correlated with histology-confirmed ablation zone measurements (Pearson correlation coefficient $r=0.814$ with $p < 0.001$).

IRE electrodes were visualized as signal voids within each image within T2W images. The diameters of these signal voids were similar with the electrodes themselves. In practice, we do not anticipate this susceptibility artifacts to be problematic for pre-procedural imaging the liver given that tissues immediately adjacent to the electrode should experience very high E -field potentials orders of magnitude greater than those produced in tissues located at increasing distances from the electrodes (31); we would anticipate that relatively independent of the applied electrode voltage used for a given IRE procedure, tissues immediately adjacent to the electrode should be sufficiently treated. Additionally, IRE electrodes were also modeled in our simulation methods. In future clinical translation of this pre-procedure simulation approach, patient can be scanned without IRE electrodes and clinicians can manipulate the virtual electrodes to look for optimal electrode positions. The simulation can be performed multiple times until find optimal treatment.

In this study, the tumor size for each animal is larger enough to exceed the liver lobe thickness. The liver lobe containing tumor will be sliced along the coronal direction, which is going through the center of tumor. This histology preparation methodology was performed in all the animals for the H&E staining. Correspondingly, for this pre-procedural FEM simulation, the center slice position will be used to measure the area of the FEM-simulation ablation zone. While histology measurements were highly correlated with FEM-simulated measurements of the IRE ablation zones, different ablation patterns between FEM-simulated ablation zones and histology-confirmed ablation zones were also noted. However, these discrepancies were not entirely unexpected because the FEM simulation method is highly depend on tissue conductivity, which is dynamically changing during the delivery of electroporation pulses. Co-registration of these measurements was quite difficult given that the IRE electrodes (serving as our fiducial markers during the MRI studies) were removed and the surgical incision closed to survive each animal for 24hrs prior to necropsy. These delays between imaging and histology measurements were critically necessary given that IRE-induced tissue necrosis does not occur until roughly 12-24hrs post-therapy.

MRI and 3D FEM can be used to predict IRE ablation zones. These methods should permit pre-procedural, patient-specific optimization of IRE parameters (voltage and electrode positions) prior to IRE to ensure complete treatment of targeted lesions.

5 MULTI-MODALITY IMAGING TO ASSESS IMMEDIATE RESPONSE TO IRREVERSIBLE ELECTROPORATION IN A RAT LIVER TUMOR MODEL

5.1 INTRODUCTION

Irreversible electroporation (IRE) has been widely studied as a novel tissue ablation modality (27, 86). With IRE, permanent nano-scale pores are created using a strong short-lived electrical field across the cell membrane, which leads to a loss of homeostasis and eventual cell death(26). The electrical field is established by delivering multiple micro to millisecond electrical pulses(67). Compared to conventional thermal ablation approaches such as radiofrequency (41, 87), IRE avoids the heat sink effect when the target lesion is adjacent to a blood vessel(29), therefore, is able to effectively ablate tissues adjacent to the blood vessels (30). Additionally, IRE ablation times are very short and take only seconds to minutes. IRE ablation zones can also be pre-procedurally simulated by finite element method (26, 31). These advantages make IRE well suited for solid organs tumors, like hepatocellular carcinoma (HCC), the fifth most common neoplasm in the world(88). In the preclinical setting, IRE has been shown to be effective for targeted ablation of liver tumors in the N1-S1 rat model (89) and in rabbit VX2 liver tumors, where IRE resulted in complete ablation of the tumor (90).

Imaging approaches are playing a crucial role in all aspects of ablation procedures including locating the target lesions (91-93), intra-procedural monitoring the therapy(94-96) and evaluating the efficacy of the treatment (97-99). Ultrasonography (US) was first

used in ablation of normal liver in swine (27, 86) and due to its ease of use and availability, it is now routinely used during ablation procedures in the clinical setting . Both unenhanced and contrast-enhanced computed tomography (CT) have been used for evaluating IRE ablation (100, 101). Magnetic resonance (MR) imaging has also been shown to be useful at assessing the immediate response (102, 103) after IRE and found to have a strong correlation with histology (103, 104).

However, the image characteristics for these conventional imaging techniques have not been well studied, especially in tumor ablation. The echogenicity changes seen with US in normal liver ablation has been reported(105); however, no work has been done with tumor ablation. While CT and MR imaging have been used to characterize tumors 24 hours after IRE (89, 90), there is very little data evaluating the immediate imaging monitoring and the measurements in Hounsfield units (HU) and signal to noise ratio (SNR).

In this study, we performed IRE procedures in both normal liver tissue and hepatic tumors. The purpose of this study was to compare induced changes within US, CT and MR images shortly after irreversible electroporation (IRE) ablation of both normal liver parenchyma and hepatic tumors.

5.2 MATERIALS AND METHODS

5.2.1 Experimental Overview

We performed *in vivo* intra-hepatic IRE procedures in both normal liver and hepatic tumors in rat models using a single electrode voltage level. Individual imaging modalities (US, CT and MR) were performed immediately prior to and immediately after application of the IRE pulses. The rats were divided into 8 groups (6 rats/group): US was performed in 2 groups (US_N: normal tissue ablation and US_T: tumor ablation); CT was performed in 3 groups (CT_N, CT_T, CT_C: control tumor without ablation), and MR was performed for 3 groups (MR_N, MR_T, MR_L: hepatic vessels ligated prior to IRE). For animals in Group US_N, US_T, MR_N and MR_T, each underwent IRE procedures and then survived for 24hrs post-procedure to allow for definitive formation of IRE-induced necrotic tissue regions (27, 73). For rats in Groups CT_N and CT_T, they were euthanized 30 minutes after IRE for follow-up CT. (Due to technical considerations, imaging of live rats was not possible). CT was also performed in Group CT_C rats without IRE. Rats in Group MR_L underwent pre- and post-IRE MR imaging with IRE immediately after portal vein and hepatic artery ligation to investigate perfusion impact upon IRE-induced signal changes; they were euthanized immediately after post-IRE imaging.

5.2.2 Tumor Cell Line and Culture

The N1-S1 rat hepatoma cell line (CRL-1603, American Type Culture Collection (ATCC), Manassas, Virginia) was cultured in Dulbecco's Modified Eagle's Medium (DMEM, ATCC, Manassas, Virginia) supplemented with 10% fetal bovine serum (Sigma-Aldrich) 90 µg/mL gentamicin. The Cells grew in suspension culture flasks at

37°C in a 95% air/5% CO₂ incubator. 5×10^6 cells were cultured for each implantation in order to establish tumor liver. Before each implantation procedure, >90% cell viability was confirmed by trypan blue staining.

5.2.3 Animal Model

All experiments were approved by the institutional animal care and use committees of University of Illinois at Chicago and Northwestern University. 48 male Sprague-Dawley rats (Charles River, Wilmington, MA) weighing 300-350g were used for these experiments. Half of the animals (24 of the 48 total) they were divided among 4 groups: US_T, CT_T, CT_C and MR_T. 2×10^6 N1-S1 cells were implanted into the left lateral lobe of rat liver after median laparotomy was performed in order expose the liver. Following the implantation, the tumors grew for approximately 7 to 10 days in order to allow the tumors to grow to the desired pre-treatment size. Prior to IRE and imaging procedures, the rats were anesthetized using isoflurane 2-4%/O₂ 1-2L and maintained with a face mask (1-2%) during surgery and imaging.

5.2.4 IRE Procedures

After pre-IRE scans were performed, the rats were removed from the scanner and maintained in the supine position. The left lateral lobe of the liver was exposed after a median laparotomy was performed. For normal hepatic parenchyma (Group US_N, CT_N, MR_N and MR_L) ablation, two parallel needle electrodes with 1 cm spacing were inserted into the center of the left lateral hepatic lobe. For tumor ablation (Group US_T, CT_T and MR_T), the N1-S1 tumors within the left hepatic lobes were visually located and digitally

palpated between thumb and forefinger to approximate the configuration of the tumor mass; following that, the needle electrodes were positioned in the way that the needles were aligned along the axis of the largest tumor dimension. 1 cm electrode separation was maintained, as the needles had previously been secured in a 15-mm-thick plastic spacing block. After needle placement, the electrodes were connected to IRE generator (Electroporator ECM830; BTX Division of Harvard Apparatus, Holliston, MA). For IRE procedures, 2500V square wave pulses were applied to the 2 parallel electrodes with following protocol: total number of pulses = 8, duration of each pulse = 100 μ s, and interval between two pulses = 100 ms. Immediately after the application of the IRE pulses, electrodes were disconnected and post-IRE imaging was performed.

5.2.5 Multi-Modality Imaging

5.2.5.1 US

The left lateral hepatic lobe was exposed with a median laparotomy. For all US, imaging was performed using a 12 MHz transducer ultrasound probe (M7, MindRay, Shenzhen, China) on the exposed liver with an acoustic window created with ultrasound gel. For Group US_N, ultrasound was performed of the normal hepatic parenchyma and for Group US_T, ultrasound was performed on the tumor. 30 minutes after the IRE procedures, the same scans were performed again to acquire post-IRE images (Focal zone depth, gain and tissue harmonics applications were optimized by the operator on a case-by-case basis for the initial images and the parameters were not changed on the post-IRE images).

5.2.5.2 CT

Computed tomography (CT) examinations were performed in Groups CT_N, CT_T and CT_C on a 64 helical clinical system (Sensation; Siemens Healthcare USA, Malvern, Pa). For rats in Groups CT_N and CT_T, they were euthanized 30 minutes after IRE for follow-up CT; CT was performed in Group CT_C rats without IRE. The following CT parameters were used: 120 kVp, 250 mA, 1mm for slice thickness.

5.2.5.3 MR Imaging

All MR imaging was performed in Groups MR_N, MR_T and MR_L using a 7 Tesla animal scanner (ClinScan, Bruker BioSpin, Ettlingen, Germany) with a two-channel volume coil with an inner diameter of 8 cm for signal reception. Pre- and post-IRE MR imaging were performed: T1-weighted (T1W) gradient recalled echo (GRE) and T2-weighted (T2W) turbo spin-echo (TSE) images were acquired for all 3 groups. The general parameters for all sequences are slice thickness (TH) = 1mm, field of view (FOV) = 64×128 mm², matrix = 96×192, bandwidth = 500 Hz/pixel. T1W repetition time/echo time (TR/TE) = 200/2.68ms, flip angle (FA) = 90°, number of averages (NA) = 6. T2W TR/TE ≈ 2634/44.1ms, FA=180, NA = 3. In order to reduce motion artifacts, an MR-compatible Small Animal Monitoring and Gating System (SA Instruments, Inc, Stony Brook, NY) was used during T2W TSE imaging by attaching a small pneumatic pillow to the animal abdomen to measure the respiratory rate.

Table 5.1: MRI Parameters of T1W GRE and T2W TSE

	T1W	T2W
TR (ms)	200	2634
TE (ms)	2.68	44.1
FA (°)	90	180
NA	6	3
TH (mm)	1	
FOV (mm ²)	64×128	
Matrix	96×192	
BW (Hz/pixel)	500	

5.2.6 Histological Evaluation

The animals in Groups CT_N, CT_T and MR_L were euthanized approximately 30 minutes after post-IRE imaging scans. The animals in Group CT_C were euthanized without IRE. The animals in Groups US_N, US_T, MR_N and MR_T were euthanized 24 hours after electroporation. These rats were euthanized and livers harvested. The livers were fixed in 10% buffered formaldehyde solution, sliced at 3 mm intervals, and embedded in paraffin for histological examination. Liver sections were sliced in 4 µm thick sections and stained using hematoxylin and eosin (H&E). Histological slides were digitized with an optical magnification image acquisition system (TissueGnostics, Vienna, Austria) for the entire field of view with a low magnification (10x); then H&E slides were scanned by another system (Zeiss Axioskop, Jena, Germany) for regional details with a high magnification (40x). Additionally, normal liver tissue and ablated normal tissue (both immediately sacrificed and 1day sacrificed), control tumor and ablated tumor (both immediately sacrificed and 1day sacrificed), were prepared for transmission electron microscopy (TEM). The tissue samples were sliced into 1 mm cubes and placed in Karnovsky's fixative (0.1 M phosphate buffered solution containing 5% glutaraldehyde with a pH between 7.2 and 7.4) for 2 weeks to preserve structures. The samples were stained with osmium tetroxide (OsO₄), dehydrated and then embedded in resin containing 36% ERL 4221, 12% diglycidyl ether of polypropyleneglycol (DER 736), 51% nonenyl succinic anhydride (NSA), and ~1% dimethylaminoethanol (DMAE) by mass. Samples were then sectioned with an ultra-microtome to a thickness of 70 nm and imaged with transmission electronic microscopy (TEM; FEI Tecnai Spirit G2) operating at 120 kV.

5.2.7 Data Analysis

The ImageJ software package (NIH) was used to analyze all of the images. The pre- and post-IRE US images were individually reviewed by 2 radiologists to determine the echogenicity prior to and after IRE by following a 4 scale grade system: 0 for no change, 1 for slight change, 2 for clear change and 3 for dramatic change (only the tumors' echogenicity change was considered for Group US_T). The discordant images will be reviewed by a third radiologist. The average grade of echogenicity change for normal liver ablation and tumor ablation will then be calculated. CT images were initially reviewed with a window level and window width of 50 and 150 Hounsfield units (HU). To improve the subjective conspicuity of the findings, the observer was free to adjust the window width and window level at will. Regions of interest (ROIs) were drawn to measure HU in different regions: normal liver post-IRE and adjacent untreated normal liver for Group CT_N, on tumors post-IRE for Groups CT_T and control tumor for Group CT_C. Within pre- and post-IRE T1W and T2W MR images, signal to noise ratio (SNR) was measured in both normal (MR_N) and tumor tissues (MR_T).

5.2.8 Statistical Analysis

Independent t-tests were used to compare the HU measurements of pre- and post-IRE CTs. Paired t-tests were performed to compare the SNR measurements of pre- and post-IRE T1W and T2W images. These analyses were implemented with the SPSS Version 17 software package (Chicago, IL) with *p*-values less than 0.05 considered statistically significant.

5.3 RESULTS

5.3.1 Multi-Modality Imaging

US Findings

For normal liver ablation (US_N), pre- and post-IRE US were acquired (**Fig.1A** and **Fig.1B**). On post-IRE US, ablated tissue appeared as a hypo-echoic region adjacent to the IRE probes and in most cases, a hyper-echoic rim was also seen (when compared to the normal surrounding hepatic parenchyma). For tumor ablation (US_T), the tumor appeared heteroechoic (hyper-echoic peripherally and iso-echoic centrally on pre-IRE US (**Fig.2A** and **Fig.2B**)). On post-IRE US, all tissues adjacent to the IRE-probe (both normal hepatic parenchyma and tumor) became more hypo-echoic and a hyper-echoic rim developed along the periphery of the ablation zone. The site of the electrodes were also noted and appeared a linear focus of hyperechogenicity, which corresponded to air introduced during initial probe placement.

CT

On post-IRE CT, ablated normal tissues appeared as hypo-attenuating foci compared to surrounding un-ablated tissues (**Fig.1C** and **Fig.1D**). The control tumor (CT_C) appeared as hypo-attenuating foci on CT (**Fig.2C**); following tumor IRE, a large hypo-attenuating focus appeared and the tumor margin could no longer be clearly visualized (**Fig.2D**).

MRI Measurements

Representative images from normal liver prior to and immediately after application 2500V IRE pulses were shown in **Fig.1**. IRE impacted tissues were clearly demarcated

from surrounding normal hepatic parenchyma; electroporated tissues were hypo-intense on T1W images (**Fig.1F**) but consistently hyper-intense on T2W images (**Fig.1H**).

Representative images from tumor ablation pre- and post-IRE are shown in **Fig.2**. Pre-IRE tumors appear hypo-intense on T1W images (**Fig.2E**) and hyper-intense on T2W images (**Fig.2G**); after IRE, a large hypo-intense area appeared as the ablation region on T1W images (**Fig.2F**) and a hyper-intense region of ablated normal tissues appeared surrounding the central hyper-intense tumor in T2W images (**Fig.2H**).

Figure 5.1: Representative multi-modality images for pre-IRE and post-IRE in normal hepatic parenchyma. On 30 min Post-IRE US(B), a hypoechoic region foci was noted in the liver parenchyma (white cross); Red arrow indicated the probe position (hyperechogenicity related to introduction of air into the liver with probe placement). On post-IRE CT(D), a hypoattenuate region appeared as the ablation zone. The ablation zone was visualized as hypointensity within T1W (F) and hyperintensity within T2W MRI(H).

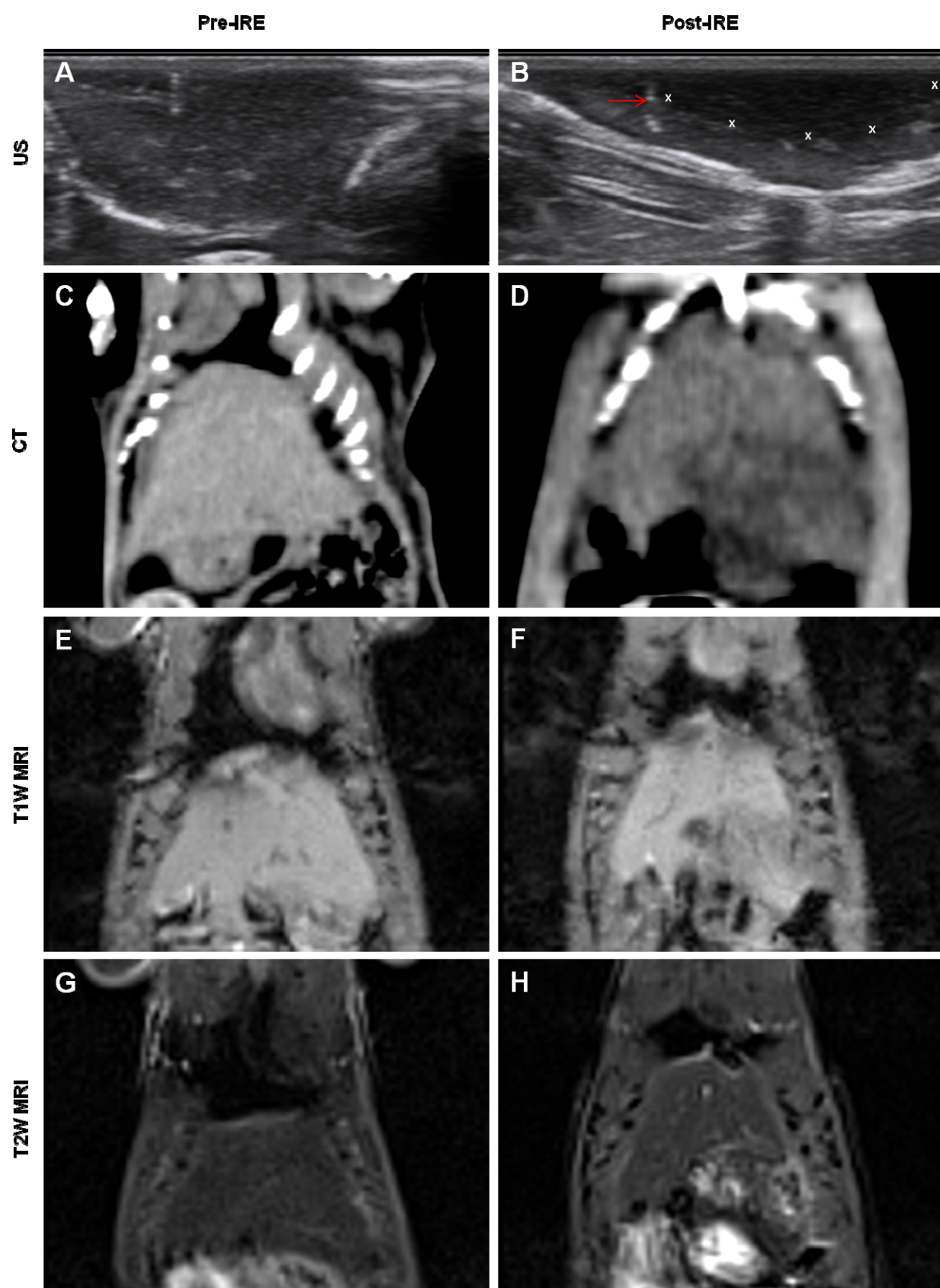
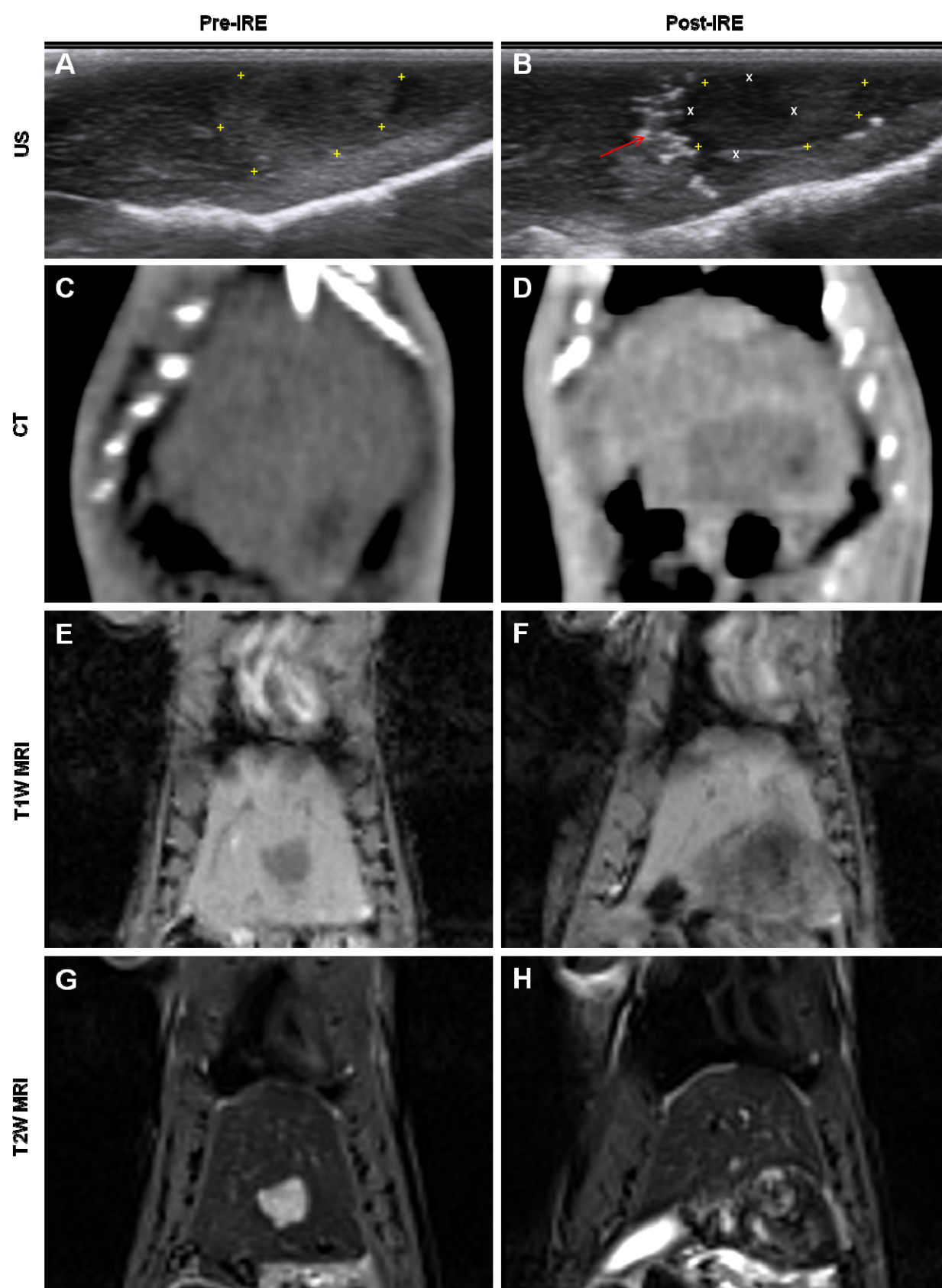


Figure 5.2: Representative multi-modality images for pre-IRE and post-IRE in tumors. Within Pre-IRE US (A), the tumor (yellow plus) appeared as hyperechoic peripherally and isoechoic centrally (when compared to normal hepatic parenchyma); Within Post-IRE US (B), both normal and tumor tissues adjacent to the IRE probe became more hypo-echoic. Red arrow indicated the probe position. The ablation zone appeared as hypoattenuating within post-IRE CT (D) where the tumor boundary could no longer be noted. A hypointense ablation zone appeared within post-IRE T1W (F). A hyperintense region of ablated normal tissues appeared surrounding the central hyperintense tumor within T2W (H).



5.3.2 Hepatic Ligation

For the animal in Group MR_L that underwent portal vein and hepatic artery ligation prior to MRI-monitored IRE procedures, no post-IRE signal changes were observed; representative images for a single animal are shown in **Fig. 5.3**.

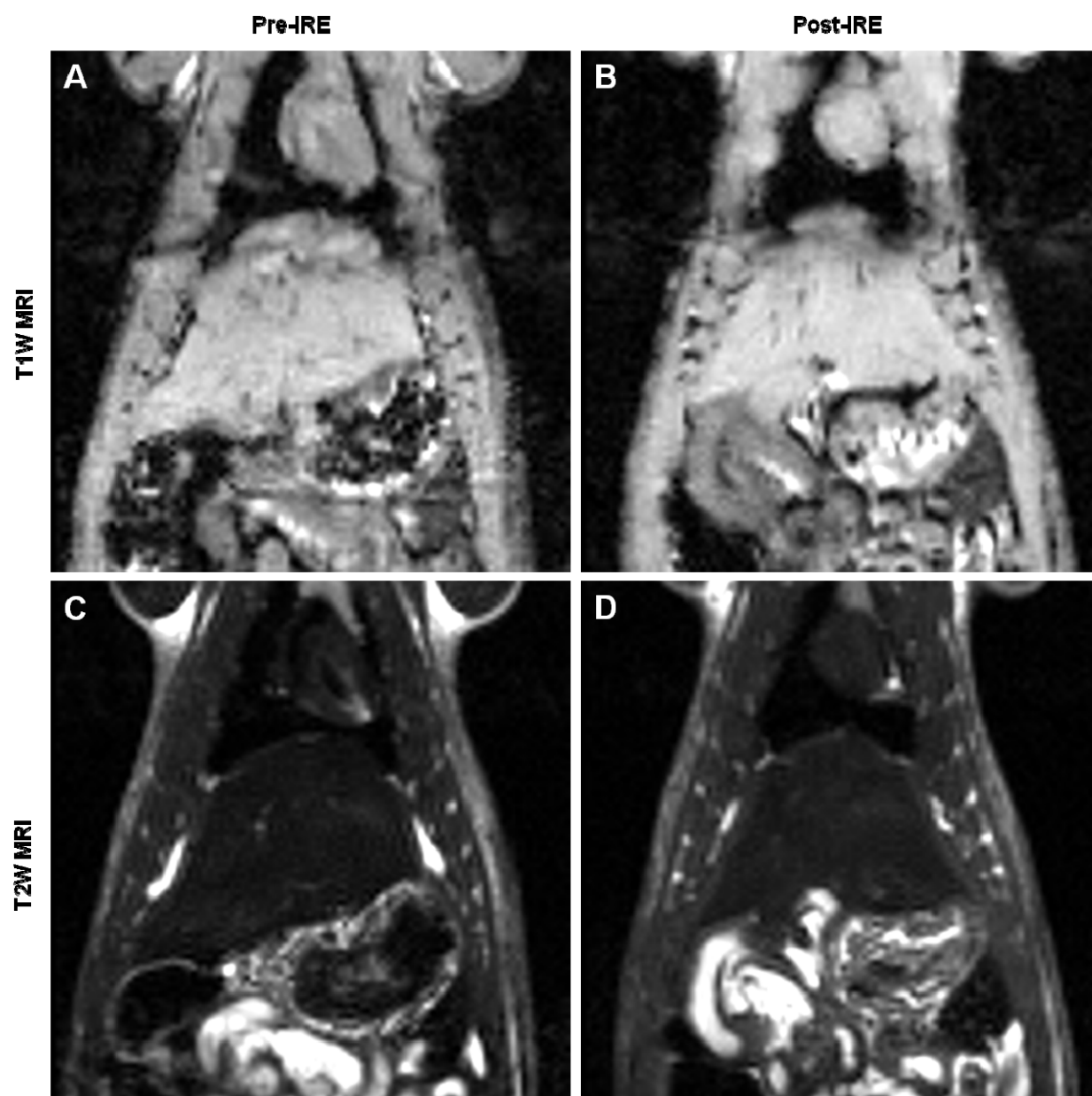


Figure 5.3: T1W GRE images (A,B) and T2W (C,D) TSE images acquired before (Pre-IRE) and immediately after (Post-IRE) the application of 2500V IRE pulses in rat with ligated port vein and hepatic artery. Notice the conspicuous lack of post-IRE T1W and T2W signal alterations compared to the post-IRE signal changes clearly apparent within those images presented in **Fig.5.1**.

5.3.3 Histology

Within the H&E staining of normal hepatic parenchyma ablation, the ablated zone approximately 30 minutes after IRE became slightly pale compared to non-ablated zone, indicating degeneration of eosinophilic structures like cytoplasm and extracellular spaces; the nuclei maintained their structures. At 24 hours, the electroporated regions appeared clear pale compared to peripheral non-ablated normal liver tissues; some of nuclei decreased in size indicating the presence of coagulation necrosis; an influx of red blood cells was seen in the extracellular spaces. Within the H&E stains of the ablated tumor, the ablation zones covered the entire tumor within both on the immediate and 24 hour post IRE H&E staining; the tumor cells were more loosely arranged compared to the non-ablated tumor cells. Some nuclei agglutinations was seen at 30 minutes; nuclear cytoplasm ratio increased 24 hours after IRE.

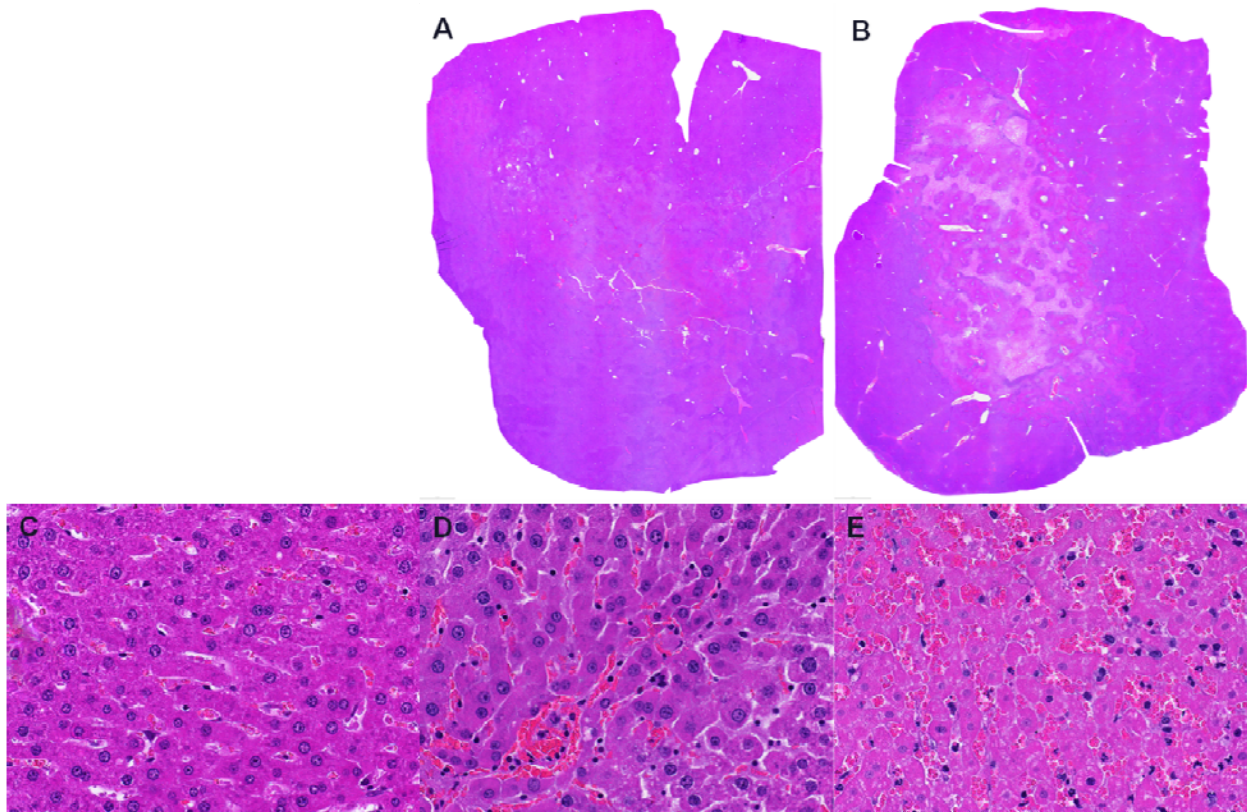


Figure 5.4: Representative H-E–stained histology slides for normal liver ablation in rats sacrificed 30minutes (A) and 24 hours after IRE procedures (B). The 24-hour staining (B) showed a more clear ablation zone than immediate one (A). The morphology of the cell nuclear immediately after IRE (D) showed no clear change compared to unablated tissues (C), but small amount of red blood cells appeared in some extracellular spaces. After 24 hours (E), red blood cells were filled in most extracellular spaces and sinusoidal space and nuclear lost their normal morphology by becoming shrunken, indicating cell necrosis.

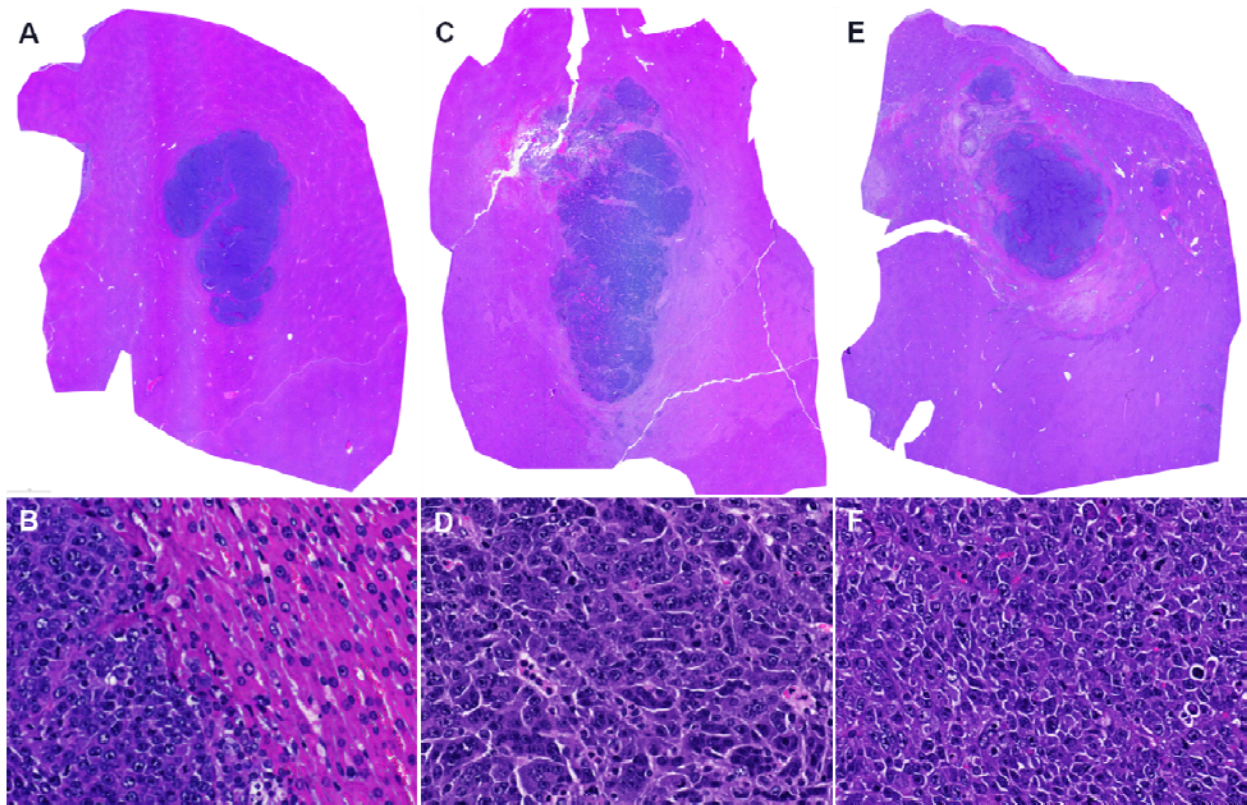


Figure 5.5: Representative H-E–stained histology slides for tumor ablation in rats those were control (A,B), sacrificed 30minutes (C,D) and 24 hours after IRE procedures (E,F). The tumor cells arranged loosely within both 30 minutes (D) and 24 hours(F) compared to control tumor cells (B). Some nucleus agglutinations can be seen at 30 minutes; nuclear cytoplasm ratio increases 24 hours after IRE.

Evaluation of the TEM images demonstrated intact cellular membranes in those tissues that were harvested immediately after IRE. These tissues could no longer be differentiated from the non-ablated tumor cells. However, small pores appeared in the nuclear membrane, while some vacuoles were present, most organelles maintained their structures indicating the organelles had begun to degenerate. At 24 hour after IRE, small pores could still be seen along the nuclear membrane and the basal layer was thinner compared to the tissue that from the samples that were obtained immediately after IRE, which indicated the irreversible electroporation had been performed. The electron density of the nucleus decreased compared to that immediately after IRE indicating the degeneration/migration of the chromatin.

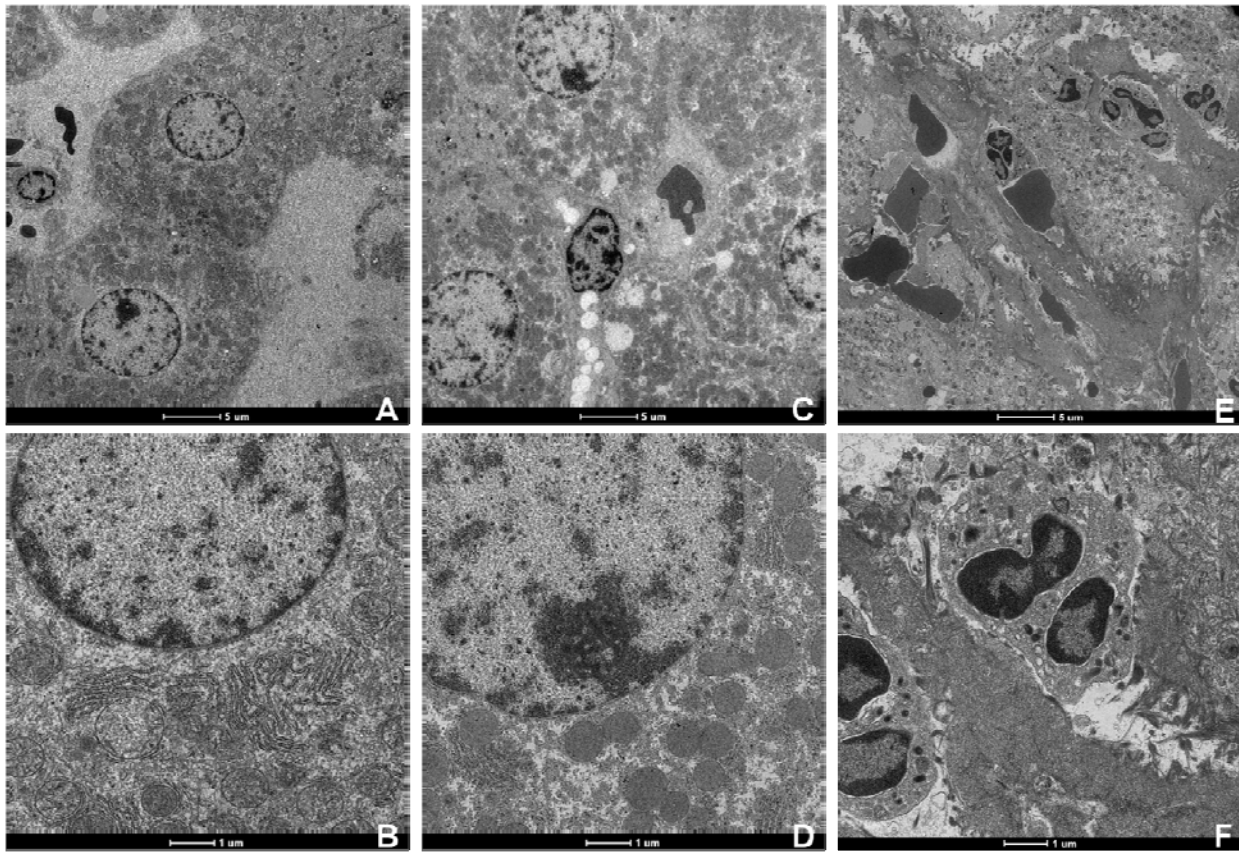


Figure 5.6: TEM images for normal liver ablation. Normal complete cell membrane, nucleus membrane and cell organelles are clear seen in untreated liver tissue (A, B). 30 minutes after IRE (C, D), pores on nuclear membrane are observed while cell membrane disappeared, but most organelles remain their structure. 24 hours after IRE (E, F), cell and nucleus boundaries are not observed; most organelles lose their structure.

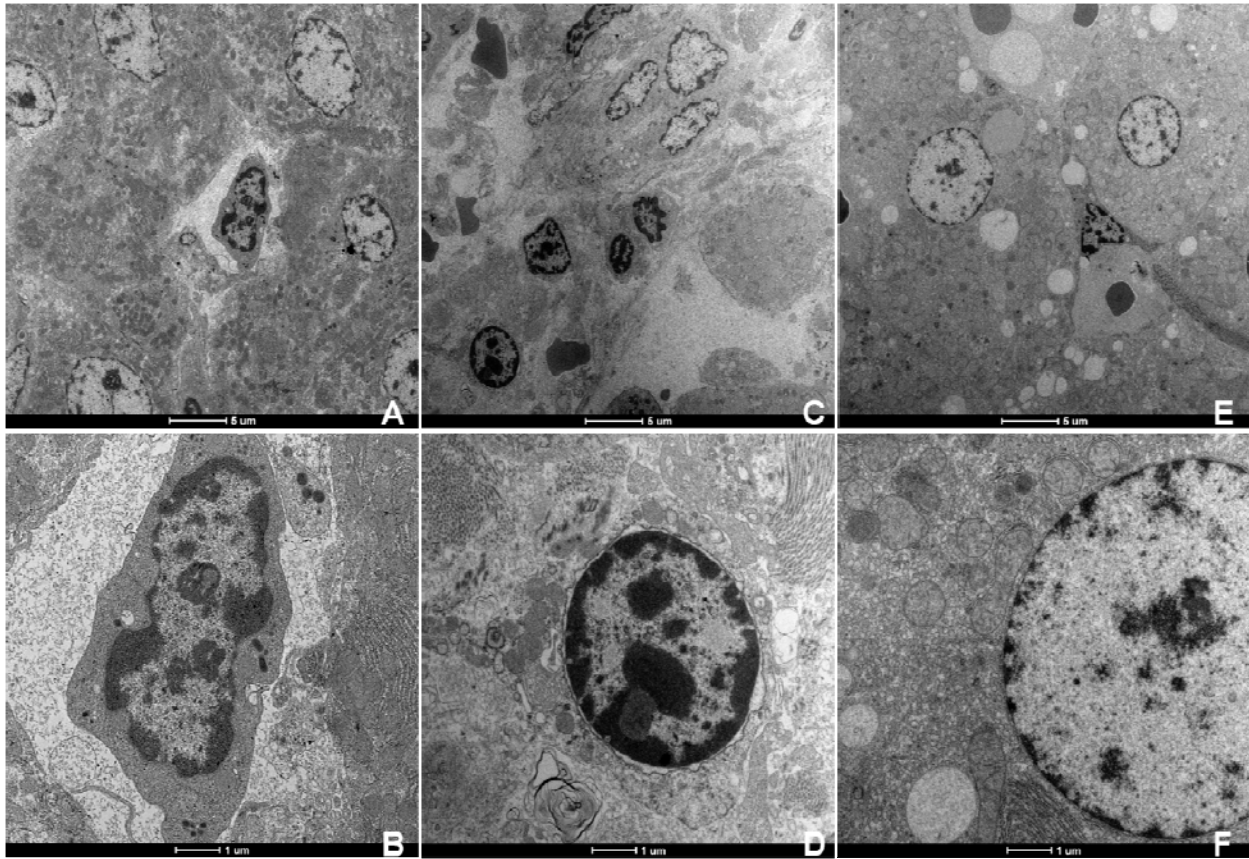


Figure 5.7: TEM images for tumor ablation. Untreated tumor cells have a larger nucleus and complete cell membrane and nucleus membrane can be noted (A, B). 30 minutes after IRE (C, D), pores on nuclear membrane are observed while cell membrane disappeared, but most organelles remain their structure. 24 hours after IRE (E, F), cell boundary can no longer be noted; most organelles lose their structure, nucleolus decrease and vacuolar degeneration is seen in cytoplasm.

5.3.4 Statistics

For US images, the average grade for echogenicity change in ablated normal liver was 2.0 and it was 1.3 for that of ablated tumor. For CT images, HU of ablated normal liver (62.53 ± 2.24) was significantly different ($p=0.0001$) from un-ablated parenchyma (46.99 ± 5.25); however, while small, the HU difference between ablated tumor (42.11 ± 2.11) and control tumor (45.14 ± 2.64) did trend toward significance ($p=0.0524$). For MR images, SNR in ablated normal liver was significantly increased post-IRE (T1W: PRE: 145.95 ± 24.32 , POST: 97.80 ± 18.03 , $p=0.0044$; T2W: PRE: 47.37 ± 18.31 , POST: 90.88 ± 37.15 , $p=0.0227$). The SNR difference between tumors pre/post-IRE was not significant (PRE: 102.13 ± 31.36 , POST: 101.09 ± 21.66 , $p=0.9401$).

5.4 DISCUSSION

IRE is a novel and potentially highly effective tissue ablation technique. Imaging monitoring approaches are crucial to optimize IRE procedures, particularly at an early stage post treatment for primary liver tumors or metastatic disease. Our studies successfully show that IRE induces rapid changes apparent on US, CT, and MR images for both normal hepatic ablation and tumor ablation. However, changes seen on gray-scale US, un-enhanced CT and T2W MRI were more dramatic when comparing the normal parenchyma to the ablated tissue than when comparing tumors pre and post ablation.

Our US finding in normal hepatic parenchyma ablation were similar to previous studies (100, 105), which demonstrate that ablated tissues appear as a hypo-echoic

focus. For tumor ablation, both normal and tumor tissues adjacent to the IRE probe became more hypo-echoic within post-IRE US. The results of echogenicity grading scale suggest that intra-procedural US monitoring of IRE is possible.

When evaluating CT images, IRE induced a large focus of low attenuation in both normal and tumor ablation. Because the tumor initially appears as a focus of hypoattenuation, the tumor margin is no longer clearly visualized on post-IRE CT. The HU measurements suggest that the HU decreases more dramatically in normal ablated tissues than pre and post IRE in tumors. However, given the dramatic tissue effect seen on CT, this imaging modality is ideal for intra-procedural imaging. At this early stage (30 minutes after IRE), only the focus of hypo-attenuation was observed without any hyper-attenuating peripheral rim. Prior studies have shown that appearance was reported at 2 days after IRE in a swine normal liver study by both unenhanced and contrast-enhanced CT(100).

Within post-IRE CT, T1W and T2W MR images, there was a well-demarcated boundary between the ablation zone and surrounding normal tissues. Within post-IRE US image, while a hypo-echoic region can be observed, the boundary between ablated tissues and surrounding tissue was hard to visualize. The reason might be that the entire ablation zone could not be captured since the US transducer can only be applied to a limited area due to the small size of a rat liver. We expect that this limitation can be overcome in a clinic setting or a large animal model.

The MR findings following hepatic ligation studies confirmed the assumption about MR signal alteration due to IRE in normal hepatic parenchyma in a previous study(104), indicating that early signal changes are likely the result of local fluid accumulation owing to transient permeabilization of blood vessels, with subsequent fluid build-up after rapid extravasation into the treated tissue zones. This can also explain why MR signal change more dramatically in normal tissues after IRE. The phenomenon of local fluid accumulation is very obvious in normal tissue ablation since a normal liver is hyper-vascular; however, N1-S1 HCC is a hypo-vascular tumor resulting in fluid build-up to a lesser extent in the tumor region.

All our image measurements (average grade for US, HU for CT and SNR for MR) indicate that IRE introduces more dramatic change in normal tissues which can be detected by conventional imaging modalities. These changes might due to the difference of tissue micro-environment between normal hepatic parenchyma and tumor: ablated normal liver can showed marked dilatation of hepatic sinusoidal spaces(105), but this was not observed in the tumor tissues.

One limitation of this study is the lack of serial monitoring after IRE. Recent studies showed IRE induced tissue damage can evolve dramatically even in the first 100 minutes(105). Additionally, early imaging is also important in a clinical setting and can provide information about the ablation zone, and whether it has completely covered the tumor volume or if further ablation is necessary. Since conventional imaging approaches in this study can only depict fluid accumulation effect after IRE, further

functional imaging methods are necessary in order to detect the direct changes caused by cell membrane permeabilization. For example, diffusion weighted imaging might provide a direct measurement of cell membrane change induced by IRE through quantifying apparent diffusion coefficient since cell membrane permeabilization after IRE might significantly change water mobility.

In conclusion, IRE induces rapid changes that can readily be seen on US, MR, and CT images. However, gray-scale US, un-enhanced CT, and T1W and T2W MRI characterized these IRE-induced signal changes were more dramatic in normal tissues than in when comparing pre and post-ablation of tumors. This study also confirms the efficacy of using these modalities in real time to monitor ablation intra-procedurally. MRI findings following hepatic ligation studies indicate that early signal changes are likely the result of local fluid accumulation in the treated tissue zones. Future studies are necessary to develop superior imaging methods to better characterize electroporation-induced changes in tumors to predict response.

6 DIFFUSION-WEIGHTED MRI FOR MONITORING IRREVERSIBLE ELECTROPORATION ABLATION OF HEPATOCELLULAR CARCINOMA IN A RODENT MODEL

6.1. INTRODUCTION

Tumor ablation therapies are very important alternative treatments for unresectable hepatocellular carcinoma. Thermal ablation treatments utilize heating-tissues interaction to achieve irreversible cellular damage(106). Radiofrequency ablation was first introduced in fresh liver from a bovine cadaver(107) and now has become the most widely used tissue ablation method due to improve regional control. Oppositely cryoablation is a process that uses freezing temperature to destroy targeted tissues(108). Other thermal ablation modalities include microwave and laser. Imaging guidance and monitoring methods has been playing a critical role in tumor ablation. Imaging guidance can serve for both real-time, targeted placement of ablation probes and functional monitoring of tissue response in these ablation procedures. MRI guidance approaches have been more intensively involved for intra-procedural monitoring of tumor ablation procedures due to excellent soft tissue contrast and the ability to non-invasively monitor temperature changes during RFA and cryotherapy (43, 45, 74). The conventional imaging techniques to evaluate tumor response mainly depend on morphological change, such as tumor size. Such morphologic changes in gross tumor size usually occur after the biological and molecular changes that happen early after the treatment.

Irreversible electroporation (IRE) has been proposed as a novel tumor ablation modality. In IRE, a short-lived but sufficiently strong electrical field across the cell membrane creates permanent nano-scale pores, which increases membrane permeability and eventually leads to cell death. IRE may offer multiple potential advantages compared to commonly used radio-frequency thermal ablation (RFA) approaches for the treatment of hepatic lesions (24, 30, 32, 73, 87). Conventional MR approaches, such as T1W and T2W MR, has been performed to detect the IRE ablation zone which is characterized as hypo-intensity within T1W and hyper-intensity within T2W(104). These signal changes within normal liver parenchyma were previously found to be due to local fluid accumulation, not cell membrane permeabilization. Diffusion-weighted MRI (DWI) is sensitive to water mobility which should be impacted by alterations to cell membrane permeability after IRE. It allows the detection of molecular motion in biological tissues and has been shown to be very sensitive to cell death and tissue damage (59-63). DWI and its corresponding quantitative apparent diffusion coefficient measurement can reflect the biological property changes that based on microstructure, cell density, and viability of the tissue(109). It has been used to assess tissue damage in many applications, including liver tumor RFA(110), chemoembolization(62), prostate cryoablation(63), and HIFU-treated uterine fibroid(60).

In this study, we used DWI to measure the IRE ablation zones and calculate the corresponding ADC change. The purpose of this study was to compare DW-MRI measurements in liver tumors before and after IRE ablation procedures in a rodent N1-S1 hepatoma model.

6.2. MATERIALS AND METHODS

6.2.1. Tumor Cell Line and Culture

The N1-S1 rat hepatoma cell line (CRL-1603, American Type Culture Collection, Manassas, Virginia) was propagated in Dulbecco's Modified Eagle's Medium (DMEM, ATCC, Manassas, Virginia) supplemented with 10% fetal bovine serum (Sigma-Aldrich) 90 µg/mL gentamicin. N1S1 cells were initially developed from carcinogenicity studies in Sprague–Dawley rats whose diet included 4-dimethylaaminoasobenzene (111). The Cells grew in suspension culture flasks at 37°C in a 95% air/5% CO₂ incubator. 5×10^6 cells were injected into liver for each implantation in order to establish tumor liver. Before each implantation procedure, >90% cell viability was confirmed by trypan blue staining.

6.2.2. Animal Model

All experiments and animal procedures were approved by the institutional animal care and use committees of University of Illinois at Chicago and Northwestern University. 18 male Sprague-Dawley rats (Charles River, Wilmington, MA) weighing 300-350g were used for these experiments and equally divided into 3 groups, in which tumors were implanted in two groups (T_A and T_B) and the other group without tumor implantation (N). After anesthesia, the left lateral lobe of rat liver was exposed and 5×10^6 N1-S1 cells were injected visually beneath the hepatic capsule into this lobe. Following the implantation, tumor growth to desired pre-treatment size generally required about 7 to 10 days. Prior to IRE and imaging procedures, Rats will be induced with isoflurane 2-4%/O₂ 1-2L for initial anesthesia and maintained with a face mask (1-

2%) during the surgery and imaging. For animals in Group TA and N, each underwent IRE procedures and then survived for 24hrs post-procedure to permit definitive formation of IRE-induced necrotic tissue regions (27, 73). For animals in Group T_B, they were euthanized immediately after IRE procedures.

6.2.3. MR Imaging

All MR imaging were performed in Group T_A(tumor) and N (normal) using a 7 Tesla animal scanner (ClinScan, Bruker BioSpin, Ettlingen, Germany) with a body coil for signal reception. Pre- and post-IRE MR imaging were performed: T1-weighted (T1W) gradient recalled echo (GRE) and T2-weighted (T2W) turbo spin-echo (TSE) images were acquired for all 3 groups; a multiple echo TSE sequence were performed for both tumor and normal groups to quantify T₂ alteration after IRE; diffusion weighted (DW) imaging were acquired in two tumor groups (TA and TB) by performing a single shot spin echo diffusion sequence. The general parameters for all sequences are slice thickness (TH) = 1mm, field of view (FOV) = 64×128 mm². The parameters for T1W and T2W are matrix = 96×192, bandwidth (BW) = 500 Hz/pixel. T1W repetition time/echo time (TR/TE) = 200/2.68ms, flip angle (FA) = 90°, number of averages (NA) = 6. T2W TR/TE ≈ 2634/44.1ms, FA=180, NA = 3. DW TR/TE = 500/47.7ms, trigger time = 660 ms, BW = 130 Hz/pixel, matrix = 64×128, NA = 5. For multiple echo TSE sequence, TE = 6.3 × [2 3 4 5 6 7] ms. DW gradients was b = 0 and 500 s/mm². Immediately following application of the IRE pulses, MR imaging measurements were repeated. In order to reduce the motion artifacts, an MR-compatible Small Animal Monitoring and Gating System (SA Instruments, Inc, Stony Brook, NY) was used during T2W TSE and DW

imaging by attaching a small pneumatic pillow to the animal abdomen to measure the respiration.

Table 6.1: MRI Parameters

	T1W	T2W	DWI
TR (ms)	200	2634	500
TE (ms)	2.68	$6.3 \times [2\ 3\ 4\ 5\ 6\ 7]$	47.7
FA (°)	90	180	90
NA	6	3	5
b (s/mm ²)			0, 500
TH (mm)	1		
FOV (mm ²)	64×128		
Matrix	96×192		64×128
BW (Hz/pixel)	500		130

6.2.4. IRE Procedures

After pre-IRE imaging, rats were removed from the MR scanner bore and remained in supine position. A surgery with midline incision at the abdomen was performed to expose the left lateral lobe of the liver. For tumor ablation (Group T_A and T_B), N1-S1 tumor within the left hepatic lobe was visually located and digitally palpated between thumb and forefinger to approximate the configuration of the tumor mass; following that, the parallel needle electrodes with 10mm distance were positioned in the way that the two-needle insertion positions were aligned along the axis of the largest tumor dimension. For normal hepatic parenchyma (Group N) ablation, the same needle electrodes were inserted into the center of the left lateral lobe. 10mm electrode separation was maintained by insertion of the needles through holes drilled within a 15mm thick plastic spacing block. After insertion, electrodes were connected to IRE function generator (Electroporator ECM830; BTX Division of Harvard Apparatus, Holliston, MA). For IRE procedures, 2500V square wave pulses were applied to the 2 parallel electrodes with following protocol: total number of pulses = 8, duration of each pulse = 100 μ s, and interval between two pulses = 100 ms. Immediately after application of the IRE pulses, electrodes were disconnected and post-IRE MR imaging was performed in Group T_A(tumor) and N (normal).

6.2.5. Histological Evaluation

The animals in Groups T_A and N were euthanized 24 hours after electroporation. The animals in Groups T_B were euthanized immediately after post-IRE imaging scans. These rats were euthanized and livers harvested for subsequent necropsy. Livers were

fixed in 10% buffered formaldehyde solution, sliced at 3mm intervals, and embedded in paraffin for histological examination. Liver sections were sliced in 4 μ m thick sections and stained using hematoxylin and eosin (H&E). Overview histological slides were digitized with an optical image acquisition system (TissueGnostics, Vienna, Austria) at $\times 20$ magnification. These slides were also scanned by CRi NUANCE Multispectral Imaging Systems (Advanced Molecular Vision Inc., Grantham, Lincolnshire, United Kingdom) with $\times 100$ magnification to observe cellular change detail.

6.2.6. Data Analysis

T1W and T2W MR images were analyzed with the ImageJ software package (NIH). For these images, signal to noise ratio (SNR) were measured based on regions of interest (ROIs) on ablated normal tissues, un- ablated normal tissue, ablated tumor and un-ablated tumor. T2 relaxation maps and ADC maps were obtained by offline using Matlab software (MathWorks, Natick, MA). T2 maps at each slice position were reconstructed from the TE images with TE = 6.3 \times [2 3 4 5 6 7] ms. T2 values for each pixel were computed by employing the nonlinear Levenberg–Marquardt algorithm to fit the monoexponential decay function $S(TE_i) = M_0 \cdot \exp(-TE_i/T_2)$, where $S(TE_i)$ denoted the signal intensity at the TE_i image and M_0 denotes the proton density. Tumor ADC parametric maps were reconstructed from each set of DW images acquired at each slice position. ROIs of tumor were draw based on b=0 DW images. ADC values for each pixel were calculated as the slope of the least-squares fit line to the function: $ADC \cdot b = \log(S(b)/S(0))$, with $S(b)$ denoting the voxel signal intensity in the image with diffusion weighting of b.

6.2.7. Statistical Analysis

Paired t-test was performed to compare the SNR measurements of pre- and post-IRE T1W and T2W. These analyses were implemented with the SPSS Version 17 software package (Chicago, IL) with p-values less than 0.05 considered statistically significant.

6.3. RESULTS

6.3.1. MRI Measurements

Fig.6.1 showed representative T1W GRE images before and immediately after application 2500V IRE pulses from Group N (Fig.6.1A and Fig.6.1B) and Group T_A (Fig.6.1C and Fig.6.1D). IRE impacted tissues were hypo-intense within T1W images and were clearly demarcated from surrounding normal hepatic parenchyma. Pre-IRE Tumors appeared as hypo-intense within T1W images (Fig.6.1C); After IRE, a large hypo-intense area appeared as the ablation region within T1W image (Fig.6.1D)

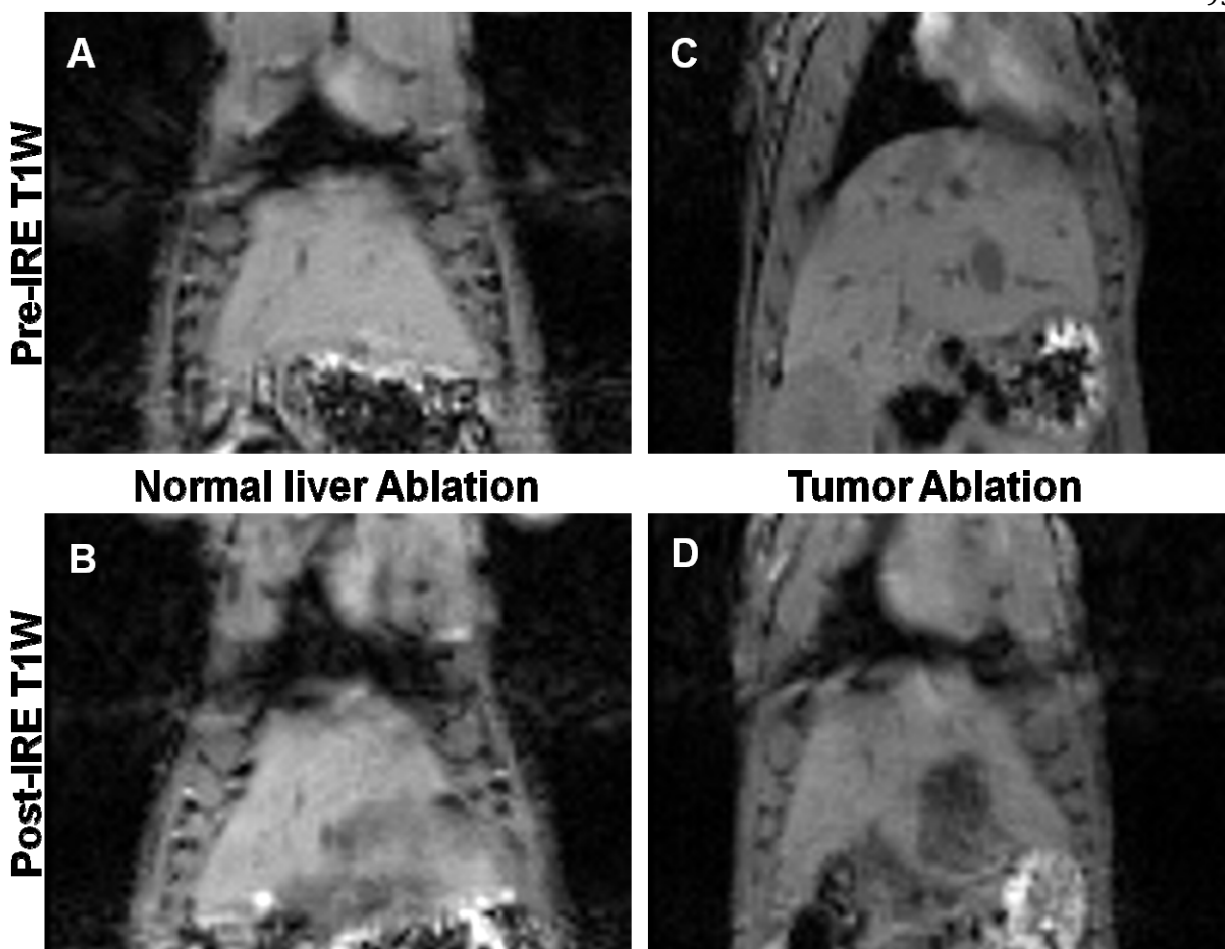


Figure 6.1: Representative T1W MRI before and after IRE within normal liver parenchyma (A and B) and tumor liver (C and D). Ablated normal tissue appeared as hypo-intensity within post-IRE T1W (B). A large hypo-intensity zone appeared to cover the tumor for tumor ablation (D).

Fig.6.2 showed representative multiple echo T2W TSE images and corresponding T2 maps from normal liver ablation pre- and post-IRE. Electroporated liver tissues appeared as hyper-intense within T2W images at TE= 12.6ms and TE = 44.1ms. Corresponding T2 maps indicate IRE ablated tissue has a higher T2 value than that before IRE. Fig.6.3 showed representative multiple echo T2W TSE images and corresponding T2 maps from tumor ablation. Pre-IRE Tumors appeared as hyper-intense within T2W images at TE= 12.6ms (Fig.3A) and TE = 44.1ms (Fig.3B); after IRE, a large hyper-intense region of ablated normal tissues appeared surrounding the central hyper-intense tumor in T2W images (Fig.6.3D and Fig.6.3E). The resultant T2 maps showed tumor T2 dropped while surrounding normal tissue T2 increased.

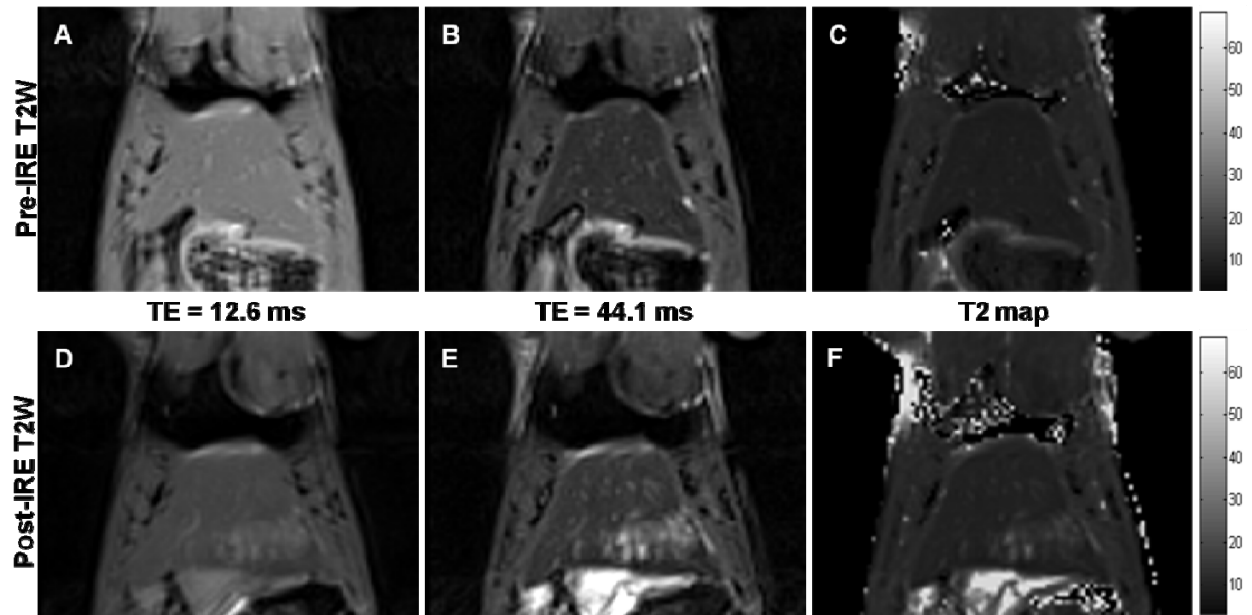


Figure 6.2: Representative multiple-echo TSE T2W MRI and the corresponding T2 maps before (A, B and C) and after IRE (D, E and F) within normal liver parenchyma. Ablated normal tissue appeared as slightly hyper-intensity within post-IRE T2W at TE = 12.6 ms (D) and hyper-intensity at TE = 44.1 ms (E). T2 maps indicated increased T2 within ablated normal tissues. In this case, average T2pre = 20.93 ms, and T2post = 32.77 ms.

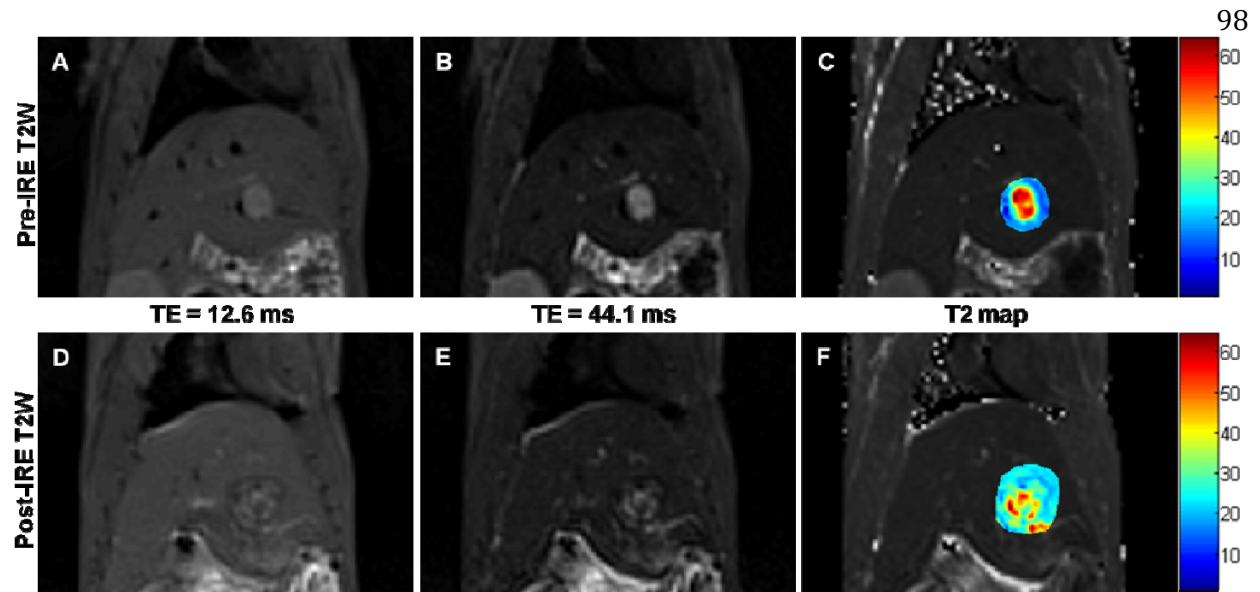


Figure 6.3: Representative multiple-echo TSE T2W MRI and the corresponding T2 maps before (A, B and C) and after IRE (D, E and F) for a tumor liver ablation. A large ablation zone appeared as hyper-intensity to cover the tumor within both post-IRE T2W at TE = 12.6 ms (D) and at TE = 44.1 ms (E). Small colored T2 maps overlaid with gray-scale T2maps (C and F) indicating decreased T2 within tumor after IRE. In this case, average tumor T2pre = 51.59ms, and T2post = 35.76ms.

A representative example of DW images with corresponding ADC map was shown in Fig.6.4. The HCC tumor was hyper-intense in DW image ($b = 0 \text{ s/mm}^2$) (Fig. 4A). At the higher diffusion weighting, HCC demonstrated less signal suppression than surrounding liver tissues (Fig. 6.4B). The corresponding ADC maps demonstrated that tumor ADC decreased after IRE.

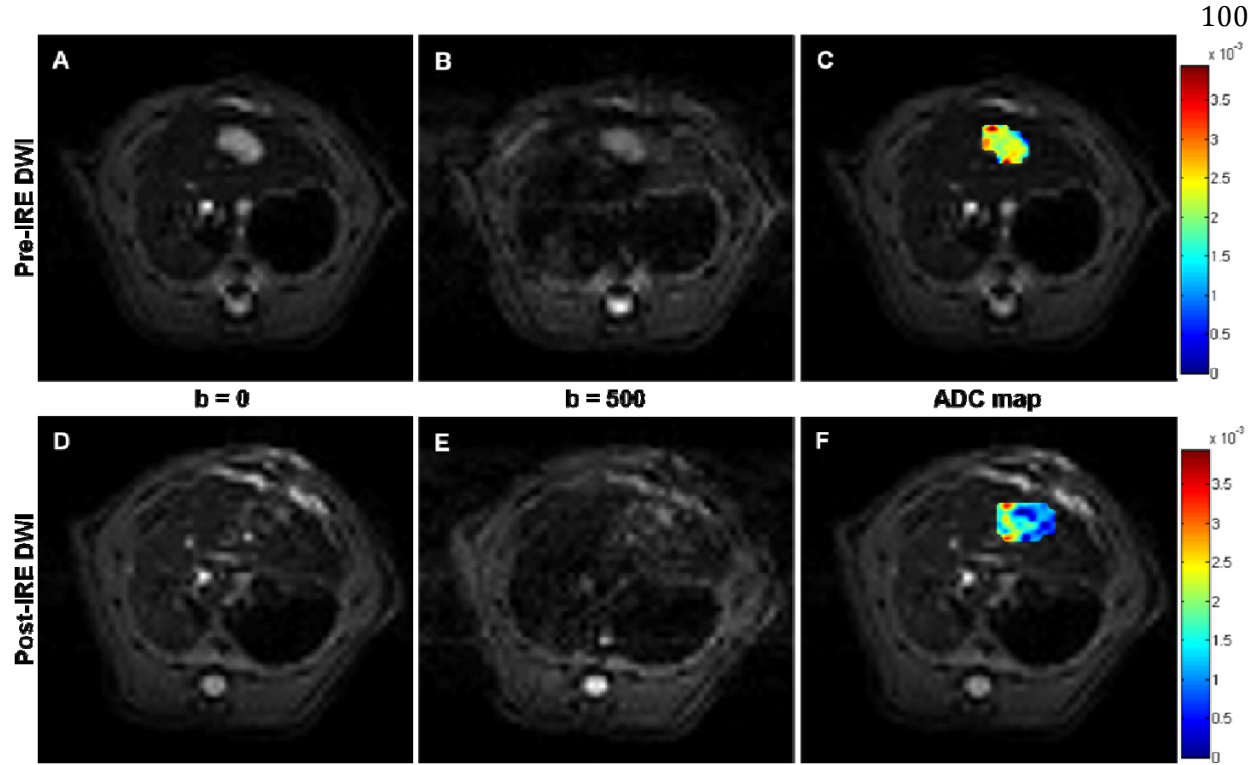


Figure 6.4: Representative DW MRI and the corresponding tumor ADC maps before (A, B and C) and after IRE (D, E and F) for a tumor liver ablation. The DW signal intensity within the tumor decayed less than that within the normal liver within both DW images at $b = 500 \text{ s/mm}^2$. The tumor region ADC maps overlaid with DW image at $b = 0$, indicating decreased ADC within tumor after IRE. In this case, average tumor $\text{ADC}_{\text{pre}} = (1.788 \pm 0.662) \times 10^{-3} \text{ mm}^2/\text{s}$, and $\text{ADC}_{\text{post}} = (1.386 \pm 0.505) \times 10^{-3} \text{ mm}^2/\text{s}$.

6.3.2. Histology

Fig.5 showed the result of an H&E staining of normal hepatic parenchyma ablation: the ablated zone immediately (approximately 30 minutes) after IRE became slightly pale compared to non-ablated zone, indicating eosinophilic structures degenerated, like cytoplasm and extracellular spaces; the nuclear remained their structures. Fig.6 showed normal liver tissues 1 day after IRE: the electroporated regions turned clear pale compared to periphery non-ablated normal liver tissues; some of nuclears decreased their size indicating the coagulation necrosis; lots of red blood cells appeared at extracellular spaces. Fig.7 showed the result of an H&E staining of tumor ablation: the ablation zones covered the entire tumors within both immediate and 1 day H&E staining; the tumor cells arranged loosely compared to control tumor cells. Some nucleus agglutinations can be seen at 30 minutes; nuclear cytoplasm ratio increases 24 hours after IRE.

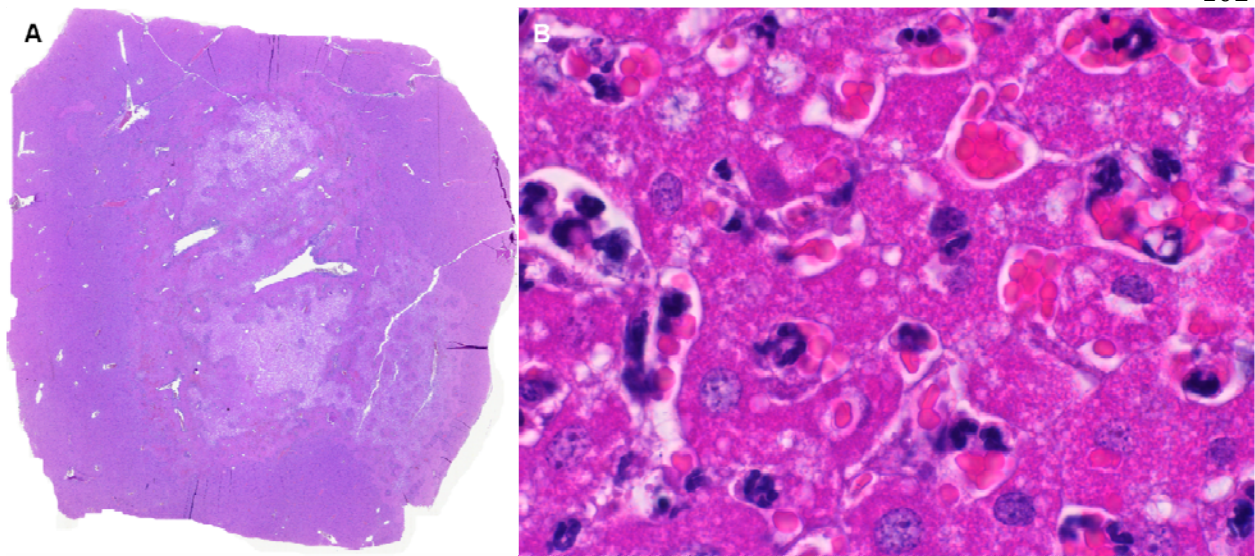


Figure 6.5: Representative H&E staining for a normal liver sacrifice 1 day after IRE. The region overview showed a well-delineated boundary between untreated and ablated tissues with cellular necrosis within ablation zone (A: original magnification $\times 2.5$). A detailed view within the ablation zone showed nuclear degeneration and remarkable hemorrhage was observed (B: original magnification $\times 100$).

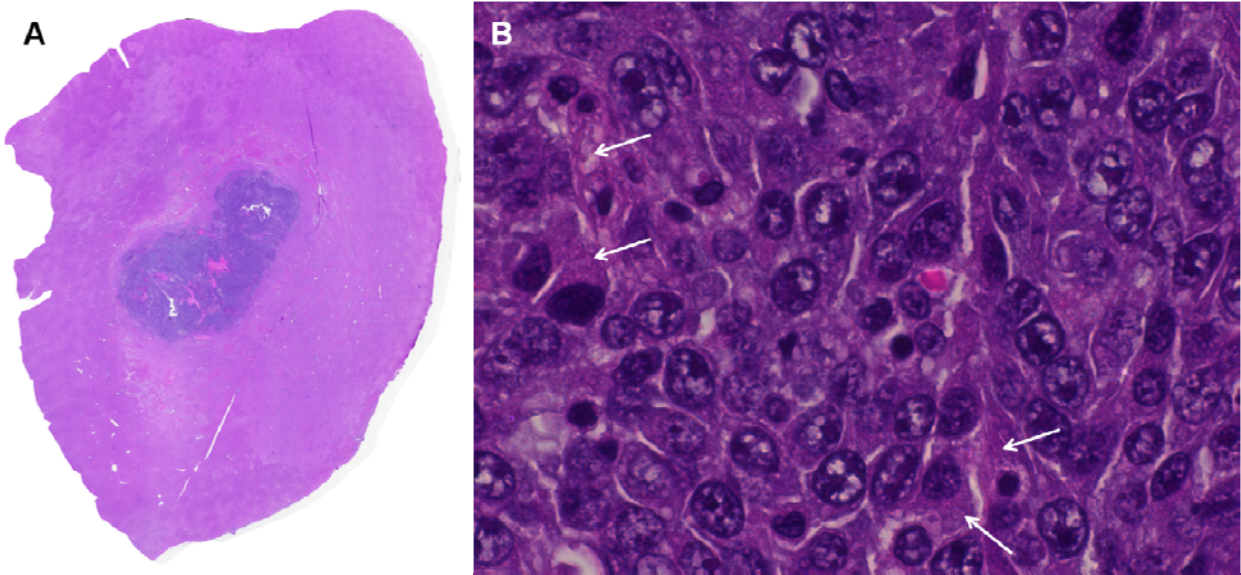


Figure 6.6: Representative H&E staining for a tumor sacrifice immediately after IRE. Tissue necrosis was not clearly observed within the ablation zone (A: original magnification $\times 20$). A detailed view within the tumor indicated cellular swelling (white arrows), no hemorrhage was observed (B: original magnification $\times 100$).

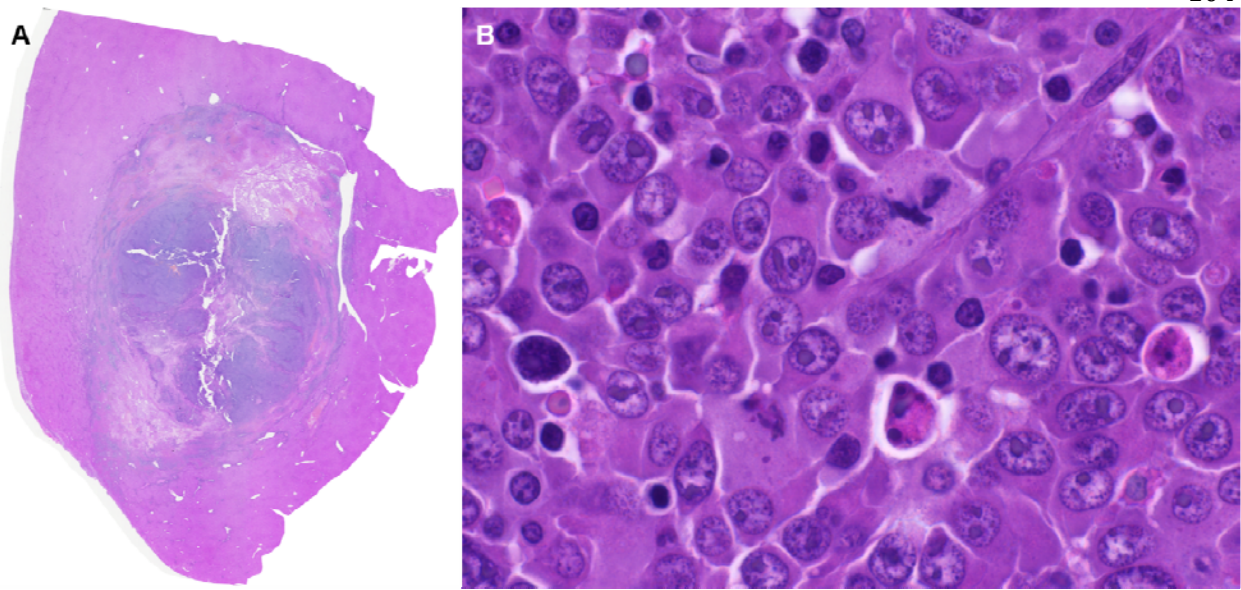


Figure 6.7: Representative H&E staining for a tumor sacrifice 1 day after IRE. The region overview showed a well-delineated boundary between untreated and ablated tissues with cellular necrosis within ablation zone (A: original magnification $\times 20$). A detailed view within the tumor showed tumor cells became loosely arranged. More extracellular space appeared and no hemorrhage was observed. (B: original magnification $\times 100$).

6.3.3. Comparison of SNR, T2 and ADC between pre- and post-IRE

The SNR of ablated normal liver was significantly different from pre-IRE normal liver for T1W images (Pre= 145.95 ± 24.32 , Post= 97.80 ± 18.03 , $p=0.0044$) and T2W (Pre= 47.37 ± 18.31 , Post= 90.88 ± 37.15 , $p=0.0227$); but SNR of tumor before and after IRE were not significantly different (Pre= 77.04 ± 9.43 , Post= 67.51 ± 14.7543 , $p=0.1342$ for T1W; Pre= 101.09 ± 21.66 , Post= 102.13 ± 31.36 , $p=0.9401$ for T2W). Normal liver T2 increased significantly (Pre= $21.00 \pm 1.08\text{ms}$, Post= $30.14 \pm 2.42\text{ms}$, $p<0.001$) but tumor T2 decreased significantly (Pre= $49.84 \pm 2.62\text{ms}$, Post= $41.17 \pm 5.27\text{ms}$, $p=0.021$). ADC within tumor tissues also significantly decreased (Pre= $1.79 \pm 0.66 \times 10^{-3} \text{mm}^2/\text{s}$, Post= $1.39 \pm 0.51 \times 10^{-3} \text{mm}^2/\text{s}$, $p=0.019$).

6.4. DISCUSSION

In this preclinical study we demonstrated the change of the ADC within liver tumor after IRE ablation. The ADC value within tumor after IRE was lower than that before treatment, which indicates restricted water movement due to cellular disruption macromolecular denaturation. Our result is similar to the cryoablation in the canine prostates in which ADC decreased 36%(63). The similar observation was also noted in a focused ultrasound surgical ablation of uterine fibroids from $1.685 \pm 0.468 \text{mm}^{-3}/\text{sec}^2$ to $1.078 \pm 0.293 \text{mm}^{-3}/\text{sec}$ (60). The similar results are also found in non-ablation procedures, one is regional cerebral ischemia in cats due to a unilateral middle cerebral and bilateral carotid artery occlusion(112), the other is postmortem rat brain tissues(113). A significant decrease in ADC was observed in an orthotopic mouse glioma 2–3 days after cediranib treatment (114). In our case, we speculated the

decrease of ADC might be explained as intracellular retention of water (known as cytotoxic edema or cellular swelling) since electroporation breaks down the transmembrane ionic equilibrium, which decreases ADC. The cellular swelling can be observed in the immediately harvested tumor.

The accurate timing evolution of the ADC in N1-S1 tumor tissue is still unknown at the present time and needs further investigation. The previous study in normal canine prostate showed the ADC decrease occurred early during the course of the treatment increased over time as the tissue recovered and regenerated(63). The study of focused ultrasound therapy in patients' uterine fibroids also demonstrated the ADC increased at six month follow-up even with immediate reduction after the treatment(60). However, the time intervals these studies investigated about ADC change are several days up to month. For IRE, a complete time course after ablation from early stage (30 minutes, 1 hour, and 3 hours) to later stage (1 day, 7day) will be more valuable. Particularly, the ADC at different time points in the early stage will provide more information of cellular membrane change. So future studies should be investigated the ADC changes at multiple time points.

In this study, we also demonstrated T2 within normal liver parenchyma (Group N) significantly increased after IRE ablation by using T2 mapping approach, which agreed on our previous study in normal liver with T2W MRI. From T2 maps in tumor ablation group, the T2 within tumor tissues decreased while the T2 within surrounding normal tissue increased. Our tumor T2 alteration is in agreement with a previous study of neuroblastoma to antivasular therapy in a transgenic mouse model (115). Similarly, a

statistically significant mean reduction of $T2^*$ was found in rabbit VX2 liver tumor after transcatheter arterial embolization, from 55 ms before embolization to 41 ms after embolization (116).

Both dynamic contrast-enhanced (DCE) MRI (117) and DWI(118) are two major quantitative modalities and have been widely used to evaluate tumor response (119). While DCE has been broadly advocated to measure tumor vascular integrity and to assess anti-tumor drug efficacy (120), it still need contrast-agent which might be toxic to patients with renal dysfunction (121). We choose DWI in this study because it is non-invasive approach to provide quantitative information related with early physiology change. Meanwhile, no external contrast source is induced so that ADC value might directly suggest membrane permeability change only due to electroporation effect.

The IRE procedures were performed in N1-S1 HCC model which is a hypovasucular tumor model. However, most patients' liver tumors are hypervascular. Future studies are clearly warranted to further investigate the ADC changes in hypervascular tumor model, like MCARH7777. In this study, the advantage of N1-S1 model is to exclude tumor blood flow impact on cell permeability change after IRE.

An additional limitation of this study was the low b value used for DWI due to limited SNR in this small animal study. Advanced MRI technique with motion reduction should be investigated to improve DWI image quality at high b value. Multiple b values should be included in future studies to improve the fitting accuracy.

In conclusion, DW imaging and ADC mapping are potential techniques for identifying and monitoring ablated liver tumor after IRE treatment.

7. SUMMARY AND FUTURE DIRECTIONS

This dissertation was composed of four studies. In the first study, conventional MRI measurements were performed before and immediate after IRE in a normal liver rat model to evaluate the imaging characteristics. MRI-based ablation zone was measured and showed a high correlation with histology-confirmed ablation zone. This study demonstrated the potential to use MRI measurements to monitor IRE zones in rat liver tissues.

This work next developed a MRI-based pre-procedural FEM simulation method to predict IRE ablation zone in a rat liver tumor model. T2-weighted TSE images were used to create a 3D virtual liver model which is based on the actual tumor size and shape. Simulated ablation zone was measured and demonstrated a high correlation with histology-confirmed ablation zone.

This work also addressed the application of multi-modality imaging before and after IRE. Ultrasound, CT and MRI were performed in normal liver model and liver tumor model to evaluate the imaging characteristics after the ablation. The echogenecity changes for Ultrasound, the Hounsfield units for CT and signal-to noise ratios for MRI were measured.

Diffusion-weighted and multiple echoes T2-weighted turbo spin echo MRI were performed before and immediate after IRE in a rat liver tumor model. Quantitative apparent diffusion coefficient and T2 maps were used to investigate cell membrane permeability change after IRE.

In summary, MRI can be used during treatment to elicit repeat application of IRE pulses or adjustments to electrode positions to ensure complete treatment of targeted lesions.

Further studies are clearly necessary to fully investigate longitudinal imaging response after IRE. A complete time course after ablation from early stage (30 minutes, 1 hour, and 3 hours) to later stage (1 day, 7day) will be more valuable to understand the tissue evolution after IRE, including imaging signal change by conventional MRI and quantitative parametric maps by DWI.

The tumor model used in this work is N1-S1 cell line and its resultant HCC is hypovascular. However, hypervascular HCC is more common in clinic. So future studies are clearly warranted to further investigate the tissue response within hypervascular HCC. MCARH7777 cell line is well established in current experiment environment and can grow hypervascular HCC at desire size to be used for such investigations.

Another direction is to correlate imaging biomarkers with histology markers. Caspase-3 and terminal deoxynucleotidyl transferase-mediated nick-end labeling

(TUNEL) assay can both be used to evaluate apoptosis index. The necrosis rate (percentage of necrosis area in tumor) can be measured based on HE staining. The correlation between these histological markers and Quantitative MRI parameters, such as ΔT_2 and ΔADC can be measured to investigate the potential MRI biomarkers.

Additionally MRI monitoring IRE method could also be used to treat prostate or pancreatic tumor. Future studies could be sought to find out the benefit for these tumor models.

REFERENCES

1. Ferlay J, Shin HR, Bray F, Forman D, Mathers C, Parkin DM. Estimates of worldwide burden of cancer in 2008: GLOBOCAN 2008. *Int J Cancer*. 2010;127(12):2893-917.
2. Di Bisceglie AM. Epidemiology and clinical presentation of hepatocellular carcinoma. *J Vasc Interv Radiol*. 2002;13(9 Pt 2):S169-71.
3. El-Serag HB. Hepatocellular carcinoma: an epidemiologic view. *J Clin Gastroenterol*. 2002;35(5 Suppl 2):S72-8.
4. Society AC. Cancer Facts and Figures 2013. Atlanta, Ga: American Cancer Society, 2013. 2013.
5. Llovet JM, Burroughs A, Bruix J. Hepatocellular carcinoma. *Lancet*. 2003;362(9399):1907-17.
6. Daniele B, Bencivenga A, Megna AS, Tinessa V. Alpha-fetoprotein and ultrasonography screening for hepatocellular carcinoma. *Gastroenterology*. 2004;127(5 Suppl 1):S108-12.
7. Bruix J, Sherman M. Management of hepatocellular carcinoma: an update. *Hepatology*. 2011;53(3):1020-2.
8. Altekruse SF, McGlynn KA, Reichman ME. Hepatocellular carcinoma incidence, mortality, and survival trends in the United States from 1975 to 2005. *J Clin Oncol*. 2009;27(9):1485-91.
9. El-Serag HB. Hepatocellular carcinoma. *N Engl J Med*. 2011;365(12):1118-27.
10. Marcos-Alvarez A, Jenkins RL, Washburn WK, et al. Multimodality treatment of hepatocellular carcinoma in a hepatobiliary specialty center. *Arch Surg*. 1996;131(3):292-8.
11. Ziser A, Plevak DJ, Wiesner RH, Rakela J, Offord KP, Brown DL. Morbidity and mortality in cirrhotic patients undergoing anesthesia and surgery. *Anesthesiology*. 1999;90(1):42-53.
12. Gozzetti G, Mazziotti A, Cavallari A, et al. Hepatic resection for tumours in cirrhotic livers. *Int Surg*. 1987;72(2):82-6.

13. Obed A, Tsui TY, Schnitzbauer AA, et al. Liver transplantation as curative approach for advanced hepatocellular carcinoma: is it justified? *Langenbecks Arch Surg.* 2008;393(2):141-7.
14. Cillo U, Vitale A, Bassanello M, et al. Liver transplantation for the treatment of moderately or well-differentiated hepatocellular carcinoma. *Ann Surg.* 2004;239(2):150-9.
15. Chow PK, Tai BC, Tan CK, et al. High-dose tamoxifen in the treatment of inoperable hepatocellular carcinoma: A multicenter randomized controlled trial. *Hepatology.* 2002;36(5):1221-6.
16. Livraghi T, Solbiati L, Meloni MF, Gazelle GS, Halpern EF, Goldberg SN. Treatment of focal liver tumors with percutaneous radio-frequency ablation: complications encountered in a multicenter study. *Radiology.* 2003;226(2):441-51.
17. Lao OB, Farjah F, Flum DR, Yeung RS. Adverse events after radiofrequency ablation of unresectable liver tumors: a single-center experience. *Am J Surg.* 2009;198(1):76-82.
18. Llovet JM, Vilana R, Bru C, et al. Increased risk of tumor seeding after percutaneous radiofrequency ablation for single hepatocellular carcinoma. *Hepatology.* 2001;33(5):1124-9.
19. Neumann E, Schaefer-Ridder M, Wang Y, Hofschneider PH. Gene transfer into mouse lyoma cells by electroporation in high electric fields. *EMBO J.* 1982;1(7):841-5.
20. Rols MP, Delteil C, Golzio M, Dumond P, Cros S, Teissie J. In vivo electrically mediated protein and gene transfer in murine melanoma. *Nat Biotechnol.* 1998;16(2):168-71.
21. Mir LM, Glass LF, Sersa G, et al. Effective treatment of cutaneous and subcutaneous malignant tumours by electrochemotherapy. *Br J Cancer.* 1998;77(12):2336-42.
22. Tsoneva I, Iordanov I, Berger AJ, et al. Electrodilivery of drugs into cancer cells in the presence of poloxamer 188. *J Biomed Biotechnol.* 2010;2010.
23. Oshima T, Sato M. Bacterial sterilization and intracellular protein release by a pulsed electric field. *Adv Biochem Eng Biotechnol.* 2004;90:113-33.
24. Davalos RV, Mir IL, Rubinsky B. Tissue ablation with irreversible electroporation. *Ann Biomed Eng.* 2005;33(2):223-31.
25. Miller L, Leor J, Rubinsky B. Cancer cells ablation with irreversible electroporation. *Technol Cancer Res Treat.* 2005;4(6):699-705.

26. Edd JF, Horowitz L, Davalos RV, Mir LM, Rubinsky B. In vivo results of a new focal tissue ablation technique: irreversible electroporation. *IEEE Trans Biomed Eng.* 2006;53(7):1409-15.
27. Rubinsky B, Onik G, Mikus PI. Irreversible electroporation: a new ablation modality--clinical implications. *Technol Cancer Res Treat.* 2007;6(1):37-48.
28. Miklavcic D, Semrov D, Mekid H, Mir LM. A validated model of in vivo electric field distribution in tissues for electrochemotherapy and for DNA electrotransfer for gene therapy. *Biochim Biophys Acta.* 2000;1523(1):73-83.
29. Onik G, Mikus P, Rubinsky B. Irreversible electroporation: implications for prostate ablation. *Technol Cancer Res Treat.* 2007;6(4):295-300.
30. Maor E, Ivorra A, Leor J, Rubinsky B. The effect of irreversible electroporation on blood vessels. *Technol Cancer Res Treat.* 2007;6(4):307-12.
31. Edd JF, Davalos RV. Mathematical modeling of irreversible electroporation for treatment planning. *Technol Cancer Res Treat.* 2007;6(4):275-86.
32. Al-Sakere B, Bernat C, Andre F, et al. A study of the immunological response to tumor ablation with irreversible electroporation. *Technol Cancer Res Treat.* 2007;6(4):301-6.
33. Granot Y, Rubinsky B. Methods of optimization of electrical impedance tomography for imaging tissue electroporation. *Physiol Meas.* 2007;28(10):1135-47.
34. Davalos RV, Otten DM, Mir LM, Rubinsky B. Electrical impedance tomography for imaging tissue electroporation. *IEEE Trans Biomed Eng.* 2004;51(5):761-7.
35. Bennett GL, Krinsky GA, Abitbol RJ, Kim SY, Theise ND, Teperman LW. Sonographic detection of hepatocellular carcinoma and dysplastic nodules in cirrhosis: correlation of pretransplantation sonography and liver explant pathology in 200 patients. *AJR Am J Roentgenol.* 2002;179(1):75-80.
36. Rode A, Bancel B, Douek P, et al. Small nodule detection in cirrhotic livers: evaluation with US, spiral CT, and MRI and correlation with pathologic examination of explanted liver. *J Comput Assist Tomogr.* 2001;25(3):327-36.
37. Bartolozzi C, Lencioni R, Caramella D, Palla A, Bassi AM, Di Candio G. Small hepatocellular carcinoma. Detection with US, CT, MR imaging, DSA, and Lipiodol-CT. *Acta Radiol.* 1996;37(1):69-74.
38. Ueda K, Kitagawa K, Kadoya M, Matsui O, Takashima T, Yamahana T. Detection of hypervascular hepatocellular carcinoma by using spiral volumetric CT: comparison of US and MR imaging. *Abdom Imaging.* 1995;20(6):547-53.

39. Prat F, Centarti M, Sibille A, et al. Extracorporeal high-intensity focused ultrasound for VX2 liver tumors in the rabbit. *Hepatology*. 1995;21(3):832-6.
40. Sibille A, Prat F, Chapelon JY, et al. Characterization of extracorporeal ablation of normal and tumor-bearing liver tissue by high intensity focused ultrasound. *Ultrasound Med Biol*. 1993;19(9):803-13.
41. Boaz TL, Lewin JS, Chung YC, Duerk JL, Clampitt ME, Haaga JR. MR monitoring of MR-guided radiofrequency thermal ablation of normal liver in an animal model. *J Magn Reson Imaging*. 1998;8(1):64-9.
42. Merkle EM, Boll DT, Boaz T, et al. MRI-guided radiofrequency thermal ablation of implanted VX2 liver tumors in a rabbit model: demonstration of feasibility at 0.2 T. *Magn Reson Med*. 1999;42(1):141-9.
43. Lewin JS, Connell CF, Duerk JL, et al. Interactive MRI-guided radiofrequency interstitial thermal ablation of abdominal tumors: clinical trial for evaluation of safety and feasibility. *J Magn Reson Imaging*. 1998;8(1):40-7.
44. Breen MS, Lazebnik RS, Fitzmaurice M, Nour SG, Lewin JS, Wilson DL. Radiofrequency thermal ablation: correlation of hyperacute MR lesion images with tissue response. *J Magn Reson Imaging*. 2004;20(3):475-86.
45. Quesson B, de Zwart JA, Moonen CT. Magnetic resonance temperature imaging for guidance of thermotherapy. *J Magn Reson Imaging*. 2000;12(4):525-33.
46. Germain D, Chevallier P, Laurent A, Saint-Jalmes H. MR monitoring of tumour thermal therapy. *MAGMA*. 2001;13(1):47-59.
47. Matsumoto R, Oshio K, Jolesz FA. Monitoring of laser and freezing-induced ablation in the liver with T1-weighted MR imaging. *J Magn Reson Imaging*. 1992;2(5):555-62.
48. Matsumoto R, Selig AM, Colucci VM, Jolesz FA. MR monitoring during cryotherapy in the liver: predictability of histologic outcome. *J Magn Reson Imaging*. 1993;3(5):770-6.
49. Hong JS, Wong S, Pease G, Rubinsky B. MR imaging assisted temperature calculations during cryosurgery. *Magn Reson Imaging*. 1994;12(7):1021-31.
50. Pease GR, Wong ST, Roos MS, Rubinsky B. MR image-guided control of cryosurgery. *J Magn Reson Imaging*. 1995;5(6):753-60.
51. Tacke J, Adam G, Speetzen R, et al. MR-guided interstitial cryotherapy of the liver with a novel, nitrogen-cooled cryoprobe. *Magn Reson Med*. 1998;39(3):354-60.

52. Rubinsky B, Lee CY, Bastacky J, Onik G. The process of freezing and the mechanism of damage during hepatic cryosurgery. *Cryobiology*. 1990;27(1):85-97.
53. Silverman SG, Tuncali K, Adams DF, et al. MR imaging-guided percutaneous cryotherapy of liver tumors: initial experience. *Radiology*. 2000;217(3):657-64.
54. Mueller-Lisse UG, Heuck AF, Thoma M, et al. Predictability of the size of laser-induced lesions in T1-Weighted MR images obtained during interstitial laser-induced thermotherapy of benign prostatic hyperplasia. *J Magn Reson Imaging*. 1998;8(1):31-9.
55. Mueller-Lisse UG, Heuck AF, Schneede P, et al. Postoperative MRI in patients undergoing interstitial laser coagulation thermotherapy of benign prostatic hyperplasia. *J Comput Assist Tomogr*. 1996;20(2):273-8.
56. Boni RA, Sulser T, Jochum W, Romanowski B, Debatin JF, Krestin GP. Laser ablation-induced changes in the prostate: findings at endorectal MR imaging with histologic correlation. *Radiology*. 1997;202(1):232-6.
57. Mueller-Lisse UG, Thoma M, Faber S, et al. Coagulative interstitial laser-induced thermotherapy of benign prostatic hyperplasia: online imaging with a T2-weighted fast spin-echo MR sequence--experience in six patients. *Radiology*. 1999;210(2):373-9.
58. Vogl TJ, Muller PK, Hammerstingl R, et al. Malignant liver tumors treated with MR imaging-guided laser-induced thermotherapy: technique and prospective results. *Radiology*. 1995;196(1):257-65.
59. Butts K, Daniel BL, Chen L, et al. Diffusion-weighted MRI after cryosurgery of the canine prostate. *Magnetic resonance imaging*. *J Magn Reson Imaging*. 2003;17(1):131-5.
60. Jacobs MA, Herskovits EH, Kim HS. Uterine fibroids: diffusion-weighted MR imaging for monitoring therapy with focused ultrasound surgery--preliminary study. *Radiology*. 2005;236(1):196-203.
61. Lang P, Wendland MF, Saeed M, et al. Osteogenic sarcoma: noninvasive in vivo assessment of tumor necrosis with diffusion-weighted MR imaging. *Radiology*. 1998;206(1):227-35.
62. Geschwind JF, Artemov D, Abraham S, et al. Chemoembolization of liver tumor in a rabbit model: assessment of tumor cell death with diffusion-weighted MR imaging and histologic analysis. *J Vasc Interv Radiol*. 2000;11(10):1245-55.
63. Chen J, Daniel BL, Diederich CJ, et al. Monitoring prostate thermal therapy with diffusion-weighted MRI. *Magn Reson Med*. 2008;59(6):1365-72.

64. Dirac P. The quantum theory of the electron. *Proceedings of the Royal Society of London Series A, Containing Papers of a Mathematical and Physical Character*. 1928;117(778):610-24.
65. Haacke E, Brown R, Thompson M, Venkatesan R. *Magnetic resonance imaging: physical principles and sequence design*: Wiley New York, 1999.
66. Nishimura D. *Principles of magnetic resonance imaging*: Stanford University Stanford, 1995.
67. Neumann E, Rosenheck K. Permeability changes induced by electric impulses in vesicular membranes. *J Membr Biol*. 1972;10(3):279-90.
68. Paunesku T, Ke T, Dharmakumar R, et al. Gadolinium-conjugated TiO₂-DNA oligonucleotide nanoconjugates show prolonged intracellular retention period and T1-weighted contrast enhancement in magnetic resonance images. *Nanomedicine*. 2008;4(3):201-7.
69. Leroy-Willig A, Fromes Y, Paturneau-Jouas M, Carlier P. Assessing gene and cell therapies applied in striated skeletal and cardiac muscle: is there a role for nuclear magnetic resonance? *Neuromuscul Disord*. 2003;13(5):397-407.
70. Leroy-Willig A, Bureau MF, Scherman D, Carlier PG. In vivo NMR imaging evaluation of efficiency and toxicity of gene electrotransfer in rat muscle. *Gene Ther*. 2005;12(19):1434-43.
71. Okino M, Mohri H. Effects of a high-voltage electrical impulse and an anticancer drug on in vivo growing tumors. *Jpn J Cancer Res*. 1987;78(12):1319-21.
72. Heller R, Gilbert R, Jaroszeski MJ. Clinical applications of electrochemotherapy. *Adv Drug Deliv Rev*. 1999;35(1):119-29.
73. Collins JM, Despa F, Lee RC. Structural and functional recovery of electroporabilized skeletal muscle in-vivo after treatment with surfactant poloxamer 188. *Biochim Biophys Acta*. 2007;1768(5):1238-46.
74. Butts K, Sinclair J, Daniel BL, Wansapura J, Pauly JM. Temperature quantitation and mapping of frozen tissue. *J Magn Reson Imaging*. 2001;13(1):99-104.
75. Fleckenstein JL, Chason DP, Bonte FJ, et al. High-voltage electric injury: assessment of muscle viability with MR imaging and Tc-99m pyrophosphate scintigraphy. *Radiology*. 1995;195(1):205-10.
76. Lee RC, Despa F. Distinguishing electroporation from thermal injuries in electrical shock by MR imaging. *Conf Proc IEEE Eng Med Biol Soc*. 2005;6:6544-6.

77. Gissel H, Despa F, Collins J, et al. Magnetic resonance imaging of changes in muscle tissues after membrane trauma. *Ann N Y Acad Sci.* 2005;1066:272-85.
78. Haemmerich D, Staelin ST, Tsai JZ, Tungjitkusolmun S, Mahvi DM, Webster JG. In vivo electrical conductivity of hepatic tumours. *Physiol Meas.* 2003;24(2):251-60.
79. Schmidt HC, Tsay DG, Higgins CB. Pulmonary edema: an MR study of permeability and hydrostatic types in animals. *Radiology.* 1986;158(2):297-302.
80. Gwan K, Edzes HT. Water in brain edema. Observations by the pulsed nuclear magnetic resonance technique. *Arch Neurol.* 1975;32(7):462-5.
81. Naruse S, Horikawa Y, Tanaka C, Hirakawa K, Nishikawa H, Yoshizaki K. Proton nuclear magnetic resonance studies on brain edema. *J Neurosurg.* 1982;56(6):747-52.
82. Herfkens RJ, Sievers R, Kaufman L, et al. Nuclear magnetic resonance imaging of the infarcted muscle: a rat model. *Radiology.* 1983;147(3):761-4.
83. Paturneau-Jouas M, Parzy E, Vidal G, et al. Electrotransfer at MR imaging: tool for optimization of gene transfer protocols--feasibility study in mice. *Radiology.* 2003;228(3):768-75.
84. Su MY, Samoszuk MK, Wang J, Nalcioglu O. Assessment of protamine-induced thrombosis of tumor vessels for cancer therapy using dynamic contrast-enhanced MRI. *NMR Biomed.* 2002;15(2):106-13.
85. Viglianti BL, Lora-Michiels M, Poulson JM, et al. Dynamic Contrast-enhanced Magnetic Resonance Imaging as a Predictor of Clinical Outcome in Canine Spontaneous Soft Tissue Sarcomas Treated with Thermoradiotherapy. *Clin Cancer Res.* 2009.
86. Lee EW, Loh CT, Kee ST. Imaging guided percutaneous irreversible electroporation: ultrasound and immunohistological correlation. *Technol Cancer Res Treat.* 2007;6(4):287-94.
87. Ahmed M, Goldberg SN. Thermal ablation therapy for hepatocellular carcinoma. *J Vasc Interv Radiol.* 2002;13(9 Pt 2):S231-44.
88. Parkin DM, Bray F, Ferlay J, Pisani P. Estimating the world cancer burden: Globocan 2000. *Int J Cancer.* 2001;94(2):153-6.
89. Guo Y, Zhang Y, Klein R, et al. Irreversible electroporation therapy in the liver: longitudinal efficacy studies in a rat model of hepatocellular carcinoma. *Cancer Res.* 2010;70(4):1555-63.

90. Lee EW, Wong D, Tafti BA, et al. Irreversible electroporation in eradication of rabbit VX2 liver tumor. *J Vasc Interv Radiol*. 2012;23(6):833-40.
91. Sugiura N, Takara K, Ohto M, Okuda K, Hirooka N. Percutaneous intratumoral injection of ethanol under ultrasound imaging for treatment of small hepatocellular carcinoma. *Acta Hepatol Jpn*. 1983;24(920):1.
92. Deng J, Virmani S, Yang GY, et al. Intraprocedural diffusion-weighted PROPELLER MRI to guide percutaneous biopsy needle placement within rabbit VX2 liver tumors. *J Magn Reson Imaging*. 2009;30(2):366-73.
93. Brandt KR, Charboneau JW, Stephens DH, Welch TJ, Goellner JR. CT- and US-guided biopsy of the pancreas. *Radiology*. 1993;187(1):99-104.
94. Gilbert JC, Onik GM, Hoddick WK, Rubinsky B. Real time ultrasonic monitoring of hepatic cryosurgery. *Cryobiology*. 1985;22(4):319-30.
95. Nour SG, Goldberg SN, Wacker FK, et al. MR monitoring of NaCl-enhanced radiofrequency ablations: observations on low- and high-field-strength MR images with pathologic correlation. *Radiology*. 2010;254(2):449-59.
96. Holbrook AB, Santos JM, Kaye E, Rieke V, Pauly KB. Real-time MR thermometry for monitoring HIFU ablations of the liver. *Magn Reson Med*. 2010;63(2):365-73.
97. Mikami S, Tateishi R, Akahane M, et al. Computed Tomography Follow-up for the Detection of Hepatocellular Carcinoma Recurrence after Initial Radiofrequency Ablation: A Single-center Experience. *J Vasc Interv Radiol*. 2012;23(10):1269-75.
98. Krause BJ, Herrmann K, Wieder H, zum Buschenfelde CM. 18F-FDG PET and 18F-FDG PET/CT for assessing response to therapy in esophageal cancer. *J Nucl Med*. 2009;50 Suppl 1:89S-96S.
99. Okuma T, Matsuoka T, Okamura T, et al. 18F-FDG small-animal PET for monitoring the therapeutic effect of CT-guided radiofrequency ablation on implanted VX2 lung tumors in rabbits. *J Nucl Med*. 2006;47(8):1351-8.
100. Lee EW, Chen C, Prieto VE, Dry SM, Loh CT, Kee ST. Advanced hepatic ablation technique for creating complete cell death: irreversible electroporation. *Radiology*. 2010;255(2):426-33.
101. Thomson KR, Cheung W, Ellis SJ, et al. Investigation of the safety of irreversible electroporation in humans. *J Vasc Interv Radiol*. 2011;22(5):611-21.
102. Ellis TL, Garcia PA, Rossmeisl JH, Jr., Henao-Guerrero N, Robertson J, Davalos RV. Nonthermal irreversible electroporation for intracranial surgical applications. Laboratory investigation. *J Neurosurg*. 2011;114(3):681-8.

103. Guo Y, Zhang Y, Nijm GM, et al. Irreversible electroporation in the liver: contrast-enhanced inversion-recovery MR imaging approaches to differentiate reversibly electroporated penumbra from irreversibly electroporated ablation zones. *Radiology*. 2011;258(2):461-8.
104. Zhang Y, Guo Y, Ragin AB, et al. MR imaging to assess immediate response to irreversible electroporation for targeted ablation of liver tissues: preclinical feasibility studies in a rodent model. *Radiology*. 2010;256(2):424-32.
105. Appelbaum L, Ben-David E, Sosna J, Nissenbaum Y, Goldberg SN. US findings after irreversible electroporation ablation: radiologic-pathologic correlation. *Radiology*. 2012;262(1):117-25.
106. Ahmed M, Brace CL, Lee FT, Jr., Goldberg SN. Principles of and advances in percutaneous ablation. *Radiology*. 2011;258(2):351-69.
107. McGahan JP, Browning PD, Brock JM, Tesluk H. Hepatic ablation using radiofrequency electrocautery. *Invest Radiol*. 1990;25(3):267-70.
108. Onik GM, Cohen JK, Reyes GD, Rubinsky B, Chang Z, Baust J. Transrectal ultrasound-guided percutaneous radical cryosurgical ablation of the prostate. *Cancer*. 1993;72(4):1291-9.
109. Roth Y, Tichler T, Kostenich G, et al. High-b-value diffusion-weighted MR imaging for pretreatment prediction and early monitoring of tumor response to therapy in mice. *Radiology*. 2004;232(3):685-92.
110. Schraml C, Schwenzer NF, Clasen S, et al. Navigator respiratory-triggered diffusion-weighted imaging in the follow-up after hepatic radiofrequency ablation-initial results. *J Magn Reson Imaging*. 2009;29(6):1308-16.
111. Thompson SM, Callstrom MR, Knudsen B, et al. Development and preliminary testing of a translational model of hepatocellular carcinoma for MR imaging and interventional oncologic investigations. *J Vasc Interv Radiol*. 2012;23(3):385-95.
112. Moseley ME, Cohen Y, Mintorovitch J, et al. Early detection of regional cerebral ischemia in cats: comparison of diffusion- and T2-weighted MRI and spectroscopy. *Magn Reson Med*. 1990;14(2):330-46.
113. MacFall JR, Maki JH, Johnson GA, Hedlund LW, Cofer GP. Pre- and postmortem diffusion coefficients in rat neural and muscle tissues. *Magn Reson Med*. 1991;20(1):89-99.
114. Farrar CT, Kamoun WS, Ley CD, et al. Sensitivity of MRI tumor biomarkers to VEGFR inhibitor therapy in an orthotopic mouse glioma model. *PLoS One*. 2011;6(3):e17228.

115. Jamin Y, Tucker ER, Poon E, et al. Evaluation of clinically translatable MR imaging biomarkers of therapeutic response in the TH-MYCN transgenic mouse model of neuroblastoma. *Radiology*. 2013;266(1):130-40.
116. Rhee TK, Larson AC, Prasad PV, et al. Feasibility of blood oxygenation level-dependent MR imaging to monitor hepatic transcatheter arterial embolization in rabbits. *J Vasc Interv Radiol*. 2005;16(11):1523-8.
117. Tofts PS, Kermode AG. Measurement of the blood-brain barrier permeability and leakage space using dynamic MR imaging. 1. Fundamental concepts. *Magn Reson Med*. 1991;17(2):357-67.
118. Koh DM, Collins DJ. Diffusion-weighted MRI in the body: applications and challenges in oncology. *AJR Am J Roentgenol*. 2007;188(6):1622-35.
119. O'Connor JP, Jackson A, Asselin MC, Buckley DL, Parker GJ, Jayson GC. Quantitative imaging biomarkers in the clinical development of targeted therapeutics: current and future perspectives. *Lancet Oncol*. 2008;9(8):766-76.
120. Morgan B, Thomas AL, Dreves J, et al. Dynamic contrast-enhanced magnetic resonance imaging as a biomarker for the pharmacological response of PTK787/ZK 222584, an inhibitor of the vascular endothelial growth factor receptor tyrosine kinases, in patients with advanced colorectal cancer and liver metastases: results from two phase I studies. *J Clin Oncol*. 2003;21(21):3955-64.
121. Ergun I, Keven K, Uruc I, et al. The safety of gadolinium in patients with stage 3 and 4 renal failure. *Nephrol Dial Transplant*. 2006;21(3):697-700.

VITA

NAME: Yue Zhang

EDUCATION: B.S., Applied Physics, Nanjing University of Aeronautics and Astronautics, Nanjing, Jiangsu, China, 2007

M.S., Bioengineering, University of Illinois at Chicago, Chicago, Illinois, 2010

TEACHING EXPERIENCE: Teaching assistant at Department of Bioengineering at University of Illinois at Chicago, August 2007 – May 2008

RESEARCH EXPERIENCE: Research assistant at Department of Radiology at Northwestern University, August 2008 - Present

HONORS: Chancellor's Supplemental Graduate Research Fellowship, University of Illinois at Chicago, 2010-2011.

PROFESSIONAL MEMBERSHIP: International Society of Magnetic Resonance in Medicine

PUBLICATIONS: Jin N, Deng J, Chadashvili T, **Zhang Y**, Guo Y, Zhang Z, Yang G, Omary RA, Larson AC. Carbogen Gas-Challenge BOLD MRI in a Diethylnitrosamine-Induced Rat Liver Fibrosis Model. Radiology. 2010 Jan; 254(1):129-37.

Guo Y, **Zhang Y**, Klein R, Nijm GM, Sahakian AV, Omary RA, Yang G, Larson AC. Liver-Directed Irreversible Electroporation Therapy: Longitudinal Efficacy Studies in a Rat Model of Hepatocellular Carcinoma. Cancer Res. 2010 Feb 15; 70(4):1555-63.

Zhang Y, Guo Y, Ragin A, Lewandowski R, Yang G, Nijm G, Sahakian A, Omary R, Larson A. MRI to Assess Immediate Response to Irreversible Electroporation for Targeted Ablation of Liver Tissues: Pre-Clinical Feasibility Studies in Rodent Model. Radiology. 2010 Aug; 256: 424-32.